



**NTNU – Trondheim**  
Norwegian University of  
Science and Technology

# Experimental and Numerical Study on Plated Structures Subjected to Blast Loading

Numerical Simulations and Experimental  
Validation

**Cecilie Baglo**  
**Therese Myrstad Dybvik**

Civil and Environmental Engineering

Submission date: June 2015

Supervisor: Tore Børvik, KT

Co-supervisor: Vegard Aune, KT

Norwegian University of Science and Technology  
Department of Structural Engineering









## MASTER THESIS 2015

SUBJECT AREA: Computational Mechanics	DATE: June 10 2015	NO. OF PAGES: 168 + 40
--	-----------------------	---------------------------

TITLE:  <b>Experimental and Numerical Study on Plated Structures Subjected to Blast Loading</b>  Eksperimentelt og numerisk studie av platekonstruksjoner utsatt for eksplosjonslast	
BY:  Cecilie Baglo  Therese Myrstad Dybvik	 

SUMMARY: The main objective of this thesis was to investigate the response of thin plates, made of Docol 600 DL steel and the aluminium alloy EN-AW-1050A-H14, subjected to blast loading. The intention was also to validate the use of the shock tube facility at SIMLab at NTNU, and to recreate the experiments by using non-linear FE numerical simulations.  The material parameters were obtained by performing tensile tests of the two materials. An accurate material description was obtained by applying an inverse modelling method. To verify the pressure distribution in the shock tube, blast experiments were conducted and the exact pressures applied to the plate were measured. The results displayed a uniform pressure distribution subjected to the plate. After calibrating the pressure, component experiments were used to determine the structural response of the steel and aluminium plates.  Different analytical techniques were used in order to predict the structural response of the plates. Due to a dynamic blast loading, idealizations and analytical solutions proved to be too inaccurate. Numerical non-linear finite element simulations had to be introduced in order to solve the plate problem.  The finite element program Abaqus CAE was used to provide a simple numerical model of the plates. The implemented blast loads were based on the Friedlander equation. Although several simplifications were made in the design of the plates, the numerical model provided efficient results with adequate accuracy. A parameter study was performed in order to investigate how different parameters in the numerical model influenced the response of the plate. The reflected peak pressure and the thickness of the plate proved to affect the structural response the most.
--

RESPONSIBLE TEACHER: Professor Tore Børvik SUPERVISORS: Professor Tore Børvik and PhDc Vegard Aune CARRIED OUT AT: Department of Structural Engineering, NTNU
---





## MASTEROPPGAVE 2015

FAGOMRÅDE: Beregningsmekanikk	DATO: 10. Juni.2015	ANTALL SIDER: 168 + 40
----------------------------------	------------------------	---------------------------

TITTEL:

### **Ekspérimentelt og numerisk studie av platekonstruksjoner utsatt for eksplosjonslast**

Experimental and Numerical Study on Plated Structures Subjected to Blast Loading

UTFØRT AV:

Cecilie Baglo

Therese Myrstad Dybvik



SAMMENDRAG:

Hovedmålet med denne masteroppgaven var å undersøke responsen av tynne plater, laget av Docol 600 DL stål og aluminiumlegeringen EN-AW-1050A-H14, utsatt for eksplosjonslast. Hensikten var å validere bruken av den nye shock tuben ved SIMLab ved NTNU. I tillegg ble forsøkene gjenskapt ved bruk av ikke-lineære numeriske analyser.

Materialparameterne ble utarbeidet ved å utføre strekktester av de to materialene. En nøyaktig beskrivelse av materialene ble oppnådd ved å anvende en invers modelleringsmetode. For å verifisere trykkfordelingen i shock tuben, ble det utført eksperimenter hvor det eksakte trykket på platen ble målt. Resultatet viste en uniform trykkfordeling på platen. Etter å ha utført kalibrering av trykket, ble eksperimenter i shock tuben på stål- og aluminiumsplatene utført. Responsen av platene ble deretter undersøkt.

Det ble brukt flere analytiske metoder for å regne ut responsen av platene. Grunnet en dynamisk trykklast, ble disse metodene for upresise. For å løse plateproblemet måtte numeriske ikke-lineære element analyser bli tatt i bruk.

Elementprogrammet Abaqus CAE ble anvendt for å fremstille en enkel numerisk modell av platene. Den implementerte trykklasten ble basert på en tilpassing av Friedlanderligningen. Selv om flere antagelser og forenklinger ble innført under modelleringen av platen, ga den numeriske modellen effektive og tilfredsstillende resultater. For å undersøke hvordan de ulike parameterne påvirket responsen, ble flere parameterstudier utført. Det reflekterte topptrykket og tykkelsen på platen hadde størst effekt på responsen.

FAGLÆRER: Professor Tore Børvik

VEILEDERE: Professor Tore Børvik og PhDc Vegard Aune

UTFØRT VED: Institutt for Konstruksjonsteknikk, NTNU



## **MASTER'S THESIS 2015**

for

*Cecilie Baglo and Therese M. Dybvik*

### **Experimental and numerical study on plated structures subjected to blast loading**

#### **1. INTRODUCTION**

Protection of engineering structures against blast loading has received a lot of attention in recent years. Such structures are often made of steel or aluminium plates. Steel is often preferred due to its combination of high strength, high ductility and good formability, resulting in an effective load carrying capability at a relatively low price compared to many other materials. During the last decades aluminium alloys have become increasingly more attractive for structural applications, particularly due to its relatively high strength to weight ratio. Since thin plates are frequently being used in engineering structures, it has become necessary to predict the structural response of such components exposed to blast loading. Computational methods are now available to predict both the loading and structural response in these extreme loading situations, and experimental validation of such methods is necessary in the development of safe and cost-effective protective structures. In this study blast experiments will be performed, and the data will be used for validation and verification of some frequently used computational methods involving blast loading.

#### **2. OBJECTIVES**

The main objective of the research project is to determine how thin steel and aluminium plates behave under blast loading, and to validate to which extent this can be predicted using computational tools.

#### **3. A SHORT DESCRIPTION OF THE RESEARCH PROJECT**

The main topics in the research project will be as follows;

1. A comprehensive literature review should be conducted to understand the blast load phenomenon, blast load design, shock tube facilities, constitutive and failure modeling of metallic materials exposed to extreme loadings, and explicit finite element methods.
2. Tension specimens are extracted from the two materials (Docol 600DL steel and 1050A-H14 aluminium alloy) and tested in uniaxial tension using DIC to obtain the mechanical properties of the materials.
3. Proper constitutive relations and failure criteria are chosen and calibrated based on the material tests.
4. The SIMLab Shock Tube Facility will be used to expose the plates to blast loading, as an alternative to explosive detonations. The shock tube experiments will be used to investigate typical dynamic responses and failure modes of plated structures exposed to blast loading.
5. Digital Image Correlation (DIC) will be used to measure the 3D transverse displacement fields of the plates in the shock tube experiments.
6. Non-linear FE numerical simulations of the shock tube experiments will be performed, and the numerical results shall be compared and discussed based on the experimental findings.

*Supervisors:* Tore Børvik (NTNU) and Vegard Aune (NTNU)

The thesis must be written according to current requirements and submitted to the Department of Structural Engineering, NTNU, no later than June 10<sup>th</sup>, 2015.

NTNU, January 14<sup>th</sup>, 2015

Tore Børvik  
Professor



## **Abstract**

The main objective of this thesis was to investigate the response of thin plates, made of Docol 600 DL steel and the aluminium alloy EN-AW-1050A-H14, subjected to blast loading. The intention was also to validate the use of the shock tube facility at SIM-Lab at NTNU, and to recreate the experiments by using non-linear finite element (FE) numerical simulations.

The material parameters were obtained by performing tensile tests of the two materials. An accurate material description was obtained by applying an inverse modelling method. To verify the pressure distribution in the shock tube, blast experiments were conducted and the exact pressures applied to the plate were measured. The results displayed a uniform pressure distribution subjected to the plate. After calibrating the pressure, component experiments were used to determine the structural response of the steel and aluminium plates.

Different analytical techniques were used in order to predict the structural response of the plates. Due to a dynamic blast loading, idealizations and analytical solutions proved to be too inaccurate. Numerical non-linear finite element simulations had to be introduced in order to solve the plate problem.

The finite element program Abaqus CAE was used to provide a simple numerical model of the plates. The implemented blast loads were based on the Friedlander equation. Although several simplifications were made in the design of the plates, the numerical model provided efficient results with adequate accuracy. A parameter study was performed in order to investigate how different parameters in the numerical model influenced the response of the plate. The reflected peak pressure and the thickness of the plate proved to affect the structural response the most.





## Acknowledgements

This thesis is written for the Structural Impact Laboratory (SIMLab) at the Norwegian University of Science and Technology (NTNU). Working on this thesis has been highly educational and has offered us an opportunity to apply the knowledge we have acquired during our five years at NTNU. It has been a great and challenging experience.

We would like to thank our supervisor Professor Tore Børvik and co-supervisor PhD-candidate Vegard Aune at SIMLab for weekly guidance during this period. They have provided us with the necessary theoretical background, in addition to advice and critique. Their help has been greatly appreciated.

We would also like to thank Mr. Trond Auestad for assistance during the shock tube experiments and Professor Odd Hopperstad for helping us with the forming limit diagram (FLD).

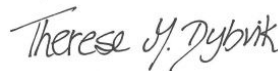
Special thanks are given to Dr. David Morin who has helped us characterizing the material behavior and constructed the material card applied in the numerical simulations. Morin has really been a great asset for us during these twenty weeks and he has deserved the title Super-David for always being available when advice has been needed.

In addition, gratitude is given to fellow M.S. candidates Karoline Osnes and Sondre Haug for helpful discussions and cooperation during the calibration experiments.

Trondheim, June 10 2015



*Cecilie Baglo*



*Therese Myrstad Dybvik*

# Contents

Abstract . . . . .	ii
Acknowledgements . . . . .	iv
Nomenclature . . . . .	ix
<b>1 Introduction</b>	<b>1</b>
<b>2 State of the Art</b>	<b>5</b>
2.1 Previous observations . . . . .	6
2.2 Shock Tube History . . . . .	9
<b>3 Theory</b>	<b>11</b>
3.1 Explosions . . . . .	11
3.1.1 Classification . . . . .	12
3.1.2 Explosion Processes . . . . .	13
3.1.3 Blast wave . . . . .	14
3.1.4 Above Ground Explosions - Reflection Process . . . . .	16
3.1.5 External Blast Loading . . . . .	17
3.1.6 Internal Blast Loading . . . . .	18
3.1.7 Ideal Blast Wave . . . . .	19
3.1.8 Blast Wavefront Parameters . . . . .	20
3.2 Shock Tube Theory . . . . .	22
3.2.1 The Ideal Gas Theory . . . . .	24
3.3 Failure Modes . . . . .	26
3.4 Forming Limits . . . . .	27

3.4.1	Forming Limit Diagrams (FLD) . . . . .	31
3.5	Material Characterization . . . . .	32
3.5.1	Strains and Stresses . . . . .	32
3.5.2	Necking . . . . .	33
3.6	Constitutive Equations . . . . .	35
3.6.1	The Johnson-Cook Material Model . . . . .	35
3.7	Digital Image Correlation . . . . .	38
<b>4</b>	<b>Materials</b>	<b>41</b>
4.1	Docol 600 DL Steel . . . . .	42
4.2	Aluminium alloy EN AW-1050A-H14 . . . . .	43
4.3	Experiments . . . . .	47
4.4	Material Identification . . . . .	49
4.4.1	Post Processing and Calibration . . . . .	49
4.4.2	Modelling of the Tensile Test using Abaqus CAE . . . . .	58
<b>5</b>	<b>Experimental Work</b>	<b>65</b>
5.1	The Shock Tube Facility at SIMLab . . . . .	65
5.2	Verification of the Pressure . . . . .	69
5.2.1	Ideal Gas Theory . . . . .	73
5.3	Component Test . . . . .	75
5.3.1	Experimental setup . . . . .	76
5.3.2	Calibration of the pressure . . . . .	78
5.3.3	Experimental Results . . . . .	81
5.4	Metallurgic Study of the Blast Subjected Plates . . . . .	93
<b>6</b>	<b>Analytical Calculations</b>	<b>97</b>
6.1	Empirical Model by Nurick and Martin . . . . .	97
6.2	Empirical Model for the Shock Tube Experiments . . . . .	101
6.3	Yield Line Theory . . . . .	104
6.4	Pressure-Impulse Diagrams . . . . .	110
6.5	Discussion of the Plate Problem . . . . .	113
<b>7</b>	<b>Numerical Study</b>	<b>115</b>

7.1	Abaqus/Explicit . . . . .	115
7.1.1	Numerical Model . . . . .	116
7.1.2	Sensitivity study . . . . .	118
7.1.3	Numerical Results . . . . .	123
<b>8</b>	<b>Parameter Studies</b>	<b>127</b>
8.1	Plate Thickness . . . . .	128
8.2	Steel vs. Aluminium Plates . . . . .	130
8.3	Strain rate sensitivity . . . . .	132
8.4	Pressure Distribution . . . . .	134
8.5	Material Parameters . . . . .	138
8.6	Temperature . . . . .	141
8.7	Capacity of the Steel Plates . . . . .	143
8.8	Forming Limits . . . . .	145
<b>9</b>	<b>Discussion</b>	<b>151</b>
<b>10</b>	<b>Conclusion</b>	<b>157</b>
<b>11</b>	<b>Further Work</b>	<b>159</b>
	<b>References</b>	<b>160</b>
<b>A</b>	<b>Theory (Ch. 3)</b>	<b>A1</b>
A.1	Numerical Integration . . . . .	A1
A.1.1	Explicit Direct Integration . . . . .	A1
A.1.2	Classical Central Difference . . . . .	A2
A.1.3	Half-Step Central Difference . . . . .	A3
A.1.4	Stability of Explicit Direct Integration . . . . .	A4
A.2	Finite Element Formulations . . . . .	A6
A.2.1	Preliminary Kinematics . . . . .	A6
A.2.2	Lagrangian Formulation . . . . .	A9
<b>B</b>	<b>Material Information (Ch. 4)</b>	<b>B1</b>
B.1	Material cards from the supplier . . . . .	B1

B.2	Data from the Tension Test . . . . .	B6
B.2.1	Initial Measurements of the Dog-Bone Specimen . . . . .	B6
B.2.2	Verification of 2D-DIC . . . . .	B7
B.2.3	Calibration of the Tension Test . . . . .	B8
B.2.4	Parameters for the isotropic hardening models . . . . .	B9
<b>C</b>	<b>Experimental Data (Ch.5)</b>	<b>C1</b>
C.1	Membrane Capacity . . . . .	C1
C.2	Calibration of the pressure in the Shock Tube . . . . .	C2
C.2.1	Pressure Distribution on the Rigid Plate . . . . .	C3
C.3	Component Experiments . . . . .	C5
C.3.1	Pressure distribution on the plates . . . . .	C6
C.3.2	Deformed plates . . . . .	C8
C.3.3	Matlab script . . . . .	C11
<b>D</b>	<b>Numerical Simulation (Ch. 7)</b>	<b>D1</b>
D.1	Material cards implemented in ABAQUS/Explicit . . . . .	D1
D.1.1	Direct modeling . . . . .	D1
D.1.2	Inverse modeling . . . . .	D4

# Nomenclature

## Acronyms

ALE	Arbitrary Lagrangian-Eulerian
CPU	Central Processing Unit
DIC	Digital Image Correlation
FE	Finite Element
FEA	Finite Element Analysis
FLC	Forming Limit Curve
FLD	Forming Limit Diagram
HE	High Explosives
LE	Low Explosives
NTNU	Norwegian University of Science and Technology
SIMLab	Structural Impact Laboratory

## Greek Letters

$I$	The 2 <sup>nd</sup> order unit tensor $\sigma$
$\sigma'$	Deviatoric stress tensor
$\alpha$	The linear thermal expansion coefficient
$\alpha$	Stress ratio
$\alpha$	Dimensionless damage number
$\alpha_I$	The angle of incidence
$\beta$	Strain ratio
$\beta$	Geometry number
$\gamma_1$	The ratio of the specific heat at constant pressure to that at constant volume for the driven gas
$\gamma_4$	The ratio of specific heats for the driver gas
$\Delta\varepsilon_e$	Strain deviation
$d\varepsilon'_2$	Strain increment parallel to neck
$\varepsilon$	Strain
$\varepsilon_1, \varepsilon_2$	Major and minor principal strains in the plane of the sheet

$\varepsilon_1^*$	Critical strain at instability
$\varepsilon_{ce}$	Corrected engineering strain
$\varepsilon_e$	Engineering strain
$\varepsilon_l$	Logarithmic strain (true strain)
$\varepsilon_{me}$	Measured engineering strain
$\theta$	Rotation of the region about its axis of rotation
$\theta$	Angle between the loading axis
$\lambda$	Aspect ratio
$\nu$	Poisson's ratio
$\rho$	Density
$\rho_0$	The density of air at ambient pressure ahead of the blast wave
$\rho_s$	Air density behind the wavefront
$\sigma$	Stress
$\sigma_0$	Yield stress
$\sigma_{ce}$	Measured stress
$\sigma_d$	Damage stress
$\sigma_{dy}$	Dynamic yield stress
$\sigma_e$	Engineering stress
$\sigma_{eq}$	Equivalent stress
$\sigma_t$	Cauchy stress (true stress)
$\sigma^{\nabla J}$	The Jaumann rate of the Cauchy stress tensor $\sigma$
$\phi$	Modified damage number
$\chi$	The Taylor-Quinney coefficient
$\Psi$	Geometrical damage number
$\omega$	Frequency
$\Omega$	is the set of pixels within the subset at the reference configuration

## Latin Letters

$\mathbf{d}$	The rate-of-deformation tensor
$\mathbf{d}^e, \mathbf{d}^p, \mathbf{d}^t$	Elastic, thermal and plastic part of the rate-of-deformation tensor
$\mathbf{x}$	refers to the image coordinates in the current configuration
$\mathbf{X}$	refers to the image coordinates in the reference configuration
$\dot{D}$	The rate of deformation
$\dot{p}$	The equivalent plastic strain rate
$\dot{p}_0$	Reference strain rate
$\dot{p}^*$	Normalized plastic strain rate
$\dot{T}$	The rate of temperature increase
$a_0$	The speed of sound at the ambient pressure
$a_1$	The speed of sound
$a_4$	The speed of sound in the undisturbed driver gas
$b$	Width of the neck
$b$	The decay of the pressure-time curve
$B$	Width of the plate
$A$	Cross section area
$A_0$	Area of the plate exposed to the impulse
$A_0$	Initial cross section area
$A, B, n, m$	Material parameters in the von Mises yield function
$C$	Material constant governing strain-rate sensitivity
$C_p$	The specific heat capacity
$D_c$	Critical damage
$E$	Young's modulus
$E$	Activation energy
$E_{corr}$	Correct elastic modulus
$E_{meas}$	Measured elastic modulus
$f$	Yield function
$F_L$	The force from the tension test
$F_{max}$	Maximum force
$G$	Shear modulus



i	represents a specific pixel
I	Total impulse
$I_0$	Impulse per area
$I^+, I^-$	Positive and negative impulse
$I_c$	is the current image
$I_r$	is the reference image
k	Spring constant
$K_L, K_M, K_{LM}$	The load-, mass- and load-mass factor
K,n	Hardening parameters in power law
l	Length of the yield line
L	Length of the plate
$L_0$	Initial gauge length
$m_1$	Molecular weight
$m_p$	Plastic moment capacity of the yield line
$M_s$	Mach number
$M_t$	Mass of the plate
p	Accumulated plastic strain
P	Pressure
$P_0$	The ambient pressure
$P_{dynamic}$	Dynamic pressure
$P_r$	Reflected pressure
$P_s$	Side-on (incident) pressure
$P_s^+, P_s^-$	Positive and negative peak side-on pressure
$P_{stagnation}$	Stagnation pressure
$P_{static}$	Static pressure
q	Load acting within a particular region of the plate
$q_d$	Dynamic collapse load
$q_s$	The maximum dynamic pressure
$q_s$	Static collapse load
Q	Heat flux
$Q_R, C_R$	Hardening parameters in Voce rule
R	Distance from the center of a source of explosion

---

R	The universal gas constant
R	Hardening variable for power law and voce rule
$R_{m,max}$	Maximum tensile strength
$R_{m,min}$	Minimum tensile strength
$R_{p,02,max}$	Maximum yield strength (0.2 offset)
$R_{p,02,min}$	Minimum yield strength (0.2 offset)
t	Time
t	Plate thickness
$t_A$	Time after an explosion
T	The absolute temperature
$T_0$	The room temperature of the material
$T_1$	The inital measured temperature
$T_m$	The melting temperature of the material
$T_n$	Natural period
$T^+, T^-$	Duration of positive and negative phase for a blast wave
$T^*$	The homologous temperature
u	Velocity
$U_s$	The blast wavefront velocity
v	The impact velocity
V	Volume
$W_c$	Failure parameter
$W_e$	External work
$W_i$	Internal work

# Chapter 1

## Introduction

Explosions can be caused by various reasons. It may be a consequence of military operations or terrorist attacks. Accidental explosions may also arise due to incidents at e.g. nuclear industries. Explosions can be extremely powerful and it can result in severe structural damage. By understanding the nature behind blast loading, the design of buildings can be accommodated to withstand shock waves and thereby reduce the loss of human lives.

Traditionally, concrete has been employed when protecting structures against explosions. A main drawback of this material is the massive weight and its inflexibility, leading to a more or less stationary structure. Due to these unfavourable features, the interest of steel and aluminium plates has increased.

There has been an abundance of work performed on the field of blast loading. Previous work includes full-scale testing with real explosions. Such research is both expensive, difficult and time consuming. By introducing the shock tube as a testing facility, experiments can be performed in a controlled environment.

In this thesis, shock tube experiments will be performed on steel and aluminium plates. Validation of the pressure distribution will be conducted. In addition, investigation of the pressure-time history is performed in order to see if the shock tube is able to represent real explosion behaviour. Subsequently, different analytical approaches will be

used to examine the response of the plate. The experiments will also be recreated using the FE program Abaqus CAE. The structural responses will be simulated using a Lagrangian formulation and a simplified blast load description based on the Friedlander equation. The numerical results will be compared with the experimental data. Finally, parameter studies will be conducted in order to investigate how different parameters influence the response of the plate.

A short overview of each chapter is given below:

### **Chapter 2** - State of the Art.

A review of previous experimental work within the field of blast loading is given. The chapter is limited to research of square, clamped metal plates. The aspects of the shock tube history is also presented.

### **Chapter 3** - Theory.

Blast related theory, material characterization and constitutive equations are presented. Shock tube theory, forming limits and digital image correlation are briefly described.

### **Chapter 4** - Materials.

In addition to general theory about Docol 600 DL steel and the aluminium alloy EN AW-1050-H14, calibration of the materials is presented.

### **Chapter 5** - Experimental Work.

An introduction of the shock tube used in the experiments is given. The experimental setup and the calibration of the pressure are explained. The results are displayed in the final section.

### **Chapter 6** - Analytical Calculations.

By use of theoretical approaches such as empirical modelling and analytical models, the plate problem is investigated.

### **Chapter 7** - Numerical Study.

The experiments are recreated using the finite element program Abaqus CAE. A sensitivity study is performed to find the suitable element size and to see if shell elements

give satisfying results. Further the experimental results are compared with the corresponding numerical simulations.

**Chapter 8** - Parameter Study.

Different parameters are studied numerically to see how they influence the response of the plate. Examples of parameters that are tested are the strain rate sensitivity, the pressure distribution and the thickness of the plate.



## Chapter 2

# State of the Art

When performing scientific research it is important to get an overview over previous observations of similar studies. Since the field of blast loaded plates is wide, it is necessary to narrow down the scope of interest. The laboratory research in this thesis involves square, clamped metal plates, hence this will also be the main focus when presenting former studies. However, other observations are introduced if necessary.

### Preliminary discussion

The two main objectives when studying blast waves are:

- To describe the blast loading
- To describe the structural and material response

Full-scale tests are expensive and hard to validate since the test object and equipment may be destroyed. By introducing the shock tube as a testing facility, the blast experiments can easier be investigated. In order to replace real explosive testing with shock tube experiments, it is important to verify that the experiments performed in the shock tube corresponds to the pressure-time history of real explosions. However, it is ideal to use finite element analyses to predict the outcome of an explosion. This is a more

economic and time-saving solution. Experiments are necessary when validating the reliability and accuracy of the finite element results with experimentally obtained data [1].

When performing numerical simulations, there are several alternatives regarding finite element formulations. Both a Lagrangian and Eulerian finite element formulation may be used when simulating the structural response due to blast loads [2]. However, both of these methods have certain shortcomings. While the Lagrangian formulation is not able to follow large distortions of the computational domain, the Eulerian approach can handle these distortions but generally at the expense of precise interface definition and the resolution of flow details. Consequently, a fully-coupled Arbitrary Lagrangian-Eulerian (ALE) formulation has been developed to combine the best features of the two finite element formulations. By using the ALE description, greater distortions of the continuum can be handled while preserving the resolution of material interfaces.

During blast loading, interaction between the deformation of the structure and the motion of the fluid occurs [3]. Fluid-structure interaction (FSI) must therefore be taken into account when simulation blast scenarios. In order to solve a FSI problem efficiently, the ALE approach may be applied. Ideally, all blast simulations should be carried out using a coupled formulation. However, both the accuracy and the computational cost must be considered when choosing a suitable numerical approach.

## 2.1 Previous observations

In 1973 Menkes and Opat conducted a series of experiments utilizing sheet explosive applied to clamped aluminium beams. By exposing the beams to high-intensity short-duration transverse pressures, three damage modes were discovered. The failure modes were classified as [4]:

- Mode I: Large inelastic deformation
- Mode II: Tearing (tensile failure) in outer fibres, at or over the support
- Mode III: Transverse shear failure at the support

These failure modes were observed for circular plates by Teeling-Smith and Nurick [5]



and for square plates by Olson et al. [6] and Nurick and Shave [7]. When studying the response of the thin square plates, tearing was observed to start at the middle of the boundary and then evolve along the boundary towards the corners. As a consequence, Nurick and Shave found it necessary to make some additions to mode II by defining the following modes,

- Mode II\*: Tensile tearing at outer fibres over part of the support
- Mode IIa: Complete tearing of the sides and increasing mid-point deflection with increasing impulse
- Mode IIb: Complete tearing of the plate and decreasing mid-point deflection with increasing impulse

In 1988, Nurick and Martin [8] published an article containing a review of the dynamic response of thin plates subjected to impulse loading . Since it is not desirable to repeat the same information here, the review is from now on focus on experimental research conducted after this period.

Experimental results for stiffened plates have been reported by Schubak et al.[9] [10] and Scheleyer et al. [11]. Fully built in stiffened square plates were researched by Nurick et al.[12]. The plates exhibited mainly mode I and only a few examples of mode II failure as the load intensity increased . The same results were obtained when built in mild steel quadrangular plates with different stiffener configurations were examined. The findings of Yuen and Nurick [13] suggested that the stiffeners did not reduce the tearing, but actually initiated it earlier.

In the experiments mentioned above, the plates were exposed to a uniform loading. When Wierzbicki and Nurick [14] investigated the effect of a localized impulsive loading, they discovered two distinct failure modes of the plates. While the first mode was a formation of a disc with a diameter slightly larger than the diameter of the centrally placed sheet explosive, the second mode was a tensile tearing fracture at the clamped edge .

Rakvåg et al. [15] performed experiments on clamped steel plates with pre-formed holes. The pre-formed holes were an idealization of a fragment loading, representing the fragments perforating the plates. The results revealed that for low impulses, the

holes did not degrade the structural resistance of the plates. It was found that the decrease in stiffness caused by the pre-formed holes, was compensated by a reduced load area. Rakvåg et al. also discovered that both the size and shape of the holes influenced the magnitude of the midpoint deflection.

Using finite element software, connections between experiments and numerical simulations can be drawn. Jacinto et al. [16] researched metallic plates subjected to explosive loads. In order to obtain guidelines to a numerical model, the same plates were modelled in Abaqus. By comparing the results from the experiments with the simulations, the accuracy of a variety of calculation methods was found. Jacinto et al. [16] observed that selecting the appropriate number of vibration modes were crucial for the accuracy of the dynamic behaviour of the analyzed structure .

Alia and Souli [17] performed an air blast simulation using Eulerian multi-material formulations. To validate the approach, the numerical findings were compared with experimental results. They found the simulated pressure-time history and impulse to be in accordance with the experimental results. From this, they concluded that the Eulerian multi-material method was an accurate approach to simulate explosions.

Olovsson et al. [18] introduced the corpuscular approach, a new procedure to describe close-range blast loading. Experimental research and numerical simulations in the finite element program LS-DYNA were performed to study the differences between the Eulerian and corpuscular approaches. The research indicated that the corpuscular method could be a functional tool for simulating close-range blast loading on structures. However, some adjustments had to be made regarding the implementation in LS-DYNA before the method was ready for use. Olovsson et al. [18] found the discrete particle method to be numerically robust, relatively fast and easy to use.

Børvik et al. [19] simulated the structural response of a steel plate subjected to the combined effect of blast and sand impact loading from a buried charge. The discrete particle method was used to model the load due to the high explosive detonation products. Experiments with spherical 150g C-4 charges detonated at different stand-off distances were then conducted on the same plates to validate the discrete particle method. The results showed that the discrete particle based method gives a realistic prediction of

the sand ejecta speed and momentum. In addition, good quantitative agreement was found between the experimental data and numerical simulations [19].

Spranghers. et al [1] investigated the dynamic response of aluminium plates under free air explosions. Simulations using a finite element approach were conducted and the results were validated with experimental data obtained from 3D digital image correlation. The accuracy of the finite element results were examined by modifying certain parameters such as the element type, element size and integration method. Since transverse shear strains only occurred in a small, localized area, it was decided that use of thin shell elements were allowed when modelling the aluminium plate.

## 2.2 Shock Tube History

In 1860, Bernhard Riemann [20] investigated the basic principle of shock tubes. Approximately forty years later, in 1899, the first shock tube facility was built by Paul Vieille [21] with the intention to study the deflagration of explosive charges. It was the Austrian scientist, Kobe [21], that developed the theory of origination of a shock wave. To be able to study and visualize the invisible shock waves, Cranz and Schardin [21] developed an optical system to record fast processes.

Around the 1940s, scientists started to study the flow in shock tubes and the application of the shock tube was extended to pressure calibration and wave propagation. At the same time, the British scientists Payman and Shepherd [21] wanted to solve the problem of explosion danger in UK mines by utilizing the shock tube to investigate the detonation processes. The shock tube was also used to perform research of hypersonic gasdynamics.

Some years later, the shock tube was employed in the field of aerodynamics and shock tunnels were developed [22]. In the 1950s, the first applications of shock tubes deriving high temperature chemical kinetic information were registered. By increasing the temperature, it was possible to study a greater range of phenomena in industrial processes such as the aircraft industry [23]. About 20 years later, the shock tube along with laser sources started research on species detection. By discovering multi-species time-

histories, it was possible to provide a complete picture of fuel chemistry [24] [25].

Shock tubes have been developed in a wide range of sizes. Traditional shock tubes are made from metal tubing. This leads to a heavy and costly machine that is difficult to modify. By using plastic tubing instead of metal, Downes et al. [26] introduced a low cost shock tube. By replacing the metal with plastic, the weight of the shock tube was reduced and modifications of the tube were easier to achieve.

While conventional shock tubes are designed to test small objects, large blast wave simulators can accommodate heavy equipment such as trucks, tanks and helicopters. A few facilities exist in Europe, e.g in the United Kingdom, Germany and France [21].

Today, the shock tube is a versatile instrument used in several fields, e.g. to investigate blast load response [27], to develop renewable fuel sources [28] [29], to study nitrogen-containing fuels, to conduct medical research [30] and within the field of astrophysics [31].

# Chapter 3

## Theory

### 3.1 Explosions

In general, explosions are described as a rapid release of energy and volume change often followed by extreme destruction and heat [32]. The characteristics of the explosion strongly depend on localization and the substance it travels through. Different types of explosions are listed below,

- Mechanical explosions
- Chemical explosions
- Nuclear explosions

Mechanical explosions are caused by mechanical forces. E.g. a closed container with gas heated until rupture. On the contrary, chemical explosions occur when one or several substances have a chemically reaction and simultaneously produces a massive quantity of gas with high temperature. E.g. a rocket that is easily detonated with a flame. Nuclear explosions are caused by a fast nuclear reaction either by fusion or fission, releasing energy from highly-powered atomic bonds, or radiation on matter. A nuclear explosion is significantly more powerful than both mechanical and chemical explosions.

How the explosions are processed and analysed are related to several factors. Initially, it is dependent on the location of the explosion. Is the explosion over or under ground? The processing is also related to the propagation of the blast wave. Does the blast wave propagate in free space (external blast load) or in a limited space (internal blast wave)? The explosions also depend on the substance they are travelling through, e.g. air or water. To enhance the general understanding on how explosive loads propagate, relevant theory is presented in the next sections.

### 3.1.1 Classification

Explosions can be classified by their nature in which they detonate or deflagrate. High explosives (HE) detonate and produces a powerful blast wave driven by a chemical decay in high speed, while low explosives (LE) deflagrate. LE generate a subsonic explosion, while HE produce a supersonic explosion due to an explosive rate faster than the speed of sound. The sensitivity of initiation is also a way of categorizing explosives, where a primary explosive easier detonates compared with a secondary explosive. In the end of the nineteenth century one of the more known explosives TNT (Trinitrotoluene) was developed [33]. To easily compare different explosives, they can all be converted into TNT equivalents. This is done by multiplying the charge mass of the substance with a conversion factor based on the energy of both the TNT and the respective charge. Some examples of HE with their conversion factors are displayed in Table 3.1 [34].

**Table 3.1:** Conversion factors for explosives [34].

Explosive	TNT equivalent
TNT	1.000
C4	1.340
RDX (Ciklonit)	1.185
Nitroglycerin (liquid)	1.481

### 3.1.2 Explosion Processes

While the safety of an explosion depends on its thermal stability, the reliability is defined by the thermal instability. Figure 3.1 demonstrates the initiation of a reaction when the activation energy  $E$  is added. The substance decomposes to the yield of explosion until all the heat energy is released  $Q$ . For a primary explosive less activation energy  $E$  is required to reach ignition. A commonly method to initiate a secondary explosive is with use of another explosive material. This leads to the creation of a high intensity shock wave [35].

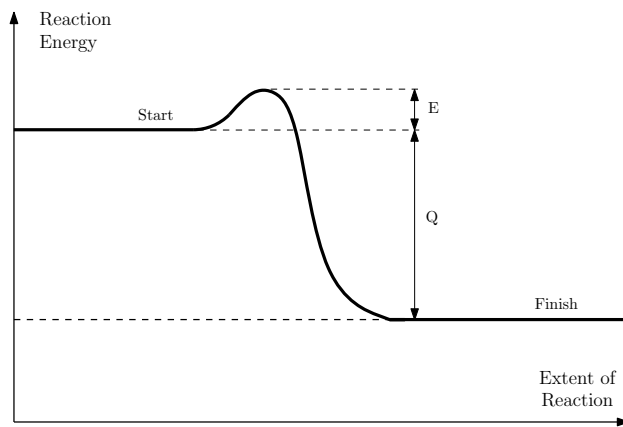


**Figure 3.1:** Energy changes in explosive reaction[35].

### 3.1.3 Blast wave

Blast waves are defined as the air wave set in motion by an explosion [36]. It includes shock waves, sonic compression waves and rarefaction waves. Blast waves are divided into categories depending on how and when the energy is released in the explosion, and the distance from the point of detonation. Figure 3.2 presents the pressure-time histories of three types of blast waves. The composition of the different blast waves are explained below,

- i. A shock wave followed by a rarefaction wave
- ii. A shock wave followed by a sonic compression wave and then a rarefaction wave
- iii. A sonic compression wave and a rarefaction wave

While category *i* is typical for strong explosions, category *iii* is characteristic for weaker explosions.

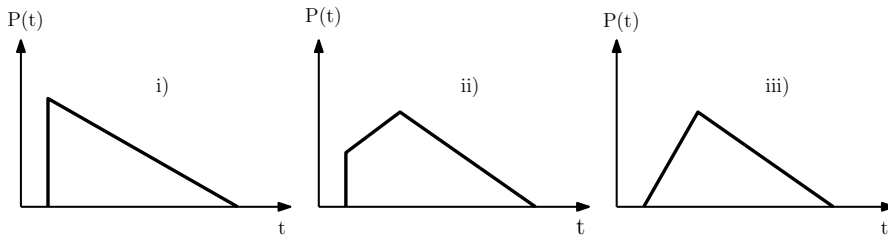


**Figure 3.2:** Different types of blast waves [36].

There are several types of pressures that form during an explosion. While the static pressure refers to the pressure level before the blast waves were formed, the dynamic pressure is related to the motion of the blast waves. The dynamic pressure can be expressed by using the flow velocity  $u$  and density  $\rho$ . The stagnation pressure is the pressure at a stagnation point, thus any point in a flow where the velocity is zero [37]. Mathematically it is the sum of the static- and dynamic pressure.

$$P_{\text{dynamic}} = \frac{1}{2} \rho u^2 \quad \text{and} \quad P_{\text{stagnation}} = P_{\text{static}} + P_{\text{dynamic}} \quad (3.1)$$



In addition to the static-, dynamic- and stagnation pressure, the terms side-on (incident) pressure  $P_s$  and reflected pressure  $P_r$  are important parameters. An illustration of the side-on pressure and the reflected pressure is given in Figure 3.3. The side-on pressure and the reflected pressure are measured perpendicular and parallel to the propagation direction of the wave, respectively.

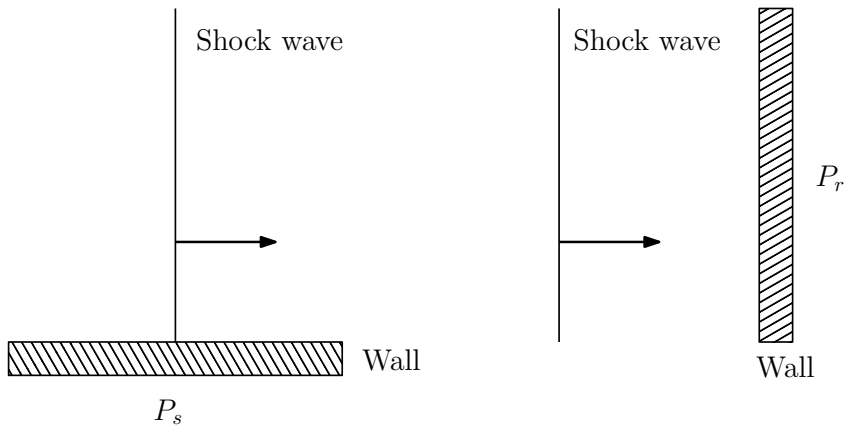


**Figure 3.3:** Side-on pressure and reflected pressure [36].

### 3.1.4 Above Ground Explosions - Reflection Process

The angle of incidence  $\alpha_I$  is an important parameter when discussing blast waves. If  $\alpha_I$  is  $90^\circ$ , there is no reflection and the surface is loaded by the side-on pressure. However if  $0 < \alpha_I < 90^\circ$ , there are two possibilities regarding reflection, i.e. regular or Mach reflection. Regular reflection occurs up to a limiting value of  $\alpha_I$  [35]. According to Bulson [33] this value is  $45^\circ$ , and when  $\alpha_I$  exceeds this threshold value, the Mach reflection takes place.

When the incident wave impacts the surface, a reflected shock wave is created. Since this wave travels with a velocity that is greater than the initial shock wave, the reflected shock wave overtakes the initial wave at what is known as the triple point. Here, a third wavefront, called the Mach stem, is formed. An illustration of this event is shown in Figure 3.4. Here, the Mach stem is given as a straight line. It is usually a fair assumption, even though it is not always the case.

As observed in Figure 3.4, the Mach front increases as the distance from the charge increases. If the triple point is established above the target, it can be assumed that the target is exposed to a uniform pressure distribution. If the triple point is located below the structure's height, the pressure distribution needs to be adjusted. However, it is important to know that assuming the target is only affected by the Mach front is a simplification. To establish the blast exactly, it is necessary to use advanced numerical simulations [38].

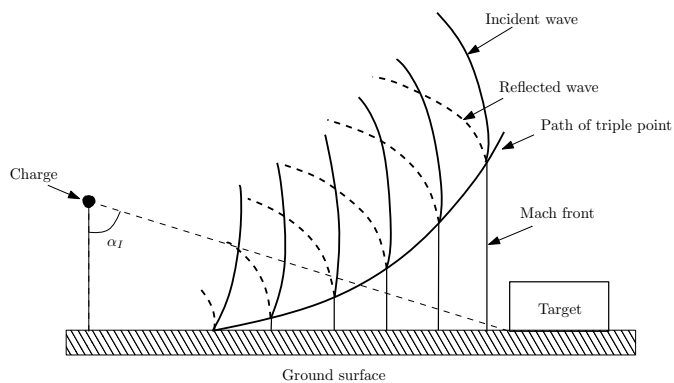
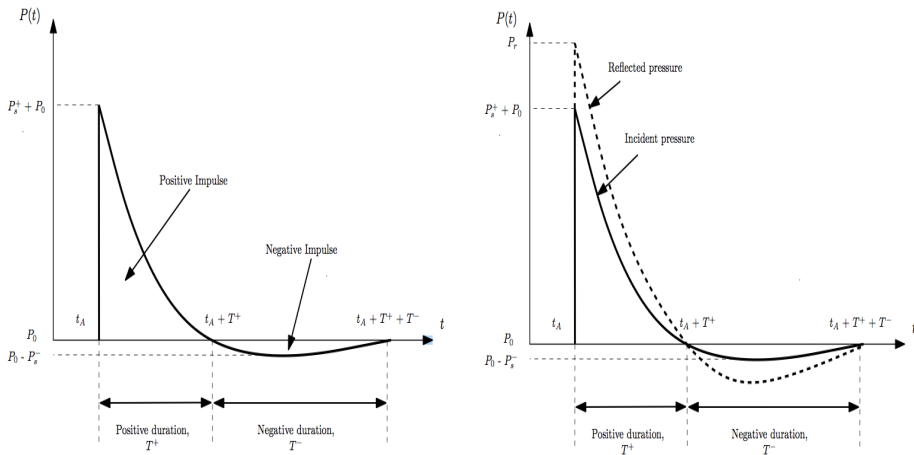


**Figure 3.4:** The reflection process of above ground explosions [38].

### 3.1.5 External Blast Loading

Figure 3.5a displays the blast wave pressure-time history for explosions in open air. An assumption of this description is that the wave propagates without encountering any obstacles.  $P_0$  is the ambient pressure, which is equivalent to the atmospheric pressure. At time  $t_A$  after the explosion, the pressure increases to a value  $P_s^+ + P_0$ . This peak value of overpressure is called the incident pressure. The pressure decreases to the ambient pressure during the time  $T^+$ . The time period between the peak value and the regained ambient pressure is referred to as the positive phase. This state is followed by a negative phase where the pressure decreases to its minimum point,  $P_0 - P_s^-$ , before increasing and returning to the ambient pressure at time  $t_A + T^+ + T^-$  [39].



(a) Blast wave pressure-time history when propagating in open air.

(b) Reflected blast wave pressure-time history when encountering obstacles.

Figure 3.5: Pressure-time histories of external blast loadings [39].

If the blast wave encounters any obstacles that are not parallel to the direction of propagation, a reflected pressure  $P_r$  is generated. Figure 3.5b displays the reflected pressure-time history. By observing the figure, it is evident that the reflected pressure is of the same shape as the incident pressure with an increase of the peak value. The form of the reflected pressure depends on two variables, the incident wave and the angle of the inclined surface. The duration however, depends on the size of the obstacle the wave encounters.

The mathematical description of the impulses due to the blast wave, are defined in Equations (3.2) and (3.3) [39].

$$I^+ = \int_{t_A}^{t_A+T^+} [P(t) - P_0] dt \quad (3.2)$$

$$I^- = \int_{t_A+T^+}^{t_A+T^++T^-} [P(t) - P_0] dt \quad (3.3)$$

### 3.1.6 Internal Blast Loading

Internal explosions occur inside a restrained area. The loading from such explosions can be divided into two phases:

- The shock pressure phase
- The gas pressure phase

The first phase is represented by Figure 3.6. It presents the reflected shock waves that appear due to the boundaries. The duration of this phase is short and depends on the shock front velocities and the distance between the charge and the surface.

In the gas pressure phase, the blast environment becomes troublesome to define. As reflected shock waves propagate, they are bound to collide with one or more of the surfaces that define the given area. For every interaction between a shock wave and a surface, a new reflected shock wave is developed. An increase in complexity also arises due to the clearing effect [40]. In a corner of a structure, the pressure and the impulse decrease to maintain continuity in the fluid domain. The gas pressure phase is also called the quasi-static phase due to its relatively long duration. This phase is terminated when the pressure decreases to the ambient level [38].

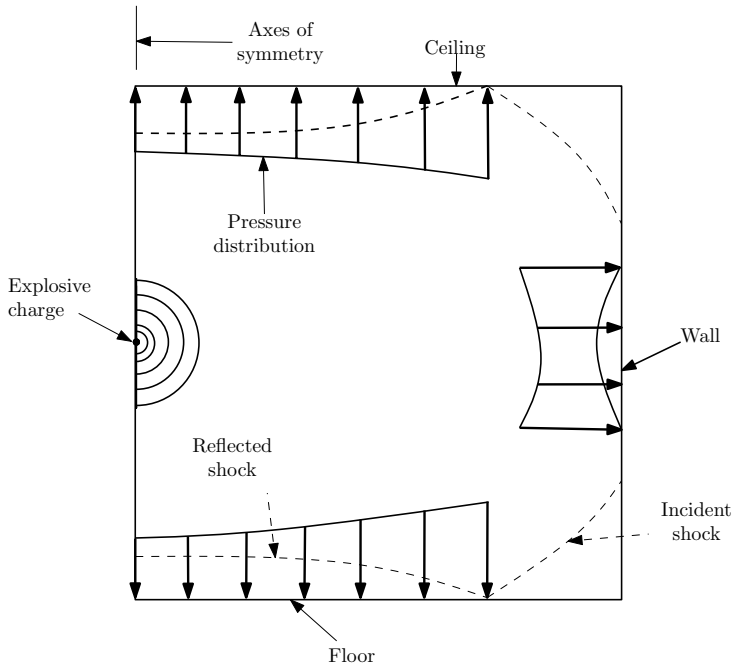


**Figure 3.6:** Shock reflections from walls during an internal explosion [38].

### 3.1.7 Ideal Blast Wave

The terms ideal or classical blast waves demand two requirements to be satisfied [39]. Primarily, the explosion must occur in a still, homogeneous atmosphere. In addition, the source needs to be spherically symmetric, meaning the blast wave only depends on two parameters, the distance from the center of the source  $R$  and the time  $t$ .

Numerous equations are given to describe the pressure-time history of the ideal blast wave. The functions vary in complexity and accuracy, but the main emphasis of most of the functions are fitting of the positive phase.

The simplest description of the blast wave assumes a linear decay of the pressure [39].

$$P(t) = P_0 + P_s^+ \left(1 - \frac{t}{T^+}\right) \quad (3.4)$$

Equation 3.4 applies when the time after arrival is between  $0 < t \leq T^+$ . To maintain a

true positive impulse  $I^+$  the positive phase duration  $T^+$  is adjusted. The true value for  $P_s^+$  is usually preserved when fitting this expression to data.

A more complex formulation of the blast wave is given by the modified Friedlander equation,

$$P(t) = P_0 + P_s^+ \left(1 - \frac{t}{T^+}\right) e^{-\frac{bt}{T^+}} \quad (3.5)$$

The difference from Equation (3.4) is the additional exponential term, where  $b$  represent the decay of the pressure-time curve. The combination of complexity and sufficient accuracy, makes the modified Friedlander equation preferable when describing the pressure-time history of the ideal blast wave.

### 3.1.8 Blast Wavefront Parameters

The equations for blast wavefront velocity  $U_s$ , air density behind the wavefront  $\rho_s$ , and the maximum dynamic pressure  $q_s$  are defined as [35],

$$U_s = \sqrt{\frac{6P_s + 7P_o}{7P_o}} a_o \quad (3.6)$$

$$\rho_s = \frac{6P_s + 7P_o}{P_s + 7P_o} \rho_o \quad (3.7)$$

$$q_s = \frac{5P_s^2}{2(P_s + 7P_o)} \quad (3.8)$$

where,

$P_s$  is the peak static overpressure or incident pressure

$P_0$  is the ambient pressure ahead of the blast wave

$\rho_0$  is the density of air at ambient pressure ahead of the blast wave

$a_0$  is the speed of sound at the ambient pressure

When the air behaves as an ideal gas, the reflected peak pressure mentioned in Section 3.1.5 can be expressed as,

$$P_r = 2P_s \left[ \frac{7P_0 + 4P_s}{7P_0 + P_s} \right] \quad (3.9)$$

When the incident pressure  $P_s$  is much smaller than the ambient pressure  $P_0$  ( $P_s \ll P_0$ ), Equation (3.9) is reduced to,

$$P_r = 2P_s \quad (3.10)$$

This is the lower acoustic limit of the reflected peak pressure and it is equivalent to a weak shock.

A strong shock is characterized by a incident pressure that is much larger than the ambient pressure ( $P_s \gg P_0$ ). Equation (3.9) will then be on the form,

$$P_r = 8P_s \quad (3.11)$$

### 3.2 Shock Tube Theory

The shock tube facility at SIMLab at NTNU is used when performing the experimental work in this thesis. It is therefore necessary to give a proper introduction of the fundamental theory behind this laboratory instrument.

The shock tube is used when generating shock waves under controlled conditions. The fundamental idea can be explained by considering the one dimensional shock tube depicted in Figure 3.7. The driver and driven sections are high and low pressure chambers, respectively. The two sections are separated by a diaphragm. The driven section is filled with pressurized air until the diaphragm ruptures. A series of compression waves are generated within the driver gas and these coalesce to form a shock wave that propagates into the driven gas [41]. When the diaphragm ruptures, pressure is released causing an expansion wave to propagate back into the driver section. Simultaneously, a contact surface between the driven and driver gases is formed. Since this contact surface has a lower velocity than the shock wave, it propagates along the tube behind the shock front.

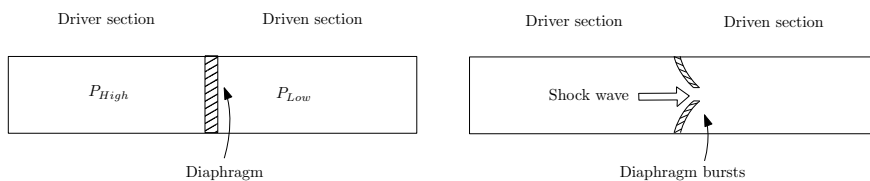


**Figure 3.7:** One dimensional shock tube.

The pressure propagation in a conventional shock tube, is illustrated in Figure 3.8. In the first figure, the driver and driven sections have uniform pressures  $P_4$  and  $P_1$ . This corresponds to a situation where the diaphragm bursts. After rupture, the shock tube condition changes as shown in (b). The shock front is now propagating into the driven gas with a constant pressure  $P_2$  behind the shock. The contact surface between the driver and driven gases propagates in the same direction as the shock front but at a lower speed. In the third figure, the rarefaction wave is reflected from the end of the driver section and the reflected wave is propagating towards the other end of the tube. The last figure shows how the shock wave is reflected from the end of the tube, where



the pressure has increased to  $P_5$ . The reflected shock wave propagates back into the part of the tube at pressure  $P_2$ . When the wave meets the contact surface, it is partially reflected and transmitted. It should be noted that Figure 3.8 applies for a low-pressure shock tube with uniform diameter. As seen, a constant cross-section implies an approximate linear and constant wave propagation. Since the area of the shock tube does not change, it is not possible for the shock wave to expand and it has to propagate forward at a constant velocity. However, if the cross-section of the tube varies, the shock wave problem becomes more complex [42].

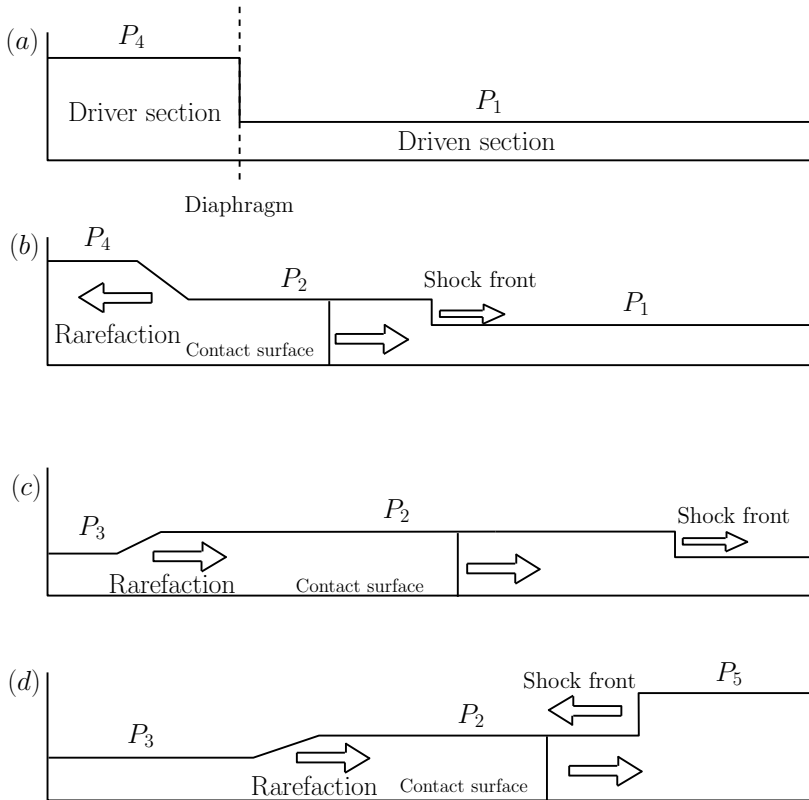


**Figure 3.8:** Pressure propagation in the shock tube [26].

### 3.2.1 The Ideal Gas Theory

The ideal gas theory is used to derive the pressures generated within a shock tube. The pressure  $P_2$  is given as a function of the driven pressure  $P_1$  [26],

$$P_2 = P_1 \left( 1 + \frac{2\gamma_1}{\gamma_1 + 1} (M_S^2 - 1) \right) \quad (3.12)$$

where,

$\gamma_1$  is the ratio of the specific heat at constant pressure to that at constant volume for the driven gas

$M_S$  is the Mach number

The Mach number is defined as the ratio of the incident shock wave velocity  $U_s$  to the speed of sound  $a_1 = \sqrt{\gamma_1 R T_1 / m_1}$  in an undisturbed low-pressure gas.  $R$  is the universal gas constant,  $T_1$  is the measured initial temperature and  $m_1$  is the molecular weight.

The pressure  $P_5$  that exist after the reflection of the shock from the end of the wall, depends on  $P_1$ ,  $P_2$  and  $\alpha_1 = (\gamma_1 + 1)(\gamma_1 - 1)$ ,

$$P_5 = P_2 \left( \frac{(\alpha_1 + 2)(P_2/P_1) - 1}{(P_2/P_1) + \alpha_1} \right) \quad (3.13)$$

The relationship between the driver pressure  $P_4$ , the driven pressure  $P_1$  and the Mach number  $M_S$  is expressed as,

$$\frac{P_4}{P_1} = \frac{1}{\alpha_1} \left( \frac{2\gamma_1 M_S^2}{\gamma_1 - 1} - 1 \right) \left( 1 - \frac{(1/\alpha_4)(\alpha_1/\alpha_4)(M_S^2 - 1)}{M_S} \right)^{-2\gamma_4/(\gamma_4 - 1)} \quad (3.14)$$

where,

$\gamma_4$  is the ratio of specific heats for the driver gas

$\alpha_4 = (\gamma_4 + 1)(\gamma_4 - 1)$

$a_4$  is the speed of sound in the undisturbed driver gas

Ideally, the response in the shock tube involves [43],

- No change in the initial gas
- An adiabatic process
- Instantaneously rupture of the diaphragms
- No reflected waves

However, the real shock tube behaviour deviates from the ideal response due to several factors. In the literature, Wright [44] derives an equation that relates the strength of the shock obtained in the tube, to the ratio of the pressures in the high and low pressure chambers ( $\frac{P_A}{P_1}$ ). When measuring the shock strength achieved for a given high to low pressure chamber ratio, he discovered that the shock wave was weaker than predicted. Several suggestions were made to explain his discoveries. The first reason involved the diaphragm and how it influences the flow in the tube. It is desirable to utilize a diaphragm that is as light as possible. This is due to the fact that the diaphragm only requires a small amount of energy to rupture. It is therefore an advantage to work with a diaphragm close to its bursting pressure. Secondly, pieces from the diaphragm tend to travel down the tube and consequently block the gas flow in the initial stages. This may lead to a delay in the creation of the shock wave. Figure 3.9a illustrates how the diaphragms tend to bow towards the low pressure chamber when subjected to pressure. This results in an initial gas flow that has velocity components directed towards the wall (Figure 3.9b), and not along the axis of the shock tube. Finally, viscous forces cause the shock front to decrease as it propagates down the shock tube [44].

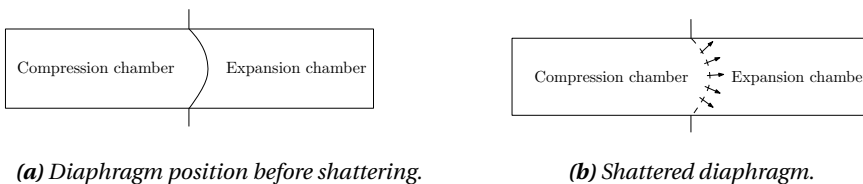


**Figure 3.9:** Illustration of the diaphragm in a shock tube[44].

### 3.3 Failure Modes

To fully understand the destructive effect an impulse load has on a structure, it is interesting to look at the possible failure modes. Menkes and Opat [4] have defined three main failure modes for clamped beams subjected to explosives. The failure modes are depicted in Figure 3.10.

- i. Mode **I** - Large inelastic deformations
- ii. Mode **II** - Tensile tearing at supports
- iii. Mode **III** - Shear failure at supports

These failure modes are found to apply for plates in general [6][45]. The plates failure modes are highly dependent on the geometry and boundary conditions [46]. A more precise characterization of square plates are achieved by subdividing failure mode **II** into [47][48],

Mode **II\*** - Partial tearing

Mode **IIa** – Complete tearing with increasing mid-point deformation

Mode **IIb** – Complete tearing with decreasing mid-point deformation

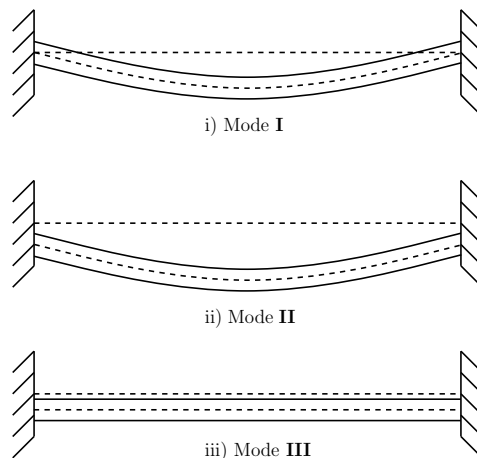


**Figure 3.10:** Failure modes [47].

### 3.4 Forming Limits

When subjected to blast loading, metal plates will most likely experience permanent deformations. It is therefore important to understand the material behaviour during plastic deformation. It is also necessary to be familiar with the interaction of the plastic deformation process and how the material is formed. In this section, forming limits and forming limit diagrams are therefore introduced. The following theory and equations are described by Hosford et. al [49].

During manufacturing, metal plates may be subjected to sheet-forming operations. The deformation is characterized by biaxial stretching and failure normally occurs when a sharp localized neck develops on the surface. It is important not to confuse localized necking with diffuse necking, which occurs when the load reaches its maximum value.

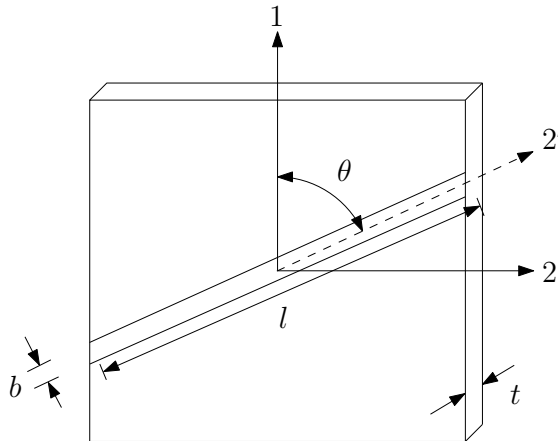


**Figure 3.11:** Localized neck and its coordinate axes.

Figure 3.11 depicts a thin sheet specimen subjected to uniaxial tension in the 1-direction. It is from now on presumed that the material obeys the power law hardening rule,  $\sigma_{eq} = Kp^n$ . The strain at the onset of diffuse necking is expressed as  $\varepsilon_1^* = n$ , where the star (\*) indicates the critical strain at instability. After being exposed to a considerable extension, a sharp localized neck is formed at an angle  $\theta$  to the loading axis. The width of the neck  $b$ , is typically in order of the sheet thickness  $t$ . In the literature [49] the

expression for the critical localized necking in uniaxial tension is derived and denoted  $\varepsilon_1^* = 2n$ . This demonstrates a factor two increase of the critical strain for localised necking compared with diffuse necking.

Due to the narrowness of the neck, the strain parallel to the neck  $d\varepsilon_{2'}$  must be zero. An expression for  $d\varepsilon_{2'}$  is given as,

$$d\varepsilon_{2'} = d\varepsilon_1 \cos^2 \theta + d\varepsilon_2 \sin^2 \theta = 0 \quad (3.15)$$

where  $d\varepsilon_1$  and  $d\varepsilon_2$  is the incremental major and minor principal strains in the plane of the sheet.

By assuming a constant strain ratio  $\beta = \frac{\varepsilon_2}{\varepsilon_1}$  during stretching, Equation (3.15) becomes,

$$\varepsilon_1 \cos^2 \theta + \beta \varepsilon_1 \sin^2 \theta = 0 \quad (3.16)$$

or

$$\tan \theta = \frac{1}{\sqrt{-\beta}} \quad (3.17)$$

Equation (3.17) indicates that  $\theta$  only has a real value if  $\beta$  is less than zero. This means that localized necking can not occur if the strain rate is constant or positive. Assuming a constant strain ratio is equivalent to assuming a constant stress ratio  $\alpha = \frac{\sigma_2}{\sigma_1}$ . When the stress becomes more biaxial,  $\alpha$  increases. By obtaining an expression of  $\beta$  based on  $\alpha$ ,  $\beta = (2\alpha - 1)(2 - \alpha)$ , it is seen that  $\beta$  becomes less negative as  $\alpha$  increases. This implies an increase of  $\theta$  as the stress becomes more biaxial.

The strain ratio influences the critical strain of necking. By applying the consistency criterion for volume, an expression relating  $\beta$ ,  $d\varepsilon_1$ ,  $d\sigma_1$  and  $\sigma_1$  is derived,

$$\frac{d\sigma_1}{\sigma_1} = (1 + \beta)d\varepsilon_1 \quad (3.18)$$

By applying the power law, the condition for localized necking is obtained,

$$\epsilon_1^* = \frac{n}{1 + \beta} \tag{3.19}$$

When  $\beta = \frac{1}{2}$ , the critical strain becomes equal to  $2n$ . For plane strain, the critical strain decreases to  $n$ .

Swift [49] showed that diffuse necking can occur when,

$$\epsilon_1^* = \frac{2n(1 + \beta + \beta^2)}{(\beta + 1)(2\beta^2 - \beta + 2)} \tag{3.20}$$

If the loading is applied with constant  $\alpha$  and consequently constant  $\beta$ , localized necking can not occur and stretching continues until the sheet fractures. However, sheet materials are never completely homogeneous and  $\alpha$  and  $\beta$  do change during stretching. Due to small inhomogeneities in geometry and material properties, local changes in the strain path occur and this leads to localized necking for positive values of  $\epsilon_2$  and hence for  $\beta > 0$ . This is the fundamental principle of the Marciniak-Kuczynski analysis[49].

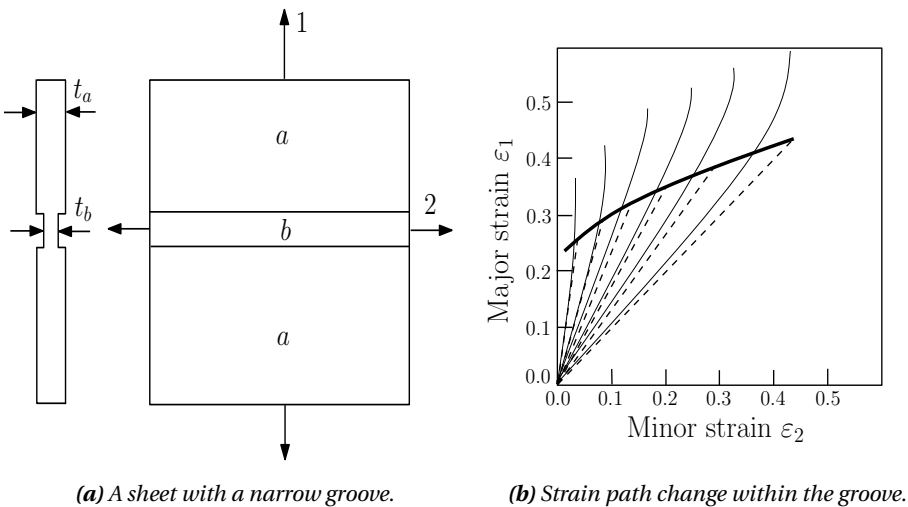


**Figure 3.12:** Marciniak-Kuczynski analysis[49].

Figure 3.12a illustrates a sheet with a narrow groove perpendicular to the major principal stress direction used for the Marciniak-Kuczynski analysis. The stress ratio  $\alpha_a$  and strain ratio  $\beta_a$  in region  $a$  are assumed constant, while  $\alpha_b$  and  $\beta_b$  in region  $b$  vary during plastic deformation. The strain in region  $b$  parallel to the groove is restricted by the uniform strain rate in region  $a$ , such that  $\varepsilon_{2b} = \varepsilon_{2a}$ .

When applying equilibrium requirements across the groove, the principal tractions inside and outside the groove should be equal,  $t_{1a} = t_{1b}$ . This is also expressed as,

$$\sigma_{1a}h_a = \sigma_{1b}h_b \quad (3.21)$$

The localization problem is solved by an incremental-iterative solution technique that requires the equilibrium across the groove, the constitutive relations and the compatibility equations to be satisfied throughout the deformation process. When deformation evolves,  $\Delta\varepsilon_{1a}$  becomes smaller and smaller compared with  $\Delta\varepsilon_{1b}$ . This corresponds to a  $\Delta\varepsilon_{2b} = \Delta\varepsilon_{2a} = \beta\Delta\varepsilon_{1a}$  that decreases compared with  $\Delta\varepsilon_{1b}$  and the flow in the groove proceeds towards plane strain. Localized necking occurs when the strain ratio reaches a critical value.

$$\beta = \frac{\Delta\varepsilon_{3b}}{\Delta\varepsilon_{3a}} = \beta_{cr} \quad (3.22)$$

This critical value corresponds to excessive thinning inside the groove.

The Marciniak and Kuczynski procedure can be used to calculate the shape of the right side of the forming limit diagram (FLD). Figure 3.12b depicts the strain paths in region  $a$  and  $b$  and the forming limit curve. The dashed and thin lines represent the strain paths in region  $a$  and  $b$ , respectively. The forming limit curve (FLC), which is displayed as the thick line, connects with the end points of the strain paths in region  $a$ . Initially, the strain paths in region  $a$  and  $b$  are similar. As the deformation process evolves, the two strain paths start to diverge and the strain path in region  $b$  tends towards plane strain with increasing strain rate. The forming limit is reached when the strain ratio  $\beta$  is equal to the critical value. It is important to know that the forming limit is based on the critical strains in region  $a$ .



### 3.4.1 Forming Limit Diagrams (FLD)

The major and minor principal strains ( $\epsilon_1$ ,  $\epsilon_2$ ) can be experimentally determined for different loadings along various paths. By plotting the strains in a diagram, a forming limit diagram (FLD) is constructed. This diagram can give indications of potential problems in the sheet forming and thereby prevent production failures. Figure 3.13 illustrates the difference between the experimental forming limit curve (FLC) and the theoretical curves for diffuse and localized necking.

By plotting local strains and comparing them with the FLD, potential trouble spots can be determined. If the measured strains are close to the FLC, there is a probability of weakness in the material. If the strains are located underneath the experimental FLC, localized necking is not a problem. A placement over the FLC indicates that the sheet may be exposed to local necking or fracture. By identifying the nature of the problem, it is possible to alter the sheet forming process such that production failures are reduced [49][50][51]. By creating a forming limit diagram for the experimental data obtained in this thesis, it is possible to investigate if the FLD provides reliable results.

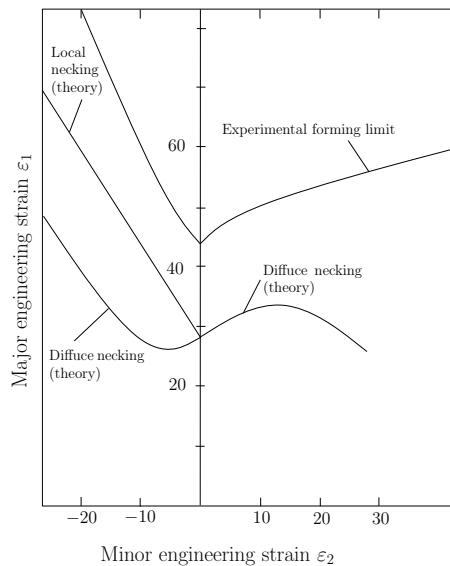


**Figure 3.13:** Experimental FLD with theoretical curves [49].

## 3.5 Material Characterization

In order to obtain a correct description of the material behaviour during loading, it is important to identify the material characterizations. In this section, relevant theory from the compendium Material Mechanics Part 1 from SIMLab [52] will be presented.

### 3.5.1 Strains and Stresses

In this thesis, all the material characteristics will be collected from multi uniaxial tensile tests. Strains and stresses, which are defined based on the initial cross section  $A_0$ , are referred to as engineering strains  $\varepsilon_e$  or stresses  $\sigma_e$  expressed in Equations (3.23) and (3.24), respectively. These equations are only valid for infinite small deformations, where the relation between strain and stresses are linear. Equation (3.25) illustrates the generalized Hooke's law which only applies for the elastic domain.

$$\varepsilon_e = \frac{\Delta L}{L_0} \quad (3.23)$$

$$\sigma_e = \frac{F_L}{A_0} \quad (3.24)$$

$$\sigma = E\varepsilon \quad \text{and} \quad \varepsilon = \frac{\sigma}{E} \quad (3.25)$$

Here,  $\Delta L$  is an increment change of the specimen,  $L_0$  is the initial gauge length,  $F_L$  is the force from the tensile test and  $E$  is Young's modulus.

For large deformations, the change of the cross section  $A$  has to be encountered for. The logarithmic strain  $\varepsilon_l$  (true strain) and the Cauchy stress  $\sigma_t$  (true stress) can be derived by assuming a constant volume. Based on the measurements from the tensile tests, the engineering stresses and strains are gathered. Subsequently the true stresses and strains are computed as,

$$\varepsilon_l = \ln\left(\frac{L}{L_0}\right) = \ln(1 + \varepsilon_e) \quad (3.26)$$

$$\sigma_t = \frac{F_L}{A} = \sigma_e(1 + \varepsilon_e) \quad (3.27)$$

The total strain  $\varepsilon$  is the sum of the elastic  $\varepsilon^e$  and plastic  $\varepsilon^p$  strain. The elastic strain is defined from Hook's law, hence the plastic strain is expressed as,

$$\varepsilon^p = \varepsilon - \varepsilon^e = \varepsilon - \frac{\sigma}{E} \quad (3.28)$$

### 3.5.2 Necking

When performing a uniaxial tensile test, the specimen reaches a critical point. Diffuse necking is defined as the point where the cross-section area rapidly decreases, simultaneously as the specimen increases its elongation. This is shown in Equation (3.29). Diffuse necking occurs when the material has reached its maximum strength  $d\sigma_e=0$ , as shown in Figure 3.14.

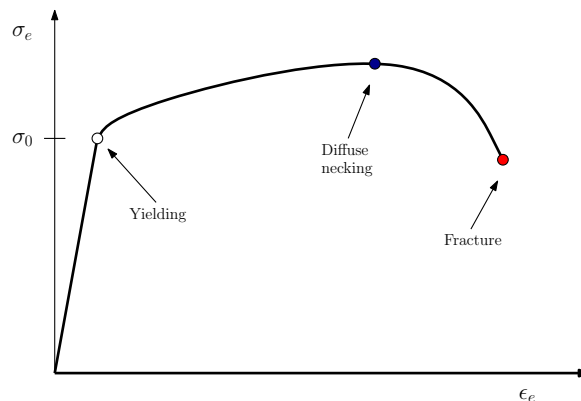


**Figure 3.14:** Engineering stress-strain curve in tension[52].

In the true stress vs. logarithmic strain relation, the diffuse necking is also expressed as,

$$\frac{d\sigma_t}{d\varepsilon_l} = \sigma_t \quad (3.29)$$

The data from the tensile test are only valid until diffuse necking occur, thus the remaining information is incorrect and extrapolation is necessary.

## 3.6 Constitutive Equations

Constitutive equations are necessary to provide a mathematical description of the material behaviour. In this thesis, plates are subjected to blast loading and large strains are likely to occur. Consequently, when the material experience yielding, the deformation, loads and stresses are non-linear and history-dependent. To precisely describe the material behaviour of the plates, the Johnson-Cook material model is applied.

### 3.6.1 The Johnson-Cook Material Model

The Johnson-Cook material model is frequently used in structural impact problems. It can be calibrated from tensile tests at various strain rates and temperatures.

A thermoelastic-thermoviscoplastic constitutive model derived by Børvik et al. [53][54], is applied in the numerical simulations of this thesis. It is based on the assumptions that the material is isotropic with small elastic strains and finite plastic strains and rotations.

The rate of deformation tensor is decomposed into elastic, plastic and thermal parts,

$$\mathbf{d} = \mathbf{d}^e + \mathbf{d}^p + \mathbf{d}^t \quad (3.30)$$

The elastic term of the tensor can be written as,

$$\mathbf{d}^e = \frac{1+\nu}{E} \boldsymbol{\sigma}^{\nabla J} - \frac{\nu}{e} \text{tr}(\boldsymbol{\sigma}^{\nabla J}) \mathbf{I} \quad (3.31)$$

where,

$E$  is Young's modulus

$\nu$  is Poisson's Ratio

$\mathbf{I}$  is the  $2^{nd}$  order unit tensor

$\boldsymbol{\sigma}^{\nabla J}$  is the Jaumann rate of the Cauchy stress tensor  $\boldsymbol{\sigma}$

The plastic rate of deformation tensor is defined by the associated flow rule as,

$$\mathbf{d}^p = \dot{p} \frac{\partial f}{\partial \boldsymbol{\sigma}} = \frac{3}{2} \dot{p} \frac{\boldsymbol{\sigma}'}{\sigma_{eq}} \quad (3.32)$$

where  $\dot{p}$  is the equivalent plastic strain rate.

The thermal rate of deformation tensor is expressed as follows,

$$\mathbf{d}^t = \alpha \dot{T} \mathbf{I} \quad (3.33)$$

where  $\dot{T}$  and  $\alpha$  represent the rate of temperature increase and the linear thermal expansion coefficient, respectively.

By including isotropic hardening, thermal softening and the von Mises yield criterion, the yield function is written as,

$$f(\boldsymbol{\sigma}, R, T) = \sigma_{eq}(\boldsymbol{\sigma}) - \sigma_0(T) - R(p, T) \quad (3.34)$$

The equivalent stress  $\sigma_{eq}$ , the yield stress  $\sigma_0$  and the hardening variable  $R$  are defined as,

$$\sigma_{eq} = \sqrt{\frac{3}{2} \boldsymbol{\sigma}' : \boldsymbol{\sigma}'}, \quad \sigma_0 = A[1 - (T^*)^m], \quad R = Bp^n [1 - (T^*)^m] \quad (3.35)$$

where,

$\boldsymbol{\sigma}'$  is the deviatoric stress tensor,  $\boldsymbol{\sigma}' = \boldsymbol{\sigma} - 1/3(\boldsymbol{\sigma})\mathbf{I}$

$A, B, n, m$  are material parameters governing strength, strain hardening and thermal softening

$T^*$  is the homologous temperature,  $T^* = (T - T_0)/(T_m - T_0)$

$T_0, T_m$  are the room and melting temperature of the material

The constitutive relation suggested by Johnson and Cook [53], has a multiplicative formulation given by a strain hardening term, strain-rate sensitivity and temperature softening,

$$\sigma_{eq}(\boldsymbol{\sigma}) = (\sigma_0(T) + R(p, T)) \left(1 + C \ln(\dot{p}^*)\right) = (A + Bp^n) \left(1 + C \ln(\dot{p}^*)\right) \left[1 - (T^*)^m\right] \quad (3.36)$$

Here  $\dot{p}^* = \dot{p}/\dot{p}_0$  is the normalized plastic strain rate. However, when  $\dot{p}^* < 1$  the strain-rate sensitivity term can exhibit an unphysical softening effect. To avoid this, the modified Johnson-Cook model is used in this thesis [54],

$$\sigma_{eq}(\boldsymbol{\sigma}) = (A + Bp^n) \left(1 + \dot{p}^*\right)^C \left[1 - (T^*)^m\right] \quad (3.37)$$

Having defined the yield function, a constitutive relation expressing the equivalent plastic strain rate is developed,

$$\dot{p} = \begin{cases} 0 & \text{for } f \leq 0 \\ \dot{p}_0 \left[ \frac{\sigma_{eq}(\boldsymbol{\sigma})}{\sigma_0(T) + R(p, T)} \right]^{\frac{1}{C}} - 1 & \text{for } f > 0 \end{cases} \quad (3.38)$$

where  $\dot{p}_0$  is a user-defined reference strain rate and  $C$  is a material constant governing strain-rate sensitivity. It should be noted that due to a slightly difference in Equation (3.36) compared with Equation (3.37), the  $C$  parameter can be different in the two formulations.

In shock tube problems it is reasonable to assume adiabatic conditions. The following term for the temperature evolution is then applicable,

$$\dot{T} = \frac{\chi}{\rho C_p} \boldsymbol{\sigma} : \mathbf{d}^p = \frac{\chi}{\rho C_p} \sigma_{eq} \dot{p} \quad (3.39)$$

where  $\chi$  is the Taylor-Quinney coefficient,  $\rho$  is the density and  $C_p$  is the specific heat capacity. The Taylor-Quinney coefficient represents the proportion of plastic work converted into heat, and is assumed  $\chi = 0.9$  for adiabatic conditions. This means that 90% of the work converts to heat, and 10% transfers to the material.

### 3.7 Digital Image Correlation

To process the experimental data obtained in this thesis, digital image correlation (DIC) is performed. This is a post-processing technique for measuring strains and displacements in experimental solid mechanics. DIC is an accurate, cheap and simple way of gathering material information. In addition, DIC makes it easy to examine the deformation pattern and the crack propagation.

The DIC technique compares the image of a specimen at a deformed stage (current configuration) to an image of the specimen at a reference stage (reference configuration). In more detail, it measures the alteration of the pixels in the images over time. The surface of the material needs to exhibit characteristic points such that the system can trace the deformation. Consequently a field of both two-dimensional (2D) and three-dimensional (3D) deformation vectors can be constructed [55]. In this thesis, 2D-DIC will be used in the material tensile tests, while 3D-DIC will be performed of the shock tube experiments.

In 2D-DIC, the deformation of the specimen is described by a set of parameters. These parameters are optimized to minimize the differences in grayscale values between the reference and current image. The optimization is performed by employing the Newton-Raphson iteration method, where the correlation function  $F$  in Equation (3.40) may be used as the objective function [56]. This is called a subset-based DIC approach.

$$F = \sum_{i \in \Omega} (I_r(\mathbf{X}_i) - I_c(\mathbf{x}_i))^2 \quad (3.40)$$

where,

$I_r$  is the reference image

$I_c$  is the current image

$\mathbf{X}$  refers to the image coordinates in the reference configuration

$\mathbf{x}$  refers to the image coordinates in the current configuration

$i$  represents a specific pixel

$\Omega$  is the set of pixels within the subset at the reference configuration



3D-DIC involves a typical stereovision system that employs two or more cameras to record digital images of the specimen from two or more viewpoints. This makes 3D-DIC theoretically capable of obtaining accurate, in-plane surface deformations even when the specimen is undergoing large, three-dimensional rigid body rotation and translation [57]. Figure 3.15 displays a typical 3D-DIC setup where  $P$  represents an arbitrary initial point and  $P'$  is the location after deformation.

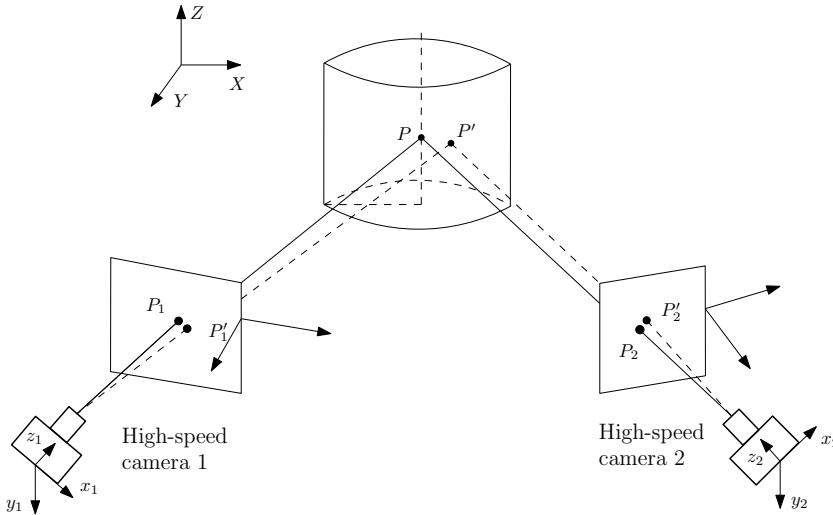


**Figure 3.15:** Mathematical model of a 3D-DIC system [58].

In addition to subset-based DIC, a finite element approach is possible. The FE-based DIC, formulates the correlation problem as a finite-element decomposition on a mesh of Q4 elements. The correlation applies global optimization on a mesh of elements, and the nodal displacements in the mesh are optimized. This differs from the subset-based DIC approach where individual optimization of subsets are applied, and optimizing involves the displacement of the center point and the displacement gradient of the subset.

The success of the correlation and the quality of the images depend on several parameters. Some of the most important parameters involve the contrast and speckle size of the recorded grayscale pattern, in addition to the subset size and the digitization level of the grayscale values.



# Chapter 4

## Materials

In this thesis, two materials are used when performing the experimental research in the shock tube. The materials are,

- Docol 600 DL steel
- Aluminium alloy EN AW-1050A-H14

While all the steel plates are produced by SSAB, the aluminium plates have two different manufacturers. Hindalco industries and Hydro have produced the 0.8mm and 2.0mm aluminium plates, respectively. The two next sections are based on general theory about the two materials. There are, however, some variations between the theoretical material characteristics and the given values in the material card appointed by the manufacturers. The material cards with the exact material characteristics are therefore enclosed in Appendix B.

To find the material characteristics of the materials, tensile tests are performed. Subsequently the data are processed using 2D-DIC. The tensile tests are also studied numerically, by applying the FE program Abaqus CAE.

## 4.1 Docol 600 DL Steel

Docol is a cold-rolled, high strength steel produced by SSAB in Sweden. It contains ferrite, which is soft and contributes to good formability, and martensite, which hardens the material. In addition, it has good weldability due to the low content of alloying elements. There are several advantages using Docol DL; weight reduction, simplified manufacturing, increased safety, longer lifecycle, reduced total cost, among others [59].

Common areas of applications of the Docol 600 DL, are in tubes and as safety components in cars. Its chemical composition in addition to physical and mechanical properties are displayed in Tables 4.1 and 4.2, respectively. Note that the steels are classified based on the lowest tensile strength, which is 600 MPa for Docol 600 DL.

**Table 4.1:** Chemical composition of Docol 600 DL steel [59].

Composition [%]	Chemical Element					
	C	Si	Mn	P	S	Al
General	0.100	0.400	1.500	0.010	0.002	0.040

**Table 4.2:** Physical and mechanical properties of Docol 600 DL steel [59] [60].

$\nu$ [-]	$\rho$ [kg/m <sup>3</sup> ]	$E$ [MPa]	$G$ [MPa]	$R_{p,02,min}$ [MPa]	$R_{p,02,max}$ [MPa]	$R_{m,min}$ [MPa]	$R_{m,max}$ [MPa]
0.30	7800	210 000	81 000	280	360	600	700

Steel has been used in structural applications since the middle of the 18<sup>th</sup> century. Steel is a ductile material with high yield strength. This means that the material can undergo large plastic deformations before failure, which is an important attribute when it comes to blast loading. Steel has also great strength, uniformity and a relatively good fatigue strength. Combined with a high strength to weight ratio it makes steel an appropriate choice for structures such as high-rise buildings and long-span bridges [61].

One major disadvantage is that steel is susceptible to corrosion when exposed to air, water or humidity. This results in higher maintenance costs. Steel is also vulnerable to fire since the strength is reduced when exposed to high temperatures [62].

## 4.2 Aluminium alloy EN AW-1050A-H14

The aluminium alloy EN AW-1050A-H14 is a preferable alloy for general sheet metal work where moderate strength is required. Typical applications are containers, foils, radiator tubes and piping. The chemical composition of the alloy is given in Table 4.3.

**Table 4.3:** Chemical composition of aluminium alloy EN AW-1050A-H14 [60].

Composition [%]	Chemical Element							
	Mg	Mn	Fe	Si	Cu	Zn	Ti	Al
General	0.05	0.05	0.40	0.25	0.05	0.07	0.05	99.50

The alloy can be identified using the four digit system for wrought alloy composition designation. In Europe, the alloys are recognized with the preface EN and AW which indicates European Normative Aluminium Wrought alloys. Since this aluminium alloy consist of 99.50 % aluminium it is characterized as technically pure. This entails a part of the 1xxx series, implying there is no major alloying element [63]. In this group, the aluminium purity is of 99.00% and greater. The two last digits of the 1xxx series, indicates the percentage of aluminium, while the second digit describes modifications in impurity limits or alloying elements. Hence, the material used in the experiments has aluminium purity of 99.50% and the zero indicates that the unalloyed aluminium has natural impurity limits [63]. The high purity leads to a rate sensitive alloy, meaning that the material is dependent on the rate of plastic straining [64].

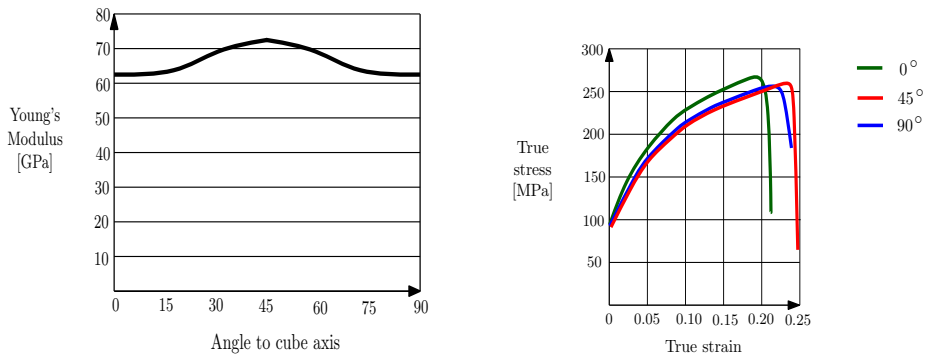
Wrought alloys are initially cast as ingots or billets. To get the desired shape, cold work in form of rolling, extruding, bending etc. is necessary. When the metal is subjected to cold work, dislocations are prevented from moving. This leads to an increase in the material strength. The wrought alloys are divided into two categories, heat-treatable and non-heat treatable alloys. The H14 in the alloy name indicates the affiliation to the latter group. The purity of the alloy result in a softness in the metal and to add strength, strain hardening is necessary. The last digit in H14, indicates that the alloy has been cold worked to a half hard condition. Due to a balance between strain hardening and recovery effects, stress-saturation rapidly occurs resulting in a flattening of the strain-stress curve [63].

Table 4.4 gives the physical and mechanical properties of the alloy. It is common to

**Table 4.4:** Physical and mechanical properties of aluminium alloy EN AW-1050A-H14 [60].

$\nu$ [-]	$\rho$ [kg/m <sup>3</sup> ]	$E$ [MPa]	$G$ [MPa]	$R_{p,02,min}$ [MPa]	$R_{p,02,max}$ [MPa]	$R_{m,min}$ [MPa]	$R_{m,max}$ [MPa]
0.33	2710	71 000	27 000	90	105	110	115

assume uniform properties in all directions, even though some degree of anisotropy is always present. The level of anisotropy depends on several parameters, including alloy composition and process history. By studying Figure 4.1a, one can see how Young's modulus changes with the rotation of the cubic axis. By rotating the axis from 0° or 90° to 45°, the E-modulus increases from 63 to 72 GPa which is equivalent to 15%. Figure 4.1b illustrates the anisotropy of the strength and elongation to failure. The sample cut parallel to the rolling direction usually differs from the samples cut in the direction of 45° and 90°. The two latter samples are nearly identical and display a lower strength than the longitudinal sample. The elongation to failure exhibits a 25 % deviation between the 45° and 0° sample [61].

**(a)** Young's modulus and the rotation of the cubic axis.**(b)** Anisotropy of the strength and elongation to failure.**Figure 4.1:** Anisotropy in aluminium [61].

When aluminium is exposed to dynamic loading, inertia and wave-propagation effects complicate the stress and strain states. The dynamic properties of aluminium alloys have been investigated numerous times and the results from some of the studies are displayed in Figure 4.2. The figure presents the strain-rate sensitivity parameter versus the static flow stress for different aluminium alloys. The result shows an increase of rate sensitivity as the material strength decreases, or as purity increases [64].

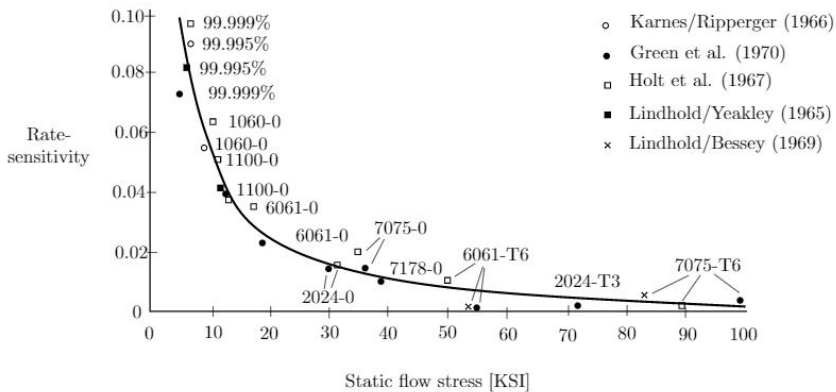


**Figure 4.2:** Strain-rate sensitivity of aluminium alloys [64].

In recent years there has been a greater focus on the use of aluminium in structural applications. The main reason is the low density of aluminium which results in a greater strength to weight ratio than for steel. This implies less material, simpler assembly and easier transportation. Aluminium also has superior corrosion resistance. The absence of solute alloys leads to less disrupting of the protective native oxide film and it is therefore fewer anodic/cathodic reaction sites where corrosion can occur. This entails less maintenance costs and it even suggest that aluminium can be used without surface protection. Without solute or precipitated alloy elements present, plastic deformation of the metal is possible. This leads to an aluminium alloy that has high formability and workability. The use of aluminium is also beneficial for the environment, since recycling of aluminium is possible without loss of properties. In addition, the required energy for recycling is only 5% of the energy to produce the primary aluminium.

However, there are some less favourable properties that a structural engineer needs to be aware of. The low modulus of elasticity leads to greater deformation and sensitivity

for instability. Due to the low weight, high cycle fatigue is more decisive than with steel. Finally, aluminium has a low melting point. This leads to a loss of the mechanical and physical properties at low temperatures, starting at 100°C [61].



### 4.3 Experiments

To collect relevant material data, uniaxial tensile tests of both steel and aluminium are performed. The tensile tests of the dog-bone specimens are performed in the Zwick Roell Z030 machine, displayed in Figure 4.3. To represent a quasi-static test, the specimens are pulled with a loading velocity of 2.1mm/min. Both the machine data and a camera, Prosilica GL2450, register the deformation. While the machine has a frequency of 10Hz, the camera captures four pictures per second. These pictures are in the next section used in a 2D-DIC analysis to process the collected data. The machine data are used for verification.



*Figure 4.3: Test specimen in the Zwick Roell Z030 machine.*

The materials are tested for two different thicknesses, 2.0mm and 0.8mm, and three rolling directions. The latter test is necessary to reveal any dependence of direction, thus if the material is isotropic or anisotropic. The various rolled orientations are the longitudinal direction  $0^\circ$ , the transverse direction  $45^\circ$  and the normal direction  $90^\circ$ . Figure 4.4 illustrates the rolling directions of the plates. To verify the reliability of the material, three tests in each rolling direction are performed. This entails a total of 36 tensile tests.

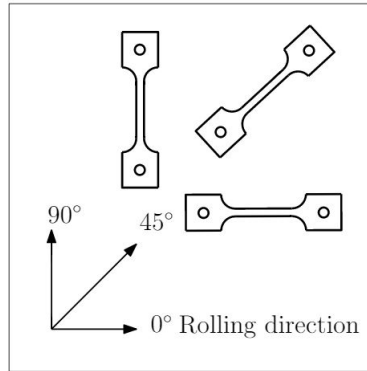


**Figure 4.4:** The different rolling directions on a plate.

The 2.0mm samples are pulled by bolts in the testing machine, while the thinner samples are pulled by clamps. This is necessary to prevent local deformation in the bolt holes. An extensometer with gauge length 40mm is used in 12 of the tests, one for each of the thicknesses and in all the three rolling directions. The extensometer is removed when the specimen achieves maximum strength.

Each specimen is measured and the initial geometries are displayed in Tables B.1 and B.2 in Appendix B. A variation in the thickness of the dog-bone specimens is registered, which is natural since the measurements are carried out using a calliper with an inaccuracy of  $\pm 0.3$ . Figure 4.5 shows the nominal geometry of a chosen dog bone specimen.

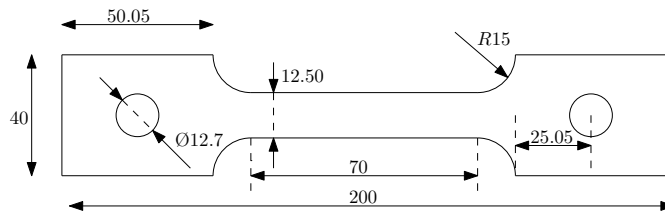


**Figure 4.5:** Nominal geometry of a dog bone specimen in [mm].

## 4.4 Material Identification

A suitable material description is highly important. If the material parameters are insufficient, it is difficult if not impossible to predict the structural response during impact of a blast wave. There are two possible approaches of identifying the material characteristics. By using a direct modelling method, material parameters are determined based on 2D-DIC. By applying an inverse modelling method, the calibrated data are modified to fit the experimental data. Both methods are carried out in the following sections.

### 4.4.1 Post Processing and Calibration

The collected data from the camera and the machine are processed. The force-displacement curves for all the samples are displayed in Section B.2.2 in Appendix B. Since the 2D-DIC data coincide with the machine data, the information obtained from the 2D-DIC can be used in the calibration of the material.

The raw data have to be processed and analysed to determine the material properties. Young's modulus  $E$ , indicates the stiffness of the material. This parameter is based on the binding forces between the atoms, hence the behaviour should be the same for all materials consisting of the same atoms. The tensile tests performed in the laboratory are not accurate enough to provide a correct Young's modulus, subsequently the material data have to be corrected using Equation (4.1). Here,  $E_{meas}$  is determined by linear regression in the elastic area for each engineering stress-strain curve.

$$\varepsilon_{ce} = (\varepsilon_{me} - \Delta\varepsilon_e) - \left( \frac{E_{corr} - E_{meas}}{E_{corr} E_{meas}} \right) \sigma_{ce} \quad (4.1)$$

where,

$\varepsilon_{ce}$  is the corrected engineering strain

$\varepsilon_{me}$  is the measured engineering strain

$\Delta\varepsilon_e$  is a possible deviation in strain at origin

$E_{corr}$  is the correct elastic modulus

$E_{meas}$  is the measured elastic modulus

$\sigma_{ce}$  is the measured stress

To find the yield strength of the material, the true plastic strain is plotted against the true stress. For a high-strength steel, the crossing from elastic to plastic strain is usually gradual. Consequently, it can be difficult to determine a distinct yield point. The 0.2% offset  $\sigma_{0.2}$  is therefore commonly used to establish an approximation of the yield strength. An illustration on how the yield stress  $\sigma_0$  and the 0.2% offset are located is shown in Figure B.9 in Appendix B.

Since the material data are only valid until necking, the curves have to be extrapolated with a suitable work hardening rule. Two isotropic hardening rules are displayed in Equations (4.2a) and (4.2b). It should be noted that for large strains, the Voce rule will converge to a constant value, while power law will increase infinitely.

$$R = K p^n \quad (\text{Power law}) \quad (4.2a)$$

$$R = \sum_{i=1}^n Q_{Ri} (1 - \exp(-C_{Ri} p)) \quad (\text{The Voce rule}) \quad (4.2b)$$

where,

$R$  is the hardening variable

$p$  is the accumulated plastic strain

$K$  &  $n$  are hardening parameters in power law

$Q_{Ri}$  &  $C_{Ri}$  are hardening parameters in the Voce rule

Before the curves are extrapolated, the data are smoothed and divided into 100 points with equal distance. To extrapolate these points a curve fitting tool in MATLAB is applied [65].

### Results of Docol 600DL Steel

It is desirable to investigate the significance of the rolling process, and evaluate if it influences the stress and strain distribution of the material. By studying Figure 4.6, it is evident that the various curves are fairly similar. They display the same shape, but the maximum tensile strength appears to vary for the different test specimens. There is a tendency towards higher tensile strengths for the thicker samples. This may be explained by the rolling process of the material. However, the difference in material behaviour is minimal and for practical applications the material can be assumed isotropic. Due to missing DIC data, one of the tensile tests are disregarded in Figure 4.6.

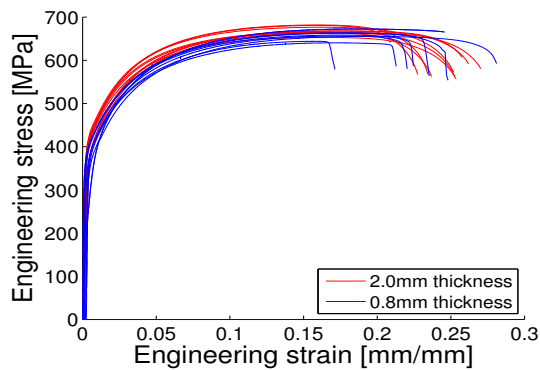


**Figure 4.6:** Steel specimens with thicknesses of 2.0mm and 0.8mm.

The curves in Figures 4.7a and 4.7b show an equal distribution of the engineering stress and strain in the three rolling directions. Since the engineering stress and strain curves exhibit the same trend, the mean curve for each rolling direction are chosen for further processing. By studying Figure B.5a in Appendix B, one of the curves show an abnormal behaviour. This is caused by an error in the clamping mechanism, which failed to hold the specimen sufficiently still. This test is therefore omitted when evaluating the curves.

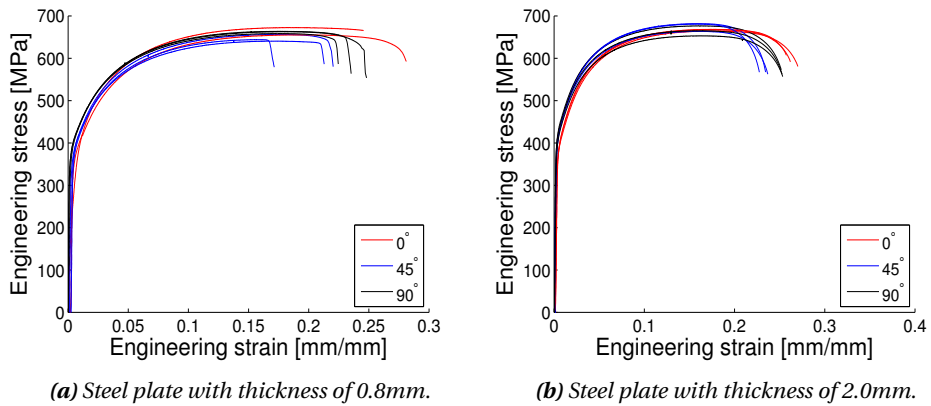


**Figure 4.7:** Results from the tensile tests in the three rolling directions.

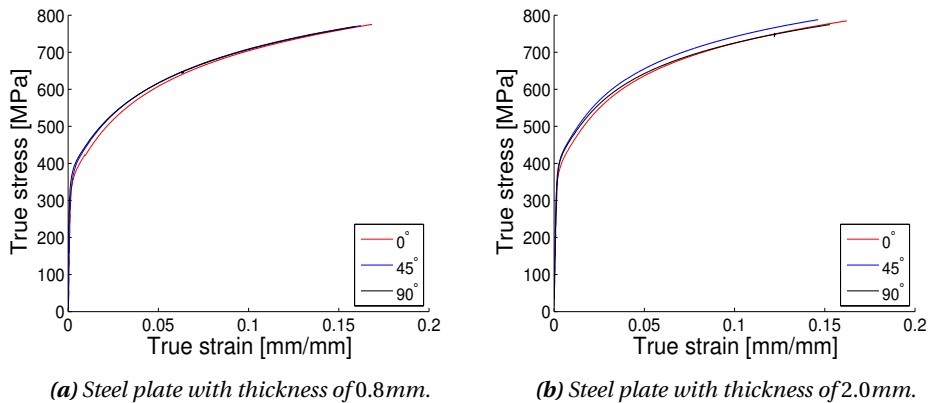


**Figure 4.8:** True stress-strain curves for the chosen specimens.

As mentioned in Section 4.4.1, correction of the curves are necessary in order to obtain the correct elasticity modulus. The results are seen in Figures B.7a and B.7b in Appendix B. From the corrected data, the true stress-strain relations are obtained. The true stress-strain curves are only plotted until diffuse necking and the maximum force is found to localize this point. The true stress-strain relation for the chosen tests are shown in Figure 4.8.

The expected maximum force is obtained by multiplying the tensile strength from the material card with the nominal cross-section. This corresponds to a  $F_{max}$  of 6.77kN and 16.60kN for the 0.8mm and 2.0mm plates, respectively. The measured  $F_{max}$ ,  $\sigma_0$  and  $\sigma_{0.2}$  from the tensile tests are displayed in Table 4.5. By comparing the measured values of  $F_{max}$  with the expected values, the thickest plates experience a deviation of up to 3.13%. This is slightly greater than the maximum deviation of 2.95% for the 0.8mm plates. However, since variations naturally occur within a material, these deviations are acceptable. By studying Table 4.2 in Section 4.1, it is seen that the 0.2% offset for Docol 600DL steel is given a value between 280MPa and 360MPa. Since the manufacturer informs about a variety in  $\sigma_{0.2}$ , it is also likely that variations between the calibrated values and the material card may occur.

**Table 4.5:** Calculated parameters for the chosen steel specimens.

Test	$F_{max}$ [kN]	$\sigma_0$ [MPa]	$\sigma_{0.2}$ [MPa]
S08-02	6.6	318.7	369.6
S08-04	6.9	306.8	384.8
S08-08	6.9	352.5	393.0
S20-03	16.6	345.1	394.0
S20-06	16.8	361.7	418.4
S20-09	17.1	303.5	413.7

As mentioned in Section 4.4.1, extrapolation of the true stress-strain curves are necessary to describe the material behaviour after necking. The hardening parameters used in the curve fitting tool in MATLAB are found in Appendix B in Table B.3. In Figure 4.9, the results of applying isotropic hardening with both the Voce rule and the power law are depicted. Since all the test specimens display the same trend, it is sufficient to only plot one curve. When necking is reached, it is assumed that the experimental data will follow a path somewhere between the Voce and Power approximations. Since there is no experimental data in the post-necking regime, it is difficult to predict the most representative hardening rule.

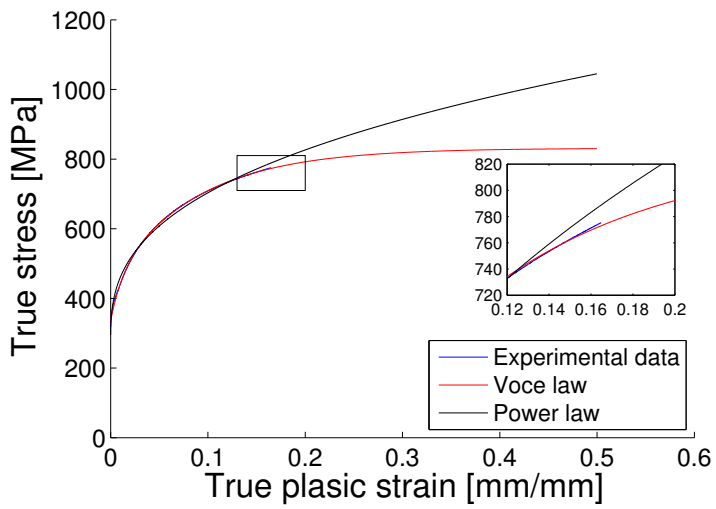


**Figure 4.9:** Different hardening rules for steel.



### Results of Aluminium Alloy EN AW1050A-H14

The results from the aluminium tensile tests are plotted and displayed in Figure 4.10. It is evident that aluminium is more dependent of the rolling direction compared with steel. This is illustrated by great variations in both yield strength and elongation. It is observed that for aluminium, the thinnest specimens accumulate highest tensile strengths. The material card of the 2.0mm aluminium plate displayed in Appendix B, reveals that the tensile strength of the aluminium alloy may vary between 105 and 145MPa. Figure 4.10 are in accordance with the information given in the material card.

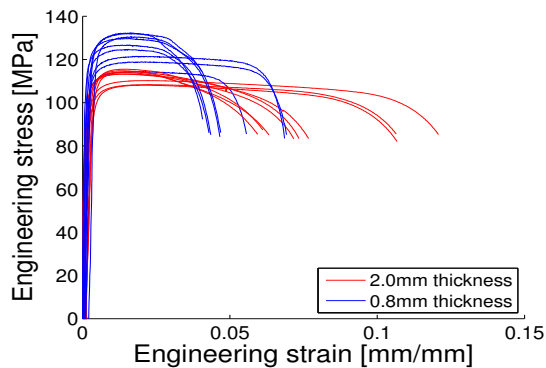


*Figure 4.10: Aluminium specimens with thicknesses of 2.0mm and 0.8mm.*

The curves in Figure 4.11 show a similar trend as described in Figure 4.1b in Section 4.2. While the tensile tests performed in the rolling direction of  $45^\circ$  and  $90^\circ$  display more or less the same stress-strain curves, the rolling direction of  $0^\circ$  displays lower yield strengths and larger elongations. By evaluating Figure 4.11, it is evident that aluminium is an anisotropic material. However, Grytten et al. [66] have investigated the effects of anisotropy on plates made of the aluminium alloy AA50836-H116. The study indicates that anisotropy does not seem to influence the response of structures made of this alloy. Due to the observations of this study, anisotropy of the aluminium alloy EN AW1050A-H14 is neglected and the material is further treated as isotropic.

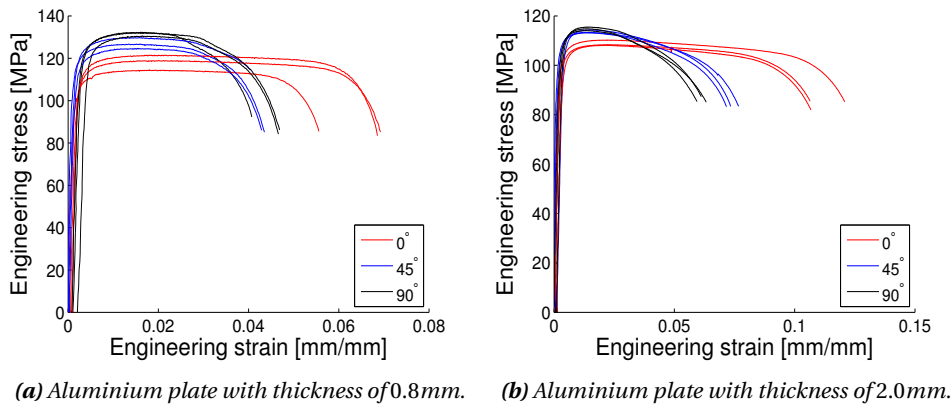


**Figure 4.11:** Results from the tensile tests in the three rolling directions.

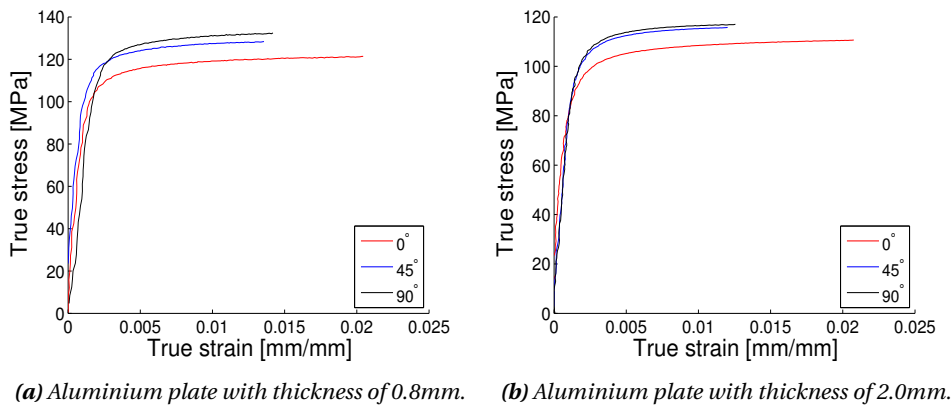


**Figure 4.12:** True stress-strain curves for the chosen specimens.

The correction procedure that were conducted for steel is also carried out for aluminium. The corrected curves for the three most representative tests are shown Figures B.8a and B.8b in Appendix B. This leads to the true stress-strain curves displayed in Figure 4.12.

The expected maximum forces are calculated by using the information in the two material cards appointed by the suppliers. This results in values of 1.17kN and 2.93kN for the 0.8mm and 2.0 specimens, respectively. Table 4.6 displays the measured  $F_{max}$ ,  $\sigma_0$  and  $\sigma_{0.2}$  from the tensile tests. For the thinner samples, the greatest difference between the expected and calculated  $F_{max}$  is 4.27%. It is observed that all the 2.0mm specimens underestimates the maximum force. The two material cards have appointed the same 0.2% offset with a value of 110MPa. While the 2.0mm specimens show a great correla-

tion with the material card, the deviations are greater for the thinner specimens. All the results are, however, still acceptable.

**Table 4.6:** Calculated parameters for the chosen aluminium specimens.

Test	$F_{max}$ [kN]	$\sigma_0$ [MPa]	$\sigma_{0.2}$ [MPa]
A08-02	1.1	97.1	112.7
A08-04	1.2	108.6	121.6
A08-09	1.2	83.8	123.5
A20-03	2.7	86.3	102.0
A20-04	2.8	88.6	109.3
A20-09	2.9	96.7	110.8

The extrapolated curve for one of the test specimens is displayed in Figure 4.13, while the parameters obtained by the curve fitting are shown in Table B.4 in Appendix B. The figure implies that the approximation by Voce rule provides the best fit of the aluminium specimen. The Voce rule converges to a constant value and this coincide with the phenomenon that the stress and strain curve for aluminium normally levels out for large plastic strains.

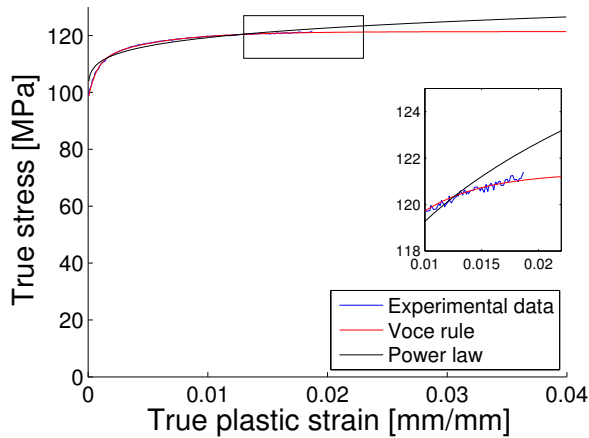


**Figure 4.13:** Different hardening rules for aluminium.

### 4.4.2 Modelling of the Tensile Test using Abaqus CAE

Until now, a direct modelling approach has been used when characterizing the material parameters. To verify the direct approach, the tensile test for a specimen of both materials and thicknesses are simulated in Abaqus CAE. The materials are assumed isotropic and it is therefore not necessary to perform a simulation in each of the rolling directions. The simulations are run using a non-linear implicit analysis. This integration method is suitable for smooth nonlinearities (e.g a plasticity problem) [67].

It is decided to obtain two numerical models, one for each hardening rule. The power law is a integrated function in Abaqus, where the parameters  $\sigma_0$ ,  $K$  and  $n$  (see Table B.3 and B.4) can be directly implemented. However, for the Voce rule, the simulations have to be run with a customized material card for each of the specimens. The material cards are made using SIMLab Metal Model (SMM) [68], and the numerical model is taken from SIMLabs toolbox [69]. Note that SMM defines the Voce rule somewhat different than in Section 4.4.1,

$$R = \sum_{i=1}^N R_i = \sum_{i=1}^N Q_{Ri} \left( 1 - \exp\left(-\frac{\theta_{Ri}}{Q_{Ri}} p\right) \right) \quad (4.3)$$

where  $\theta_{Ri} = C_R Q_{Ri}$ .

It should be mentioned that it is not necessary to obtain a numerical model for each of the hardening rules. However, it was decided to utilize the SIMLab Toolbox. Despite two different numerical models, the response of the two specimens should be the same. Both models are modelled with nominal geometry and material properties as displayed in Tables 4.2 and 4.4, respectively.

For the model with power hardening, the dog-bone specimen is modelled as displayed in Figure 4.14. To decrease the simulation time, only a quarter of the specimen is modelled, hence two symmetry planes. The specimen is modelled as 3D deformable shell planar with S4R elements (a shell 4-node element with reduced integration).

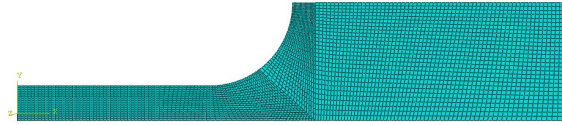


**Figure 4.14:** Numerical model for the simulation with power hardening law.

The model from SIMLabs toolbox is shown in Figure 4.15. This is a 3D deformable model with volume elements *C3D8R* (an 8-node linear brick with reduced integration).

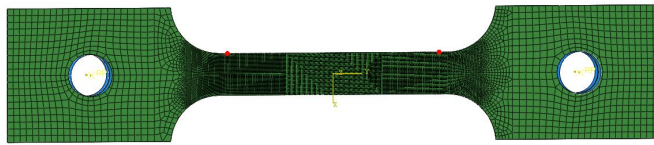


**Figure 4.15:** Numerical model for the simulation with the Voce hardening rule.

## Modification of the Tensile Test

By comparing the force-displacement curves from the experimental data and the results from the Voce and power simulations, neither of the responses give a satisfying description of the experimental data. In an attempt to improve the material model, the strain-rate hardening term is added to the material description. Neither this gives sufficient results, and therefore an additionally term in the Voce rule is added. It is not a common procedure to use three Voce terms in a material model.

Initially, two terms of the Voce rule is used when describing the material. By only including two terms, there may be a lack of flexibility describing the post-necking regime. Before deciding which parameters in Equation (4.3) to modify, two different scenarios are considered,

- Scenario 1: The first term  $R_1$  and second term  $R_2$  saturate before necking, and the third term does not
- Scenario 2: The first term  $R_1$  and second term  $R_2$  does not saturate before necking

Since the first term describes the initial curvature of the stress-strain curve, this curve will most likely to saturate before necking. Consequently, there is a greater focus on the second and third term when modifying the curve. For both scenarios there are a modifying procedure to optimize the hardening curve [70]. Since both materials act in accordance with scenario 1, only the third term is altered. This is a time consuming operation that demands experience when varying the parameters  $Q_{Ri}$  and  $\theta_{Ri}$ . In order to achieve accurate material parameters, the modification is performed by Dr. Morin [71].

Since it is natural to assume the possibility of fracture in the forthcoming shock tube experiments, a failure criterion is defined. The Cockcroft-Latham (CL) model is a ductile damage model, used for both steel and aluminium. In SMM this model is defined by reducing the Extended-Cockcroft Latham (ECL) by setting  $\phi = 1$  and  $\gamma = 1$  [68],

$$\dot{D} = \frac{1}{W_C} \left\langle \phi \frac{\eta_I}{\eta_{eq}} + (1 - \phi) \left( \frac{\eta_I - \eta_{III}}{\eta_{eq}} \right) \right\rangle^\gamma \eta_{eq} \dot{p} \rightarrow \dot{D} = \frac{\langle \eta_I \rangle}{W_C} \dot{p} \quad (4.4)$$

where  $W_C$  is the failure parameter and  $\langle \eta_I \rangle$  is the first principal value of the over-stress tensor. Since the materials are isotropic this value is equal to the Cauchy stress.

While Table 4.7 displays the Voce parameters used in the initial FE simulation with two Voce terms, Table 4.8 shows the Voce parameters with three terms for both the direct and the inverse modelling method. By comparing the values obtained with direct and inverse modelling, it is evident that some significant modifications have been made, especially for the aluminium material. When further referring to the direct modelling methods, it implies the use of the two terms Voce rule in Table 4.7. While the initial Voce fit indicates the use of the direct modelling method in Table 4.8, the optimized Voce rule represents the inverse modelling method.

**Table 4.7:** Strain hardening parameters - Voce rule with two terms.

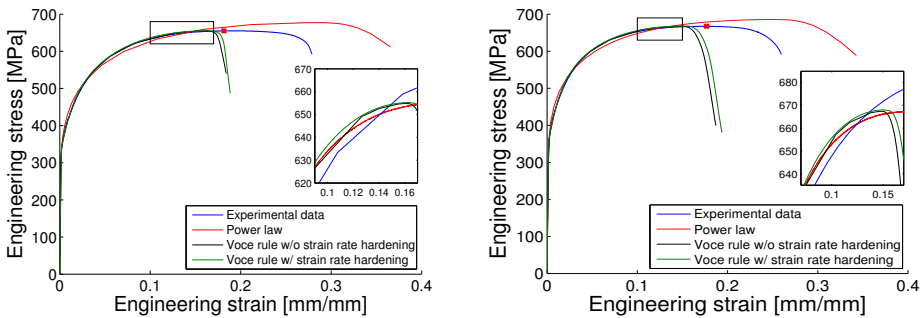
Test	$A$ [MPa]	$Q_{R1}$ [MPa]	$Q_{R2}$ [MPa]	$C_1$ [MPa]	$C_2$ [MPa]
Docol 600 DL 0.8mm	334.5	117.1	379.7	84.9	11.4
Docol 600 DL 2.0mm	355.6	345.0	135.0	11.8	85.8
EN AW-1050A-H14 0.8mm	97.6	13.2	10.6	1458.0	185.9
EN AW-1050A-H14 2.0mm	86.8	8.5	16.5	103.3	993.6

**Table 4.8:** Strain hardening parameters - Voce Rule with three terms.

Parameters	Docol 600 DL				EN AW-1050-H14			
	0.8mm		2.0mm		0.8mm		2.0mm	
	Direct	Inverse	Direct	Inverse	Direct	Inverse	Direct	Inverse
$A$ [MPa]	330.0	330.0	330.0	330.0	100.0	100.0	95.0	95.0
$Q_{R1}$ [MPa]	27.5	27.5	43.9	43.9	8.6	8.590	5.510	5.510
$Q_{R2}$ [MPa]	164.6	164.6	179.4	179.4	10.7	10.7	8.2	8.2
$Q_{R3}$ [MPa]	358.3	392.0	329.7	392.0	2.3e4	4.0	8.1e4	17.5
$C_1$ [MPa]	1051.4	1051.4	1399.2	1399.2	1786.9	1786.9	1353.2	1353.2
$C_2$ [MPa]	43.0	43.0	48.0	48.0	284.9	284.9	252.1	252.1
$C_3$ [MPa]	7.4	5.9	7.5	6.4	4.3e-3	20.0	1.2e-3	5.570
$C$ [-]	1.0e-3	5.0e-3	1.0e-3	5.0e-3	1.4e-2	1.0e-2	1.4e-2	1.0e-2
$W_C$ [MPa]	-	815.0	-	880.0	-	120.0	-	200.0

**Results of Docol 600DL Steel**

In Figure 4.16, the responses of the 8.0mm and 2.0mm steel specimen are displayed. The simulations are run with the two terms Voce rule (from Table 4.7) and either with or without the strain rate hardening parameter  $C = 0.001$ . The red dot on the experimental data indicates necking of the material. Both thicknesses seem to display a similar behaviour. The only difference is a slightly earlier neck of the Voce curves for the 2.0mm test. It is evident that the power law exhibit a to stiff behaviour, hence there will be a greater focus on adapting the Voce rule.



(a) Engineering stress-strain curves for the 0.8mm specimen.

(b) Engineering stress-strain curves for the 2.0mm specimen.

**Figure 4.16:** FE simulations with hardening (Direct modelling method).

In Figure 4.17, the Voce rule with three terms and strain rate hardening are displayed. With three Voce terms the model is able to represent the experimental data beyond necking. The curve displaying the initial Voce fit, neck to early. The steel material exhibit a large strain hardening up to necking, hence the third Voce term will most likely underestimate the strain hardening. This is illustrated by the initial curve, and the third Voce term is increased to get a better fit.



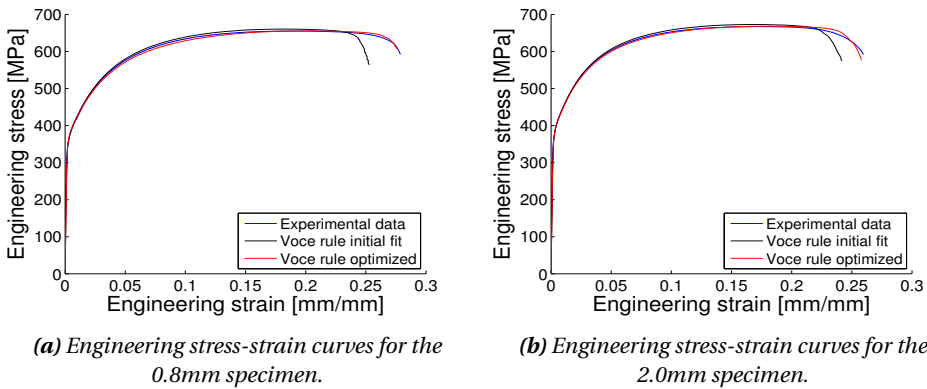
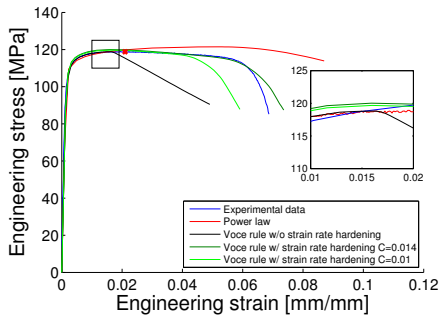


**Figure 4.17:** Optimization of the three term Voce rule (Inverse modelling method).

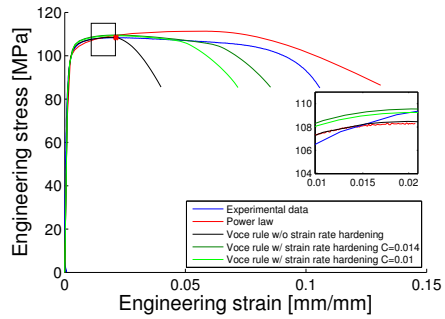
### Results of Aluminium alloy EN AW-1050A-H14

The results of the FE model for the 0.8mm and 2.0mm specimens, are displayed in Figure 4.18. The power law exhibit a too steep slope after necking, and does not give a sufficient representation of the material behaviour. The engineering stress-strain response for the Voce curve without hardening, displays a curve that neck too rapidly for both specimen thicknesses. This may be a consequence of a rate sensitive behaviour and a missing viscoplastic material description.

In addition to the analyses that include the Voce rule and the power law, two extra simulations are run with an additional rate sensitive hardening term. The  $C$  parameter describes the rate sensitivity, hence a lower value exhibits a more saturated curve. An initial strain hardening parameter  $C$  of 0.014 [72] is used to describe the material. However, in an attempt to decrease the initial curvature,  $C$  is set to 0.01. The simulations run with strain rate hardening show a significant improvement. For the 0.8mm specimen, the FE-model with  $C = 0.014$  exhibits adequate results compared with the experimental data.



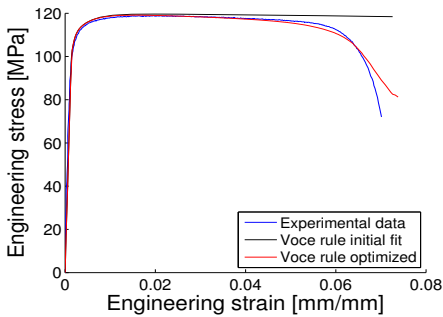
(a) Engineering stress-strain curves for the 0.8mm specimen.



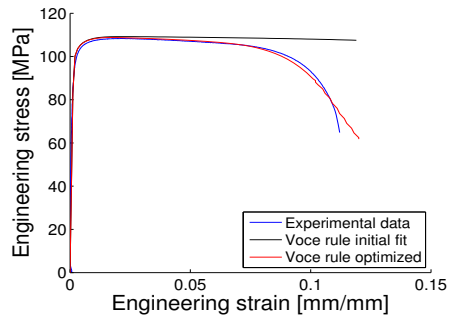
(b) Engineering stress-strain curves for the 2.0mm specimen.

Figure 4.18: FE simulations with hardening (Direct modelling method).

As for steel, the aluminium model is run with a three terms Voce rule and with strain rate hardening. The aluminium specimen exhibits a small strain hardening up to necking, and the third Voce term will most likely overestimate the large strain hardening as illustrated in the initial FE model. By optimizing the parameters, the Voce rule gives a good fit as shown in Figure 4.19.



(a) Engineering stress-strain curves for the 0.8mm specimen.



(b) Engineering stress-strain curves for the 2.0mm specimen.

Figure 4.19: Optimization of the three term Voce rule (Inverse modelling method).

# Chapter 5

## Experimental Work

The experimental work is performed in the newly established shock tube facility at SIM-Lab. An introduction of this laboratory instrument is therefore necessary. The pressure distribution in the shock tube is validated, and the results from the shock tube experiments are calibrated and evaluated.

### 5.1 The Shock Tube Facility at SIMLab

The shock tube utilized in the experiments of this thesis, is built by SIMLab at NTNU. The shock tube, which has a total length of 18.275m, is made from the stainless steel P355NH, and is designed according to EN13445–1 : 2009 [73]. An overview of the design is depicted in Figures 5.1 and 5.2.

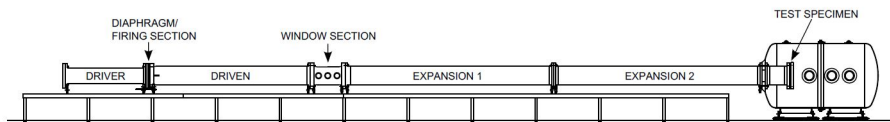


*Figure 5.1: Sketch of the SIMLab shock tube facility [74].*



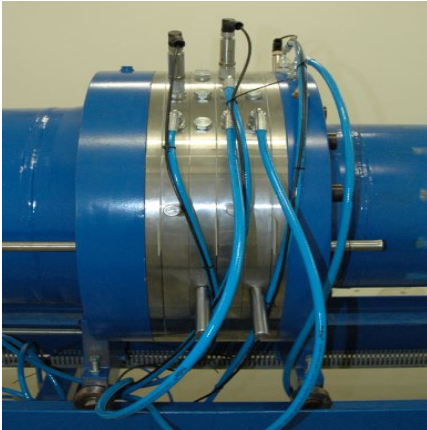
*Figure 5.2: The shock tube facility at SIMLab.*

The shock tube is divided into the following five sections:

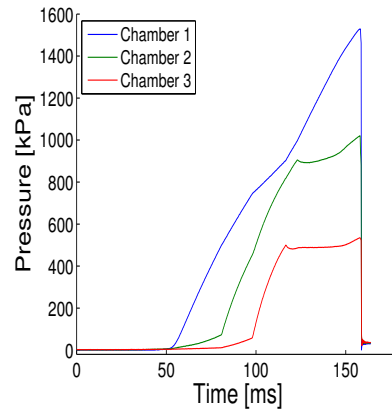
- The driver section
- The firing section
- The driven section
- The window section
- The dump tank

The different parts of the tube can sustain various maximum working pressures. The driver section is limited to 17MPa, while the driven section, window section and dump tank are limited to 10MPa, 5MPa and 1.4MPa, respectively.

The driver tube is 2.02m long and has a inner diameter of 0.331m. The volume is adjustable with a maximum value of 173.8 dm<sup>3</sup>. In the experiments performed in this thesis, the volume is set to 23.2 dm<sup>3</sup> by using aluminium inserts, placing the inner wall 0.27m from the firing section. The volume is specifically chosen to recreate the desired time and pressure distribution of an explosion.



(a) The mechanism of the firing section.



(b) Typical pressure-time history of the chambers in the driver.

**Figure 5.3:** The firing section.

The firing section is displayed in Figure 5.3a. This section includes two intermediate pressure chambers that can be separated by diaphragms. The diaphragms can be made from different materials, depending upon the strength of the shock wave required. In this thesis, the polyester Melinex is used. To obtain different firing pressures, the placement and combination of the diaphragms are adjusted. SIMLab has performed a number of experiments to collect data of the pressure tolerances for different combinations of the membranes. This data is available in Table C.1 in Appendix C. There is always a possibility that the membranes used for achieving a certain driver pressure are not available. The problem is solved by using a membrane composition that results in a slightly higher pressure than intended. Figure 5.3b illustrates how the pressure is built up in the shock tube. The filling starts with the driver chamber (chamber 1) and thereby the two intermediate chambers (chambers 2 and 3). The chambers are all filled close to the diaphragms tolerance. While the intended firing pressure is 1500 kPa, the Figure 5.3b displays a pressure of 1530 kPa. In this calibration experiment, the firing section is divided by  $2 \times 0.25$  mm thick Melinex diaphragms at three locations. By studying the tolerance level in Table C.1, a total firing pressure of  $3 \times 5.8$  bar = 17.4 bar = 1740 kPa is indicated. This is higher than the actual firing pressure obtained in the experiment. In order for the diaphragms to rupture, venting of the intermediate chamber closes to the driver is necessary. When venting is initiated, the pressure drops leading to a firing

pressure less than the desired value. Consequently, in order to achieve a certain firing pressure, the driver section should be filled with an additional 5-10% of the pressure. A program developed by SIMLab, monitors the gas-filling and ensures a controlled and automatic process [73].

The firing section is followed by the driven section. The cross-section is initially circular with a transition to a  $0.3 \times 0.3 \text{ m}^2$  square cross-section. As mentioned in the previous section, a shock wave is generated when the diaphragms burst, leading to natural propagation from the driver to the driven section.

At the end of the tube, a dump tank is installed. In the experiments performed in this thesis, this is where the test objects are placed. An explanation of how the plates are clamped to the end flange is given in Section 5.3.1. If the dump tank is open, it serves to decrease the pressure in the system after the experiment.

It should be mentioned that there is another possibility regarding the placement of the test specimen. By placing it in the window section in Figure 5.4, the flow around the object can be studied. The object is then attached to the bottom of the section using bolts. To record the effects of the shock wave, a camera placed on the side of the windows or sensors attached directly on the test object can be used.

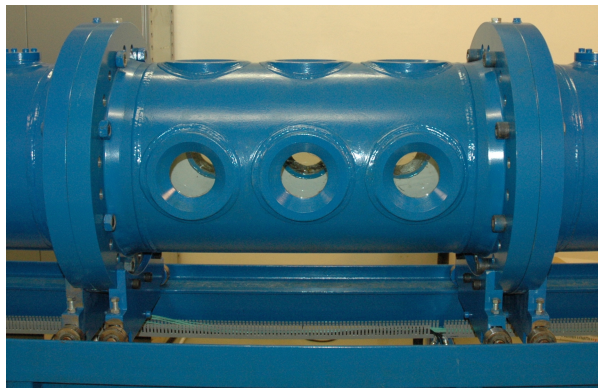
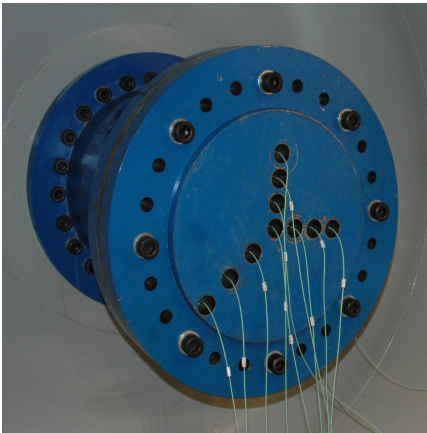


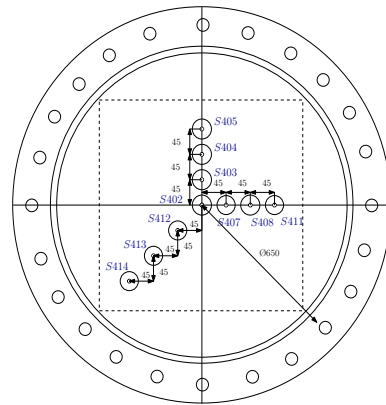
*Figure 5.4: The window section.*

## 5.2 Verification of the Pressure

Before performing the plate experiments, it is important to investigate the pressure distribution in the shock tube. Ideally, the distribution should be uniform over the cross-section when encountering the metal plate. To examine the applied pressure, the experimental setup in Figure 5.5 is used. Ten sensors are placed along the vertical, horizontal and diagonal line of a rigid plate to measure the pressure distribution on the plate.



(a) Sensors on the rigid plate.



(b) Numeration of the sensors [mm].

**Figure 5.5:** Experimental set up of the verification tests.

The experiment is performed for seven different driver pressures; 500, 1000, 1500, 2000, 2500, 3500 and 4000 kPa. To examine the reliability of the results, the experiments of the first five pressures are carried out three times. The membrane compositions for the different pressures are shown in Table C.2 in Appendix C.

The results of the actual firing pressures are depicted in Table 5.1. As seen, it is difficult to obtain a firing pressure identical to the intended driver pressure, and consequently the repeatable tests show some diversity in the peak reflected pressures. However, these differences are not significant and the experiments display a good reliability.

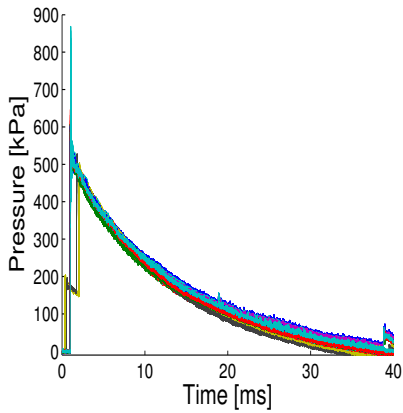
Three typical curves of the pressure-time history are displayed in Figure 5.6. While Figure 5.6a shows an experiment with uniform pressure distribution, Figure 5.6b displays some variation of the pressure distribution for the different tests. As seen in Table 5.1, the firing pressure of Test 4 deviates the most from the chosen driver pressure. The

test displays a peak reflected pressure almost 10 % higher than the two other repeatable tests for the same experiment. The experiment with a driver pressure of 2500 kPa expose the most consistent results for the three tests. The finale figure (Figure 5.6c) illustrates disturbance on the pressure-time history. This is caused by debris of ruptured diaphragms that are located inside the shock tube during the experiment. It should be noted that some of the curves only display the positive phase of the pressure-time history. This is a result of saving a too short time period of data. The pressure-time histories for the remaining experiments are displayed in Section C.2.1 in Appendix C.

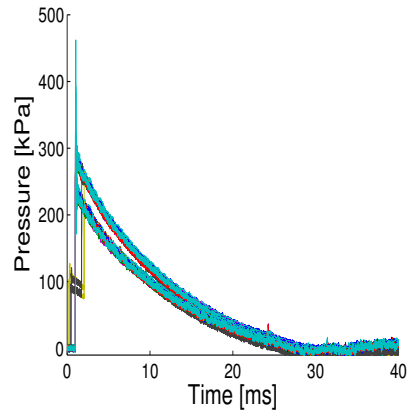
**Table 5.1:** *Different driver and firing pressures of the calibration experiments.*

Test #	Driver pressure [kPa]	Firing Pressure [kPa]
1	500	570
2		520
3		520
4	1000	1120
5		1020
6		1020
7	1500	1570
8		1530
9		1530
10	2000	2000
11		2070
12		2080
13	2500	2500
14		2520
15		2530
16	3500	3580
17	4000	4080

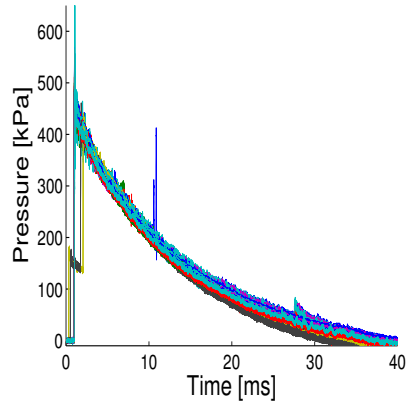




(a) Uniform pressure distribution of Tests 13,14,15.



(b) Variation in the pressure distribution for Tests 4,5,6.



(c) Disturbance in the pressure-time history of Tests 10,11,12.

**Figure 5.6:** Typical pressure-time histories from the calibration experiments.

As already mentioned, Figure 5.5b illustrates the placement of the different sensors located directly on the rigid plate. By studying the figure closely, it is seen that not all sensors are represented in the drawing. This is reasoned in that these sensors are located along the driven section. The sensors S409 and S410 are placed closest to the test specimen. Figure 5.7 illustrates the pressure-time history of a calibration test for three specific chosen sensors; sensor 402 located on the rigid plate and sensors 409 and 410 located in front of the plate. Since the pressure distribution is uniform, it is sufficient to only display the pressure-time history of the sensor located in the center of the rigid plate. The pressure-time history illustrates how the shock wave encounters sensor 409 and 410 before impacting the plate. A more detailed explanation of how the blast wave encounters the different sensors is given in the next section.

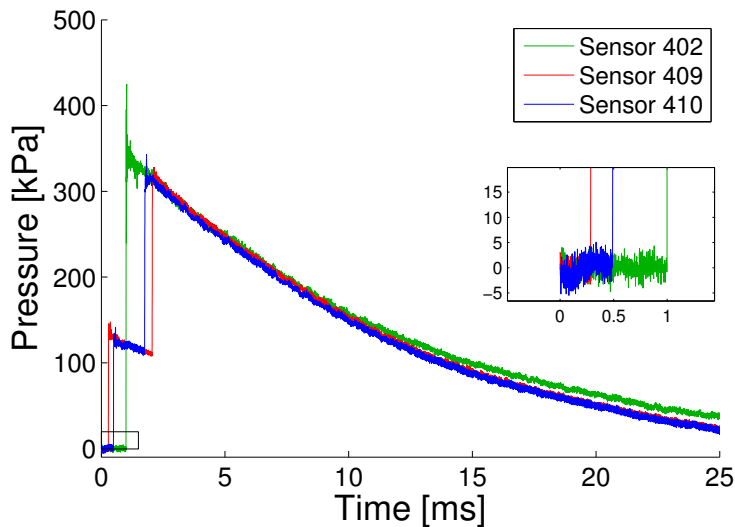


**Figure 5.7:** Illustration of the pressure-time history for a calibration test, displaying sensors 402, 409 and 410.

### 5.2.1 Ideal Gas Theory

As mentioned in section 3.2, it is possible to apply the ideal gas theory to obtain the pressures that generate within the shock tube. Table 5.2 displays the ideal gas parameters that are used in the calculations of the different pressures. The values of the universal gas constant  $R$  and the specific heat ratio  $\gamma_1$  are found in the literature [75] [76]. The molecular weight  $m_1$  is calculated for air and the temperature is assumed to be  $20^\circ\text{C}$ .

**Table 5.2:** Ideal gas theory parameters.

$\gamma_1$ [-]	$R$ [J/mol × K]	$T_1$ [K]	$m_1$ [kg/mol]
1.401	8.3145	293	0.02897

By determining the velocity of the initial shock wave, the Mach number can be calculated. The Mach number is used in the derivation of the pressure behind the incident shock wave  $P_2$  in Equation (3.12) and the pressure behind the first reflected shock wave  $P_5$  in Equation (3.13). The calculated velocities, Mach numbers and different pressures for the calibration tests are found in Table 5.3. As seen, only one test for each of the calibration experiments is chosen.

**Table 5.3:** Velocity, mach number and pressures for the calibration tests.

Test #	$U_s$ [m/s]	$M_s$ [-]	$P_1$ [kPa]	$P_2$ [kPa]	$P_5$ [kPa]
2	427.40	1.25	100.31	166.04	265.60
5	490.00	1.43	100.31	222.41	453.32
8	500.10	1.46	100.31	232.54	490.85
11	510.20	1.49	100.32	242.91	530.31
14	556.60	1.62	100.31	290.13	723.10
16	561.80	1.64	100.50	298.31	757.46
17	598.90	1.75	100.48	341.90	954.79

In order to compare the results from the ideal gas theory with the experimental data, the incident and peak reflected pressures must be obtained. The incident peak pressure is found by subtracting the pressure behind the incident shock wave from the initial pressure in the driven section,  $P_2 - P_1$ . The reflected overpressure is calculated by subtracting  $P_5$  from  $P_1$ . The results are displayed in Table 5.4.

Table 5.4 reveals great variations in the accuracy of the incident and peak reflected pres-

sure when applying the ideal gas theory. Even though Test 5 gives a great representation of the experimental peak reflected pressure, it overestimates the incident pressure by 26 %. On the contrary, the results from Test 11 are in good accordance with the incident pressure, but it underestimates the peak reflected pressure by 24 %. These observation applies for most of the tests. By evaluating the results, it is evident that the ideal gas theory does not give an optimal representation of the incident and peak reflected pressures of these calibration experiments. The main reason may be the assumption of a constant blast wave through the shock tube. This is a simplification since the velocity decreases as the blast wave travels through the shock tube.

**Table 5.4:** Incident and reflected peak pressure from the calibrations tests.

Test #	Firing pressure [kPa]	$P_2 - P_1$			$P_5 - P_1$		
		Ideal theory [kPa]	Exp. data [kPa]	Error [%]	Ideal theory [kPa]	Exp. data [kPa]	Error [%]
2	520	65.7	63.2	4.0	165.2	201.8	18.1
5	1020	122.1	96.9	26.0	353.0	350.5	0.7
8	1530	132.2	119.9	10.3	390.5	400.7	2.5
11	2070	142.6	145.4	1.9	430.0	567.9	24.3
14	2520	189.8	170.3	11.5	622.8	637.7	2.3
16	3580	197.8	199.7	1.9	657.0	738.9	11.1
17	4080	241.4	226.3	6.7	854.3	936.8	8.8

### 5.3 Component Test

Table 5.5 gives an overview of the nine component tests conducted in this thesis. It displays the chosen driver pressures, the actual firing pressures and the specific numbers given to each of the experiments. The number is based on the formulation  $MX.Y-ZW$ . While the  $M$  represents the material,  $X.Y$  gives the thickness of the plates in mm. The two last digits  $ZW$  symbolize the intended driver pressure given in bar. The plates applied in the experiments are made of the two materials introduced in Chapter 4. The different membrane compositions of the intended driver pressures are displayed in Section C.3 in Appendix C.

As Table 5.5 indicates, it was not performed any experiments of the 2.0mm steel plates. Since laboratory work and processing of the experimental data are time consuming, it was decided to omit experimental research and perform a numerical study of these plates instead.

**Table 5.5:** Experiments performed in the shock tube.

Material		Driver pressure [kPa]	Firing pressure [kPa]	Test [MX.Y-ZW]
Steel	0.8mm	1500	1623	S0.8-15
		2500	2522	S0.8-25
		3500	3735	S0.8-35
Aluminium	0.8mm	500	560	A0.8-5
		750	820	A0.8-7.5
		1000	1116	A0.8-10
	2.0mm	1500	1527	A2.0-15
		2500	2521	A2.0-25
		3500	3701	A2.0-35

### 5.3.1 Experimental setup

The steel and aluminium plates have the same dimension of  $0.625 \times 0.625 \text{ m}^2$ , but only a area of  $0.3 \times 0.3 \text{ m}^2$  is exposed to the blast wave. In an attempt to achieve fixed boundary conditions, the plates are clamped to the end flange using M24 bolts and a clamping frame. The clamping set-up is shown in Figure 5.8, and the bolts are tighten using a torque wrench of 200Nm.

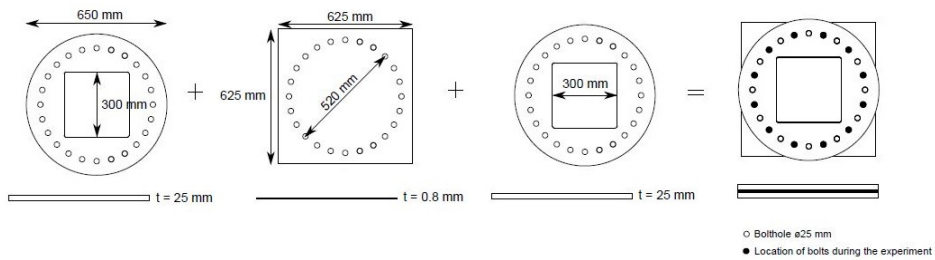


**Figure 5.8:** Clamping of the plate [74].

To capture the shock wave response, two pressure sensors are placed at the end of the driven section. The pressure-time history is recorded by sensors 409 and 410, which are denoted 1 and 2 in Figure 5.9. Two Phantom v1610 high-speed cameras are used to capture the structural response. As seen in Figure 5.9, the separation angle between the optical axes of the cameras are approximately  $60^\circ$ . The cameras record data with a frequency of 21 kHz, combined with an image resolution of  $896 \times 800$  pixels and 12-bit grey level digitization. To synchronize the pressure recordings with the images from the high-speed cameras, an independent data acquisition system from National Instruments (NI USB-6356) is used.

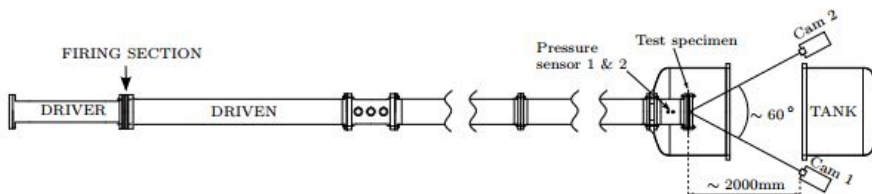


**Figure 5.9:** Sketch of the setup [73].

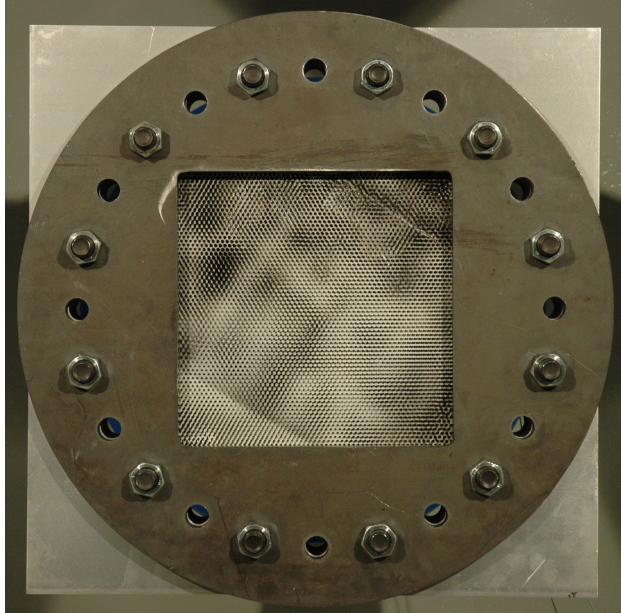


*Figure 5.10: Plate located in the clamping frame.*

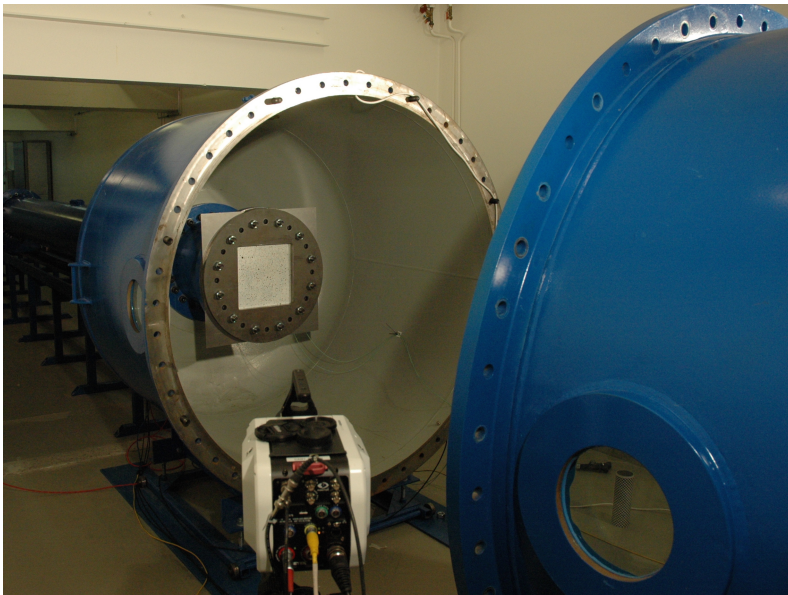


*Figure 5.11: The dump tank and camera setup.*

### 5.3.2 Calibration of the pressure

Figure 5.12a describes the pressure-time history of the two sensors placed in front of the plate. The shock wave encounters sensor 409 before 410. This corresponds to sensor 409 reaching its initial peak before sensor 410 on the plot. Subsequently, the incident overpressure drops, representing the wave traveling from the latter sensor to the plate. The wave is thereby reflected and encounters sensor 410 before 409. This implies that sensor 410 is first to reach the second peak. The positive phase of the pressure ends when the pressure decreases to its initial value. The pressure then briefly encounters the negative phase before the pressure increases and surpasses the initial value again.

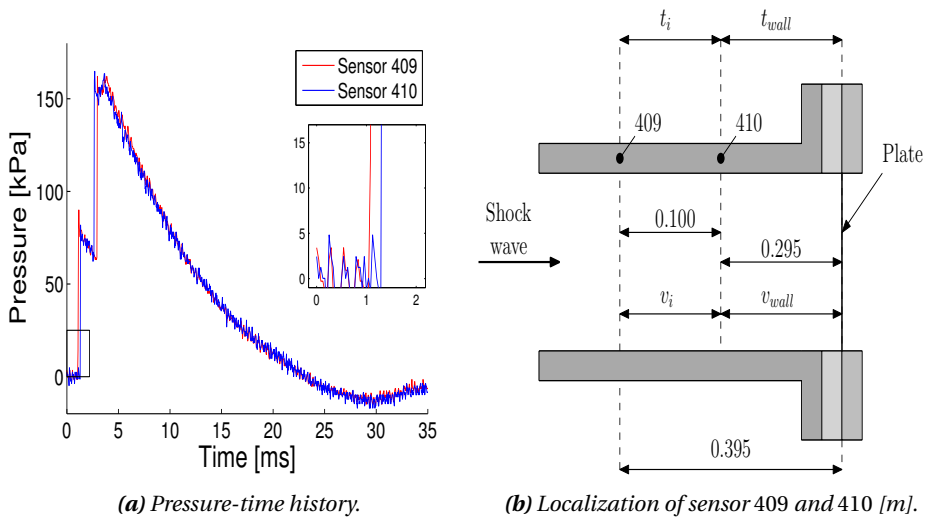


**Figure 5.12:** Illustration of how to find the exact pressure subjected to the plate.

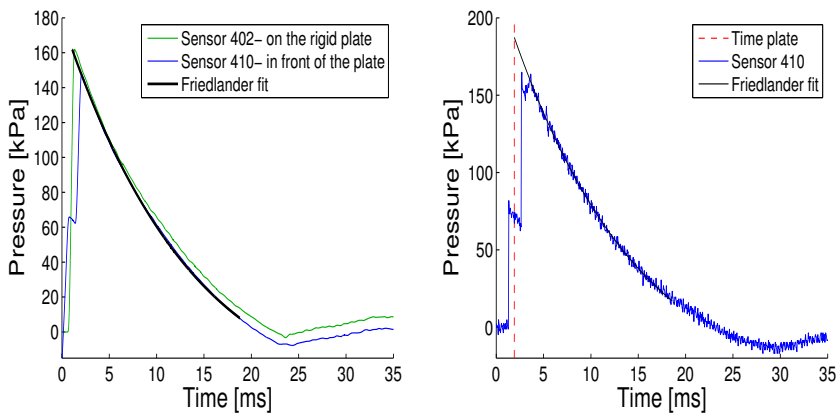
Since sensors 409 and 410 are located in front of the plate, there is no data of the exact pressure applied to the plate for the component tests. To be able to estimate the exact pressure, the time of contact between the plate and blast wave must be found. This is easily done by utilizing the information in Figure 5.12b. The time  $t_i$  is given as the time it takes for the shock wave to travel from sensor 409 to 410. Since the distance between the sensors is known, it is possible to calculate the corresponding velocity. By assuming  $v_i = v_{wall}$ , the travelling time between the plate and the wave can be calculated.

When the time  $t_{wall}$  is found, it is possible to use extrapolation to find the exact pressure at the plate. Extrapolation is conducted by using the modified Friedlander Equa-



tion (3.4) in Section 3.1.7. It is a common approximation when describing the pressure-time history for blast loading on a continuous format. In Equation (3.4), the ambient pressure  $P_0$  is set to zero and the incident pressure  $P_s^+$  is replaced by the reflected overpressure  $P_r$ .

The three unknown parameters in the Friedlander equation are the reflected overpressure  $P_r$ , the decay coefficient  $b$  and the positive duration  $t_+$ . In order to determine the value of these parameters, a curve fitting tool using the Levenberg-Marquardt algorithm in MATLAB is applied. To verify the use of extrapolation back in time, the Friedlander equation is used on the calibrated data where the pressure of the plate is already known. Figure 5.13a shows the smoothed pressure-time history of sensors 402 and 410. The first sensor is located directly on the rigid plate and the latter is placed in front of the plate. By extrapolating the curve obtained by sensor 410, it is shown that the Friedlander fit intersects with the maximum peak reflected pressure of sensor 402. Consequently, the Friedlander Equation (3.4) can be used on the experimental data to estimate the peak reflected pressure on the plate, illustrated in Figure 5.13b.



(a) Verification of the Friedlander fit based on a calibration experiment. (b) Friedlander fit of the pressure curve of a shock tube experiment.

**Figure 5.13:** Extrapolation of the pressure.

The natural period of vibration  $T_n$  can be determined using an approximate method with reasonable accuracy [77]. This method requires that both the structure and the loading are idealized to some extent. In this calculation, the structure is simplified as a single degree of freedom system. In addition, the elastic transformation factors for a two-way slab with four fixed sides and the uniform load are applied. The elastic factors are chosen since the expressions of the loading domains in Equation (5.2) are based on elastic assumptions. The following equations are used when calculating the natural periods,

$$\omega = \sqrt{\frac{k_e}{M_e}} = \sqrt{\frac{K_L k}{K_M M_t}} = \sqrt{\frac{k}{K_{LM} M_t}} \quad \text{and} \quad T = \frac{2\pi}{\omega} \quad (5.1)$$

where  $K_L$ ,  $K_M$  and  $K_{LM}$  are load-, mass- and load-mass factors respectively. Different values of these parameters are tabulated in the literature [77]. The spring constant is expressed as  $k = 810EI_a/a^2$  and the mass is given by  $M_t = \rho a^2 t$  where  $a$  is equivalent to the short edge of the plate (0.3m). The natural periods are given in Table 5.6.

**Table 5.6:** Natural periods of vibration for the plates.

Material		Elastic natural period, $T_n$ [ms]
Steel	0.8mm	13.2
	2.0mm	5.3
Aluminium	0.8mm	13.4
	2.0 mm	5.4

### 5.3.3 Experimental Results

Table 5.7 gives the loading parameters and the maximum out-of-plane displacement of the centre point  $u_{max}$ . The values are obtained from for the sensor closest to the plate, sensor 410. It should be noted that the blast wave parameters are limited to those related to the positive phase.

During the experiment of A0.8 – 10, the part of the plate subjected to the shock wave was completely torn out of the clamping frame. As will be illustrated later, the pressure-time history will deviate from the other experiments. Consequently, a Friedlander fit is not performed for this experiment and the decay coefficient is therefore not found. Since the plate fractures, the maximum displacement is not attainable. The maximum peak reflected pressure, the positive duration and impulse are obtained directly from the pressure-time history curve.

**Table 5.7:** Experimental results from the component tests.

Test	$P_{r,max}$ [kPa]	$t_+$ [ms]	$b$ [-]	$I_+$ [kPa × ms]	$t_+/T_n$ [-]	$u_{max}$ [mm]
S0.8-15	348.3	22.9	1.3	2735.9	1.7	18.4
S0.8-25	468.3	26.3	1.6	3993.6	2.0	22.1
S0.8-35	612.3	34.3	2.4	5370.2	2.6	26.8
A0.8-5	161.5	16.4	0.8	1081.3	1.2	23.8
A0.8-7.5	187.3	18.6	0.8	1413.6	1.4	27.6
A0.8-10	249.2	37.0	–	914.6	2.8	–
A2.0-15	345.4	24.6	1.2	3063.3	4.6	23.6
A2.0-25	460.6	28.6	1.7	4046.9	5.3	30.4
A2.0-35	640.4	39.5	2.2	6622.2	7.3	37.3

The characteristics of the loadings applied to the plates depend on the positive duration  $t_+$  and the natural period of vibration  $T_n$ . The following loading domains are defined [32],

$$\begin{aligned}
 \frac{t_+}{T_n} < 0.064 & \quad (\text{Impulsive domain}) \\
 0.064 < \frac{t_+}{T_n} < 6.4 & \quad (\text{Dynamic domain}) \\
 6.4 < \frac{t_+}{T_n} & \quad (\text{Quasi-static domain})
 \end{aligned} \tag{5.2}$$

By evaluating Table 5.7 and the different loading domains, the loadings applied to the plate are classified. While the loading in experiment A2.0 – 35 is characterized as quasi-static, the other loadings belong to the dynamic domain. For a quasi-static loading, the deformation is mainly related to the peak load and it is not dependent on the duration of the loading. For the loading in the dynamic domain, the deformation is determined by the entire load history. Consequently, the shape of the pressure-time curve is important for the response of the plate [78].

In Figure 5.14, the maximum mid-point deflection is plotted against the maximum peak reflected pressure. Since there is only two data points for the 0.8 mm aluminium plates, it is challenging to state a relation that accounts for the loadings in general. All the data points for the 0.8 mm steel specimens shows a nearly perfect correlation with the linear fit. The results of the 2.0 mm aluminium plates are also in accordance with the linear line. However, more data points are needed in order to state a representative relation.

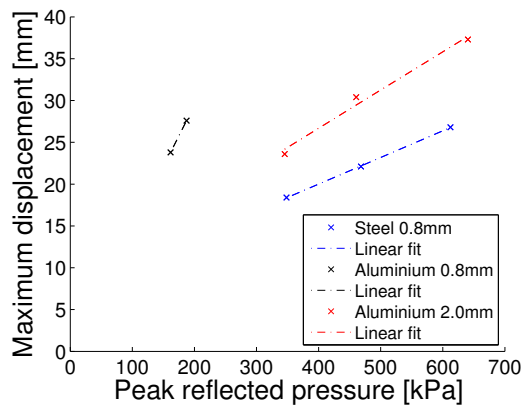
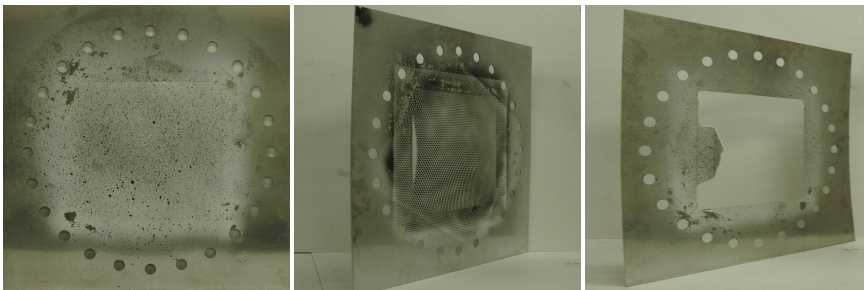


*Figure 5.14: Peak reflected pressure and maximum displacement.*

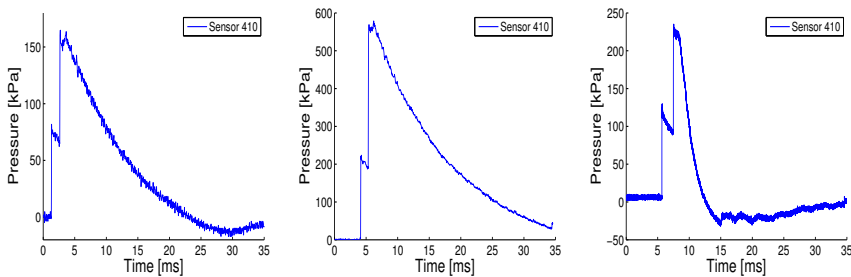
## Response of the Plates

Most of the shock tube experiments expose the same response patterns. However, two of the aluminium plates experience failure. Figure 5.15 depicts three plates that exhibit difference responses. Figure 5.15a displays test A0.8–7.5 that experience a typical deformation. The A2.0 – 35 experiment displays a tear along one of the boundaries, shown in Figure 5.15b. Figure 5.15c illustrates how the blast subjected plate in experiment A0.8 – 10 is completely torn off from the rest of the plate. The pressure-time history for the three corresponding responses are shown in Figure 5.16. While the pressure-time histories for A0.8 – 7.5 and A2.0 – 35 display the same behaviour, the response is different for the A0.8 – 10 experiment. When the plate fractures, the pressure propagates into the dump tank. This is illustrated by a rapid decrease of the pressure-time history in Figure 5.16c.



(a) Typical deformation. (b) Tearing along boundary. (c) Complete tearing.

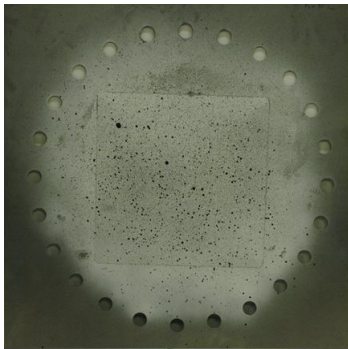
**Figure 5.15:** Three different plate responses.



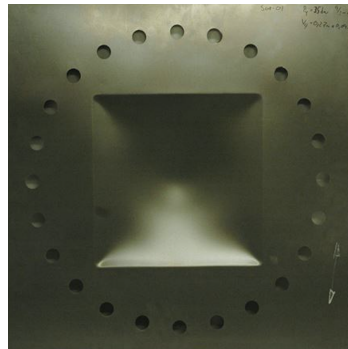
(a) Typical deformation. (b) Tearing along boundary. (c) Complete tearing.

**Figure 5.16:** Pressure-time histories of different component responses.

Figures 5.17, 5.18 and 5.19 display selected plates exposed to blast loading. A typical response for each of the materials is illustrated. For the aluminium experiment, images of both thicknesses are shown. As seen, the steel plate exhibit prominent yield lines. The yield lines accumulate from each corner and unite at the centre point of the plate. The aluminium plates display a more arced response. This may be related to the stiffness of the two materials. Steel has a elasticity modulus almost three times greater than aluminium, and this may result in more visible yield lines of the steel plates compared with the aluminium plates. The material characteristics of the two materials also lead to greater deflections of an aluminium plate when exposed to the same loading as a steel plate. The remaining plates used in the shock tube experiments are depicted in Section C.3.2 in Appendix C.

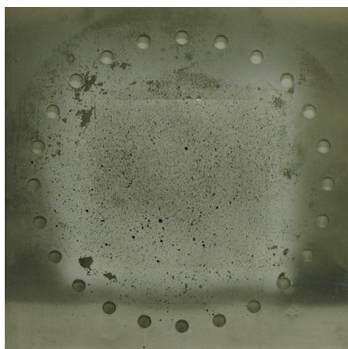


(a) The front of the plate.

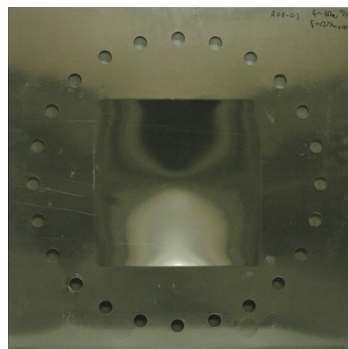


(b) The backside of the plate.

**Figure 5.17:** Plate S0.8-35 after deformation.

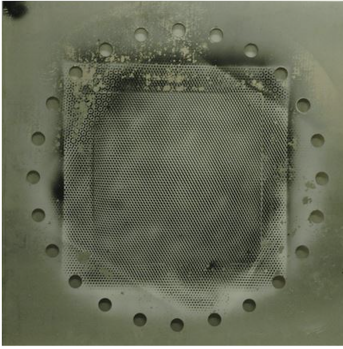


(a) The front of the plate.

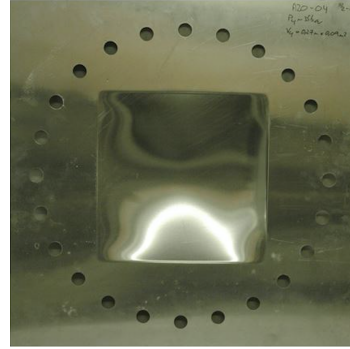


(b) The backside of the plate.

**Figure 5.18:** Plate A0.8-7.5 after deformation.



(a) The front of the plate.



(b) The backside of the plate.

**Figure 5.19:** Plate A2.0-35 after deformation.

In order to fully illustrate the response process of the plates during the shock tube experiment, a sequence of images from the high-speed cameras are shown. Figure 5.20 shows the response process of A0.8 – 7.5. This plate displays a typical deformation pattern and the maximum mid-point deflection is 27.6mm. Figure 5.21 illustrates the complete tearing of the plate in experiment A0.8 – 10. The tearing is initiated at one of the boundaries, which implies a shear fracture of the plate. In the last frames it is seen how the plate fractures around the boundaries and finally is completely torn off from the clamping frame. In both of the sequences it is possible to study the propagation of the yield lines as the response process evolves.

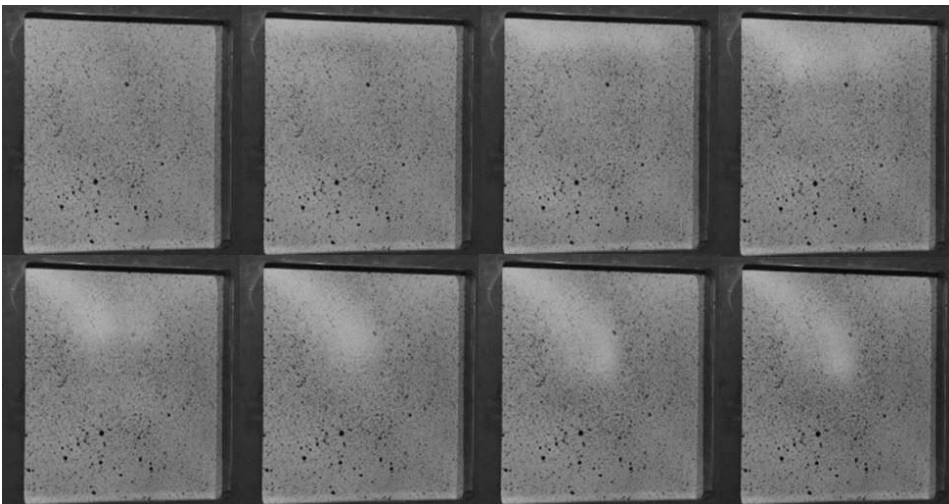


**Figure 5.20:** Typical deformation of a plate.

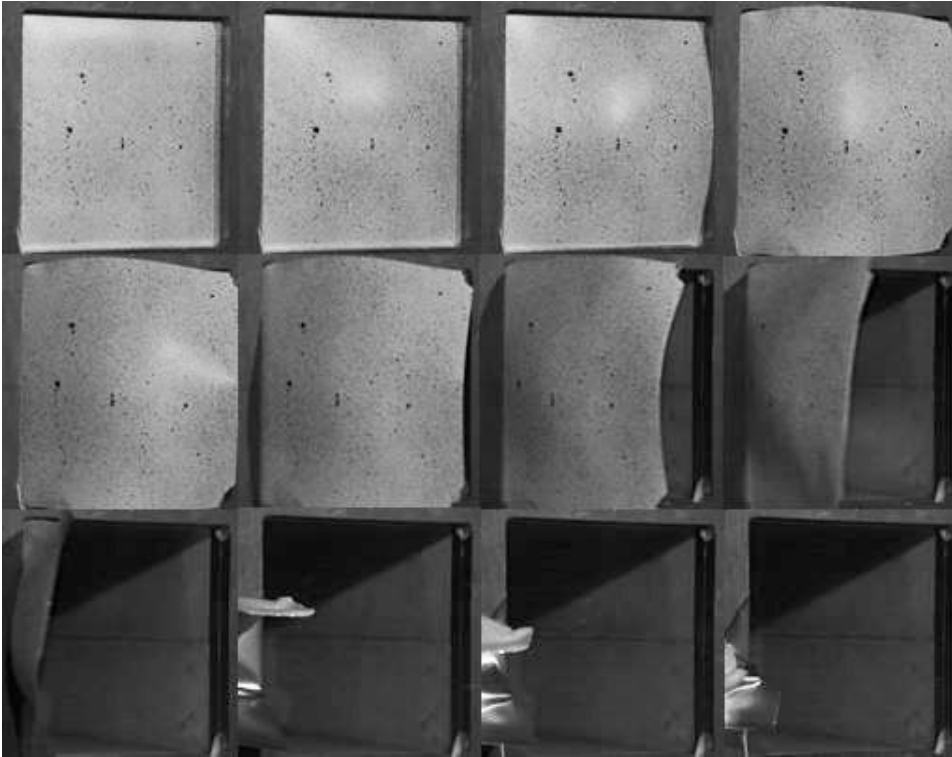


*Figure 5.21: Plate completely torn out of the clamping frame.*



### 3D-DIC post-processing and synchronized pressure

Based on the images from the high-speed cameras, a program called eCorr [79] is used to find the deformation fields of the plates. A 3D-DIC processing of the plates are conducted and it is therefore possible to obtain different plots of the plate's response. The three different plots illustrates,

- a) The deflection in 3D.
- b) The pressure and displacement distribution.
- c) The displacement over the cross-section.

The 3D-plots provides a good understanding of the displacement field of the plate and the second plot combines the pressure and displacement history of the plate. The third graph illustrates the maximum mid-point deflection over the cross-section of the plate.

Figures 5.22, 5.23 and 5.24 illustrates the response process of the S0.8 – 15 experiment. Three different time steps are chosen. Initially, at  $t = 0.833$  ms, the plate has just started to deform. The last frame, at  $t = 1.417$  ms, displays the plate after reaching its maximum deflection. In the first illustration, the plate is slightly curved between the yield lines. Ideally, this line should be straight. The curvature of the line is caused by an initially curved plate in the 3D-DIC calibration and not by the physics of the plate. The plots illustrating the pressure and displacement history, includes two red marks. They represent the respective time at the chosen frame.

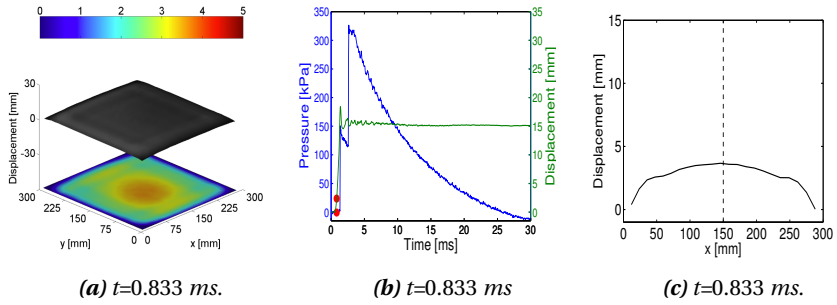


Figure 5.22: Response process of experiment S0.8 – 15.

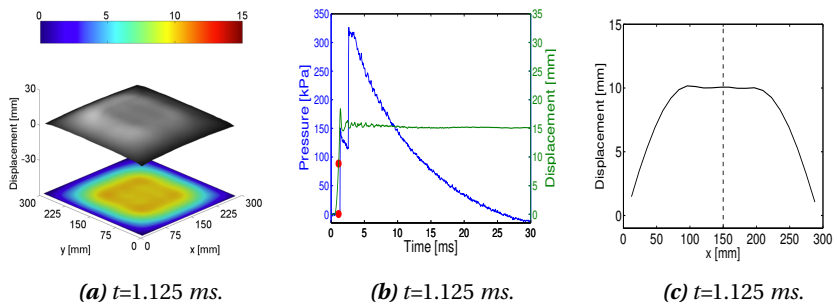


Figure 5.23: Response process of experiment S0.8 – 15.

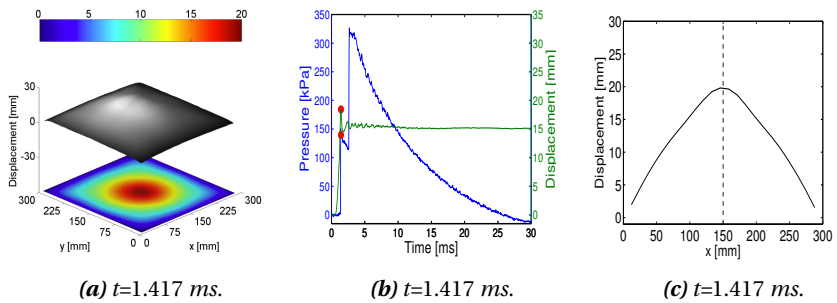
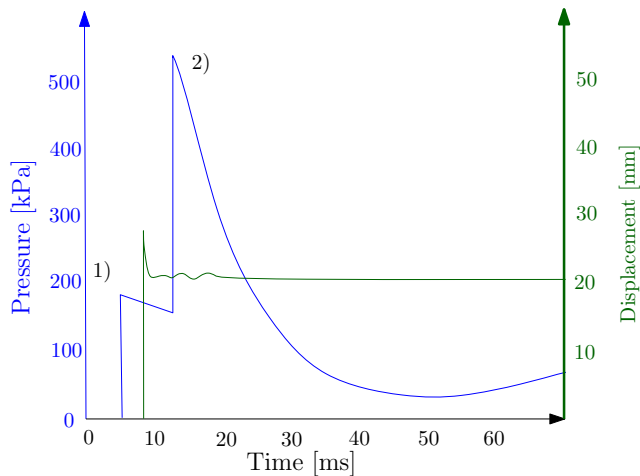


Figure 5.24: Response process of experiment S0.8 – 15.

Further, the responses of the component experiments are plotted when the plate reaches its maximum deflection. The plots are shown on the next pages. When evaluating the plots, it is clear that some of the results are non-physical. This is especially illustrated in Figures 5.28a, 5.28c and 5.32a. These results are a consequence of noise and highlights in the 3D-DIC. When studying the displacement-time history, it is observed that oscillations only occur for a few ms. After the shock wave impacts the plate, the pressure is reflected. As illustrated in Figure 3.8 in Chapter 3, a pressure  $P_5$  exist after the reflection of the shock. This pressure may behave as a constant force, preventing the oscillations of the plate to occur.

Figure 5.25 displays an illustration of an ideal pressure and displacement plot. As shown, the deformation of the plate starts between points 1) and 2). In most of the plots from the component experiments, the beginning of the displacement curves are located before point 1) occurs. This is a result of an error in the synchronization between the recorded pressure and the high-speed cameras.



**Figure 5.25:** Illustration of an ideal pressure and displacement history plot.

Responses of the 0.8 mm Steel Plates

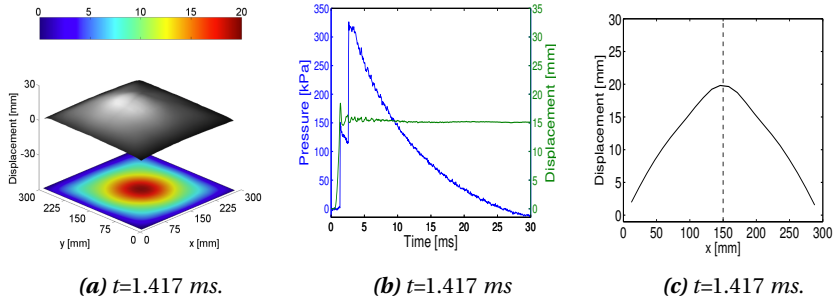


Figure 5.26: Response process of experiment S0.8 – 15.

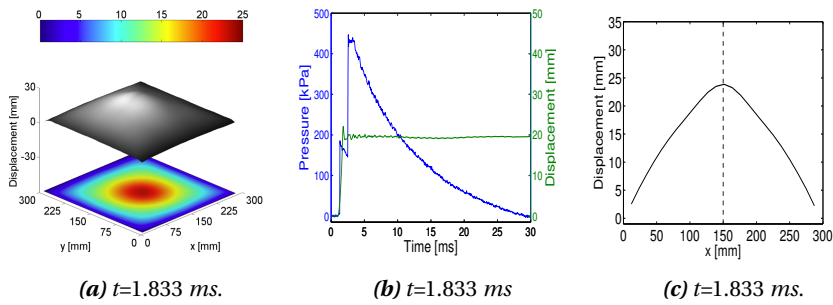


Figure 5.27: Response process of experiment S0.8 – 25.

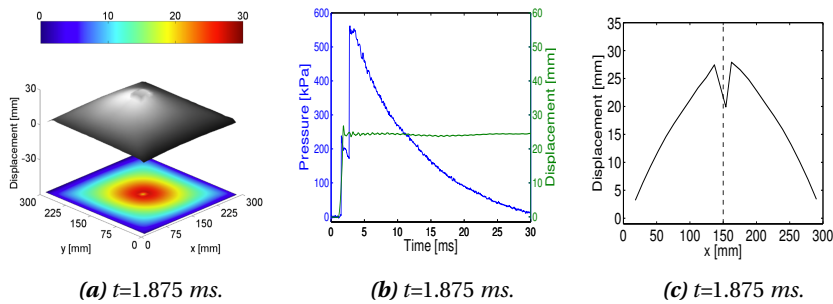
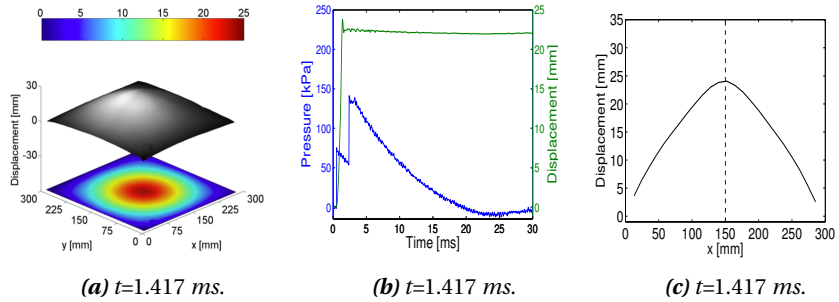
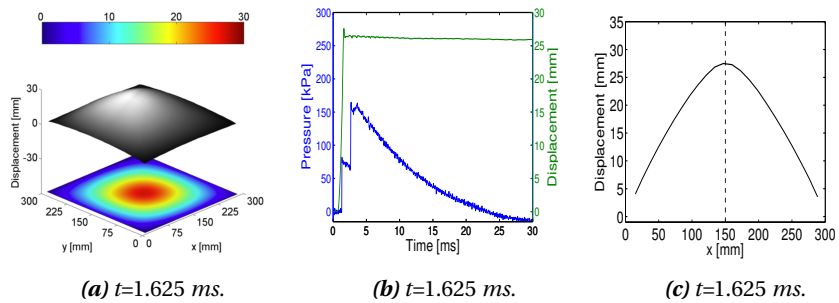


Figure 5.28: Response process of experiment S0.8 – 35.

**Responses of the 0.8 mm Aluminium Plates**



*Figure 5.29: Response process of experiment A0.8 – 5.*



*Figure 5.30: Response process of experiment A0.8 – 7.5.*

**Responses of the 2.0mm Aluminium Plates**

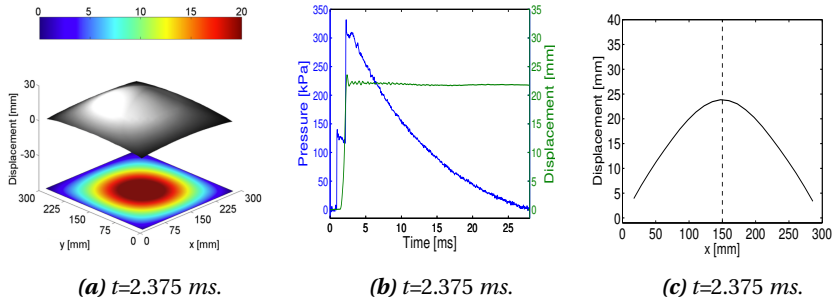


*Figure 5.31: Response process of experiment A2.0 – 15.*

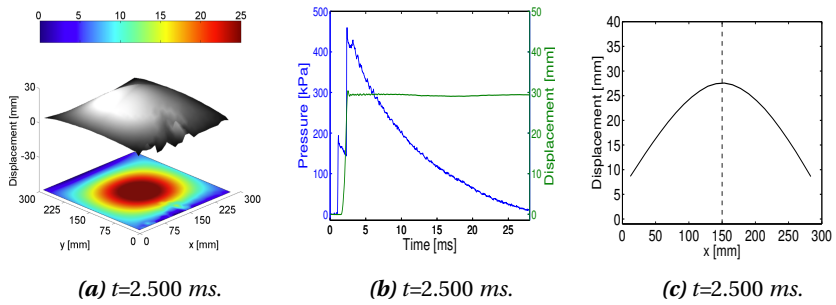


*Figure 5.32: Response process of experiment A2.0 – 25.*

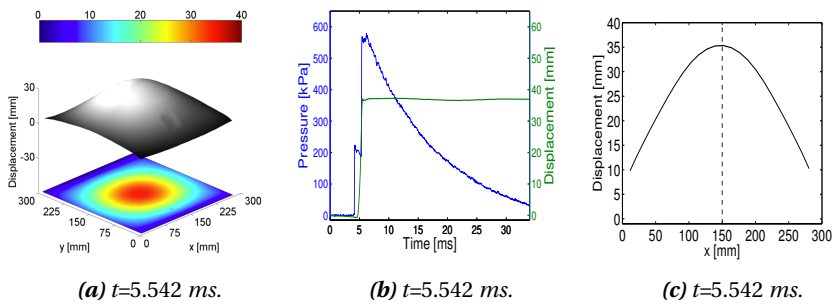


*Figure 5.33: Response process of experiment A2.0 – 35.*

## 5.4 Metallurgic Study of the Blast Subjected Plates

It is desirable to examine the cross-section of the plates after being exposed to the blast loading. NTNU Metallurgy has performed a detailed study of the plates. The area of interest is the crossing between the blast subjected domain and the clamping frame, illustrated in Figure 5.34. While the top surface of the cross-section corresponds to the front of the plate, the bottom surface is equivalent to the back side of the plate. Consequently, it is the bottom surface that is subjected to the blast loading.

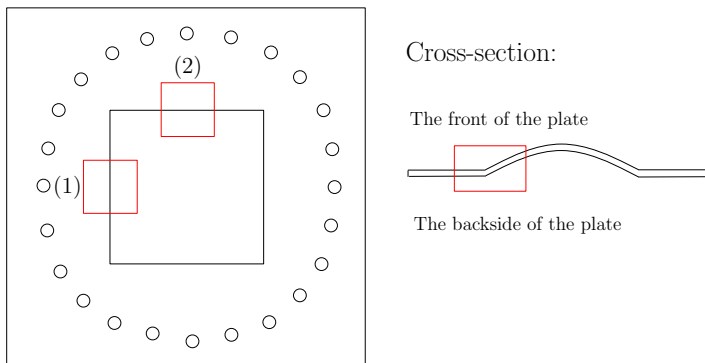


**Figure 5.34:** The area of interest of the metallurgic study.

NTNU Metallurgy has processed the plates and the results are shown in Figures 5.35, 5.36 and 5.37. The study has been performed on the plate that displayed a typical deformation (A0.8 – 7.5), the plate that fractured along one of the sides (A2.0 – 35) and the plate that was completely torn out of the clamping frame (A0.8 – 10).

The thickness displayed in Figure 5.35a are in good agreement with the nominal thickness of the plate. Figure 5.35c and 5.35d shows the initiation of necking and the reduction in cross-section close to the neck.

Figure 5.36a indicates an accurate thickness of the 2.0mm plate. As seen in Figures 5.36b, 5.36c and 5.36d, the clamping frame clearly affects the plate. By studying the left side of the neck, it is seen how a sharp edge is formed when the blast wave encounters the plate. The figures also illustrate how localized the response is.

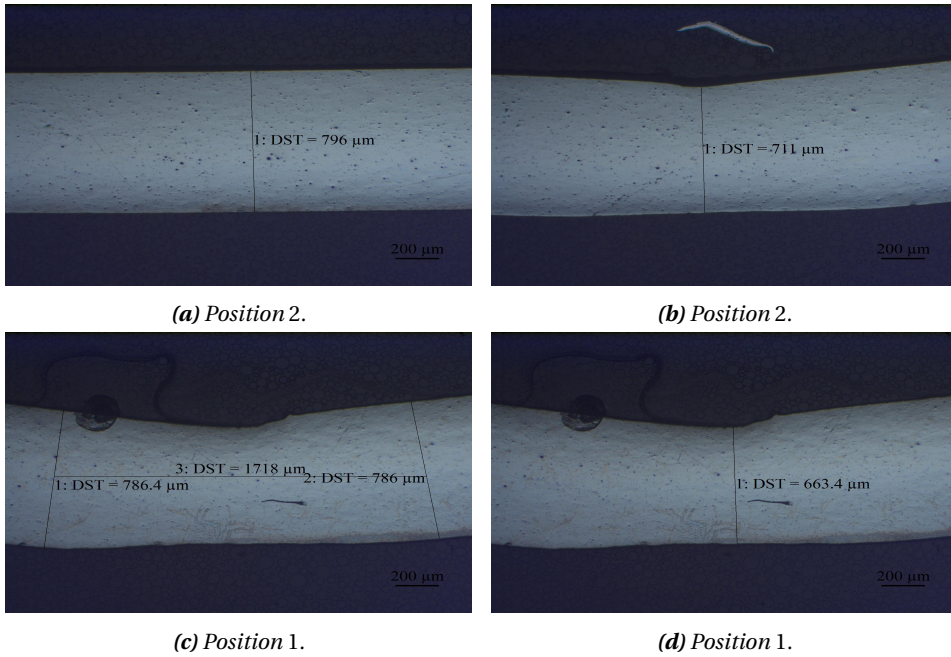


**Figure 5.35:** Metallurgic study of experiment A0.8 – 7.5.

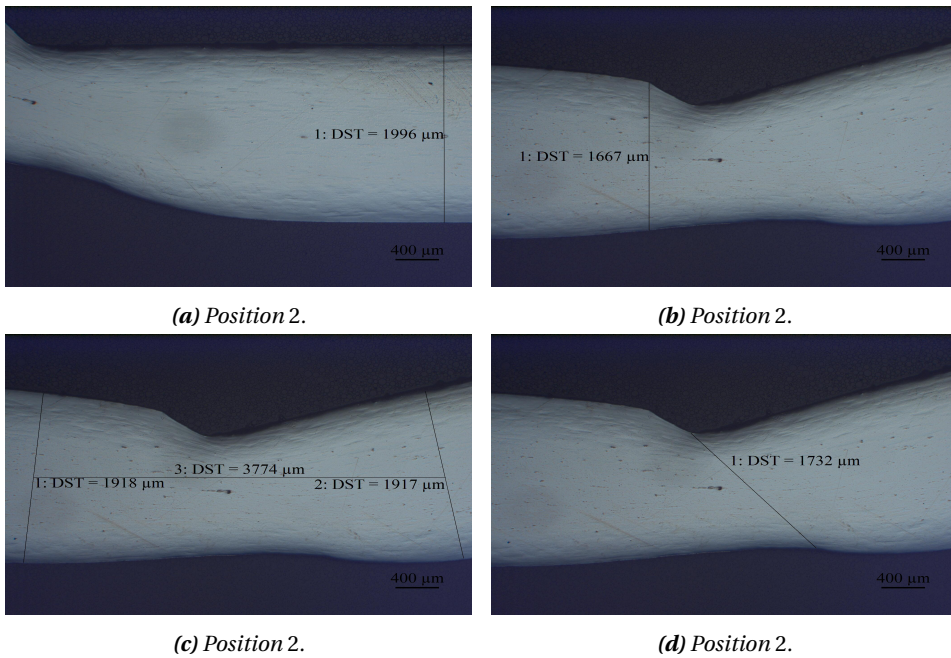


**Figure 5.36:** Metallurgic study of experiment A2.0 – 35.



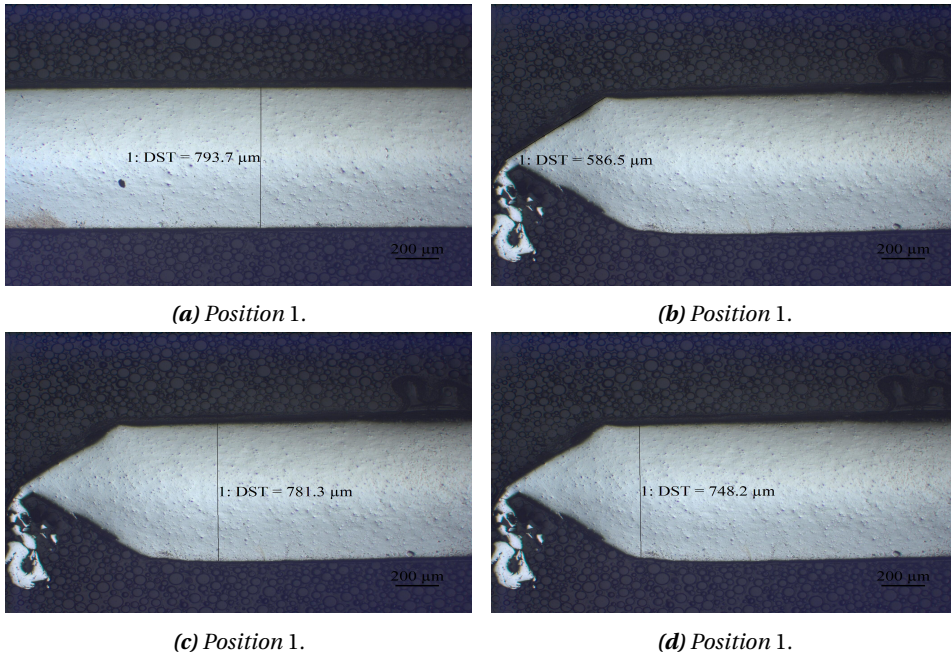


**Figure 5.37:** Metallurgic study of experiment A0.8 – 10.

Figure 5.37 illustrates the plate that were completely torn out of the clamping frame. The measured thickness of position 1 is accurate compared to the nominal thickness. The three next frames display the same image with different measurements. As observed, necking initially occurs and thereby it results in a distinct shear fracture.

The results from the metallurgic study, display necking for the different plates. Since the forming limit diagram in Section 3.4.1 is based on the same mechanism, this method should provide good results of the capacity of the plates.



## Chapter 6

# Analytical Calculations

There are several possible procedures when solving a plate problem. By applying an empirical model, the expected mid-point deflection of the plate can be calculated. It is important to understand that this approach does not obey physical laws as it only provides a mathematical relation of previous experiments. Hence, an empirical model is only applicable for experiments that satisfy the same requirements, e.g. loading and boundary conditions. In order to perform calculations that apply for plates in general, the yield line theory is introduced. By identifying a yield pattern of the plate, the collapse load can be determined. Finally, an introduction of the pressure-impulse diagram is given. By establishing this diagram, it is possible to evaluate if a certain loading will lead to structural damage.

### 6.1 Empirical Model by Nurick and Martin

Nurick and Martin [8] [80] published a two part review of the theoretical considerations and experimental work on the deformation of thin plates subjected to impulsive loading . Even though the loadings in the blast experiments are characterized as dynamic, it is interesting to see if the empirical model by Nurick and Martin is able to give a good approximation of the mid-point deflection. Before conducting any calculations, an in-

roduction of the empirical model is necessary.

In order to compare experimental results conducted by different researches using various plate dimensions and plate materials, a dimensionless damage number is defined as,

$$\alpha = \frac{\rho v^2}{\sigma_d} \quad (6.1)$$

where  $\rho$  is the material density,  $v$  is the impact velocity and  $\sigma_d$  is the damage stress. The damage number is used as a guide when evaluating the behaviour of metals exposed to impact loading. It is a simplified method that does not consider boundary conditions, structural geometry or the method of impact. By defining the damage number as a function of the impulse, it can be written as,

$$\alpha_0 = \frac{I^2}{A_0^2 t^2 \rho \sigma_0} = \frac{I_0^2}{t^2 \rho \sigma_d} \quad (6.2)$$

where  $I$  is the total impulse,  $A_0$  is the area of the plate exposed to the impulse,  $I_0$  is the impulse per area and  $t$  is the plate thickness.

A geometry number for quadrangular plates is introduced,

$$\beta = \frac{L}{B} \quad (6.3)$$

where  $L$  and  $B$  are the length and width of the plate. This parameter together with the damage number are used when establishing an expression for the geometrical damage number,

$$\Psi = \left[ \beta \alpha_0 \left( \frac{A_0}{A} \right)^2 \right]^{\frac{1}{2}} \quad (6.4)$$

where  $A$  is the area of the plate.

The aspect ratio  $\lambda$  defines the relationship between the distance from the plate centre to the nearest boundary and the plate thickness  $t$ . For quadrangular plates the ratio is given as,

$$\lambda = \frac{B}{2t} \quad (6.5)$$

By combining Equations (6.4) and (6.5), an expression for a modified damage number, that includes dimensions and loadings, is defined,

$$\phi = \Psi \lambda \quad (6.6)$$

For quadrangular plates Equation (6.6) becomes,

$$\phi_q = \frac{I}{2t^2(BL\rho\sigma_0)^{\frac{1}{2}}} \quad (6.7)$$

In their review, Nurick and Martin simplified the value of the damage stress by setting it equal to the value of the static yield stress  $\sigma_0$ . This simplification is also made when performing the calculations of the steel and aluminium plates.

By performing a least square analysis of previous experimental results, an empiric relation between the mid-point deflection and the thickness of quadrangular plates were obtained,

$$\left(\frac{u}{t}\right) = 0.480\phi_q + 0.277 \quad (6.8)$$

In order to calculate the expected mid-point deflection, several parameters need to be known. While the different measurements and densities are easily obtained, the yield stress and impulse are found from the experimental research. The yield stress is obtained during the tensile testing of the materials and the positive impulse is given from the shock tube experiments. The impulses are given in the unit  $Ns$  which implies that they have been multiplied with the area of impact. The different parameters along with

the expected mid-point deflections are displayed in Table 6.1.

**Table 6.1:** *Expected mid-point deflections*

Test	$\sigma_0$ [MPa]	$I_+$ [Ns]	$\frac{u}{t}$ [-]	$u_{max}$ [mm]
S0.8-15	318.7	246.2	195.5	156.4
S0.8-25		359.4	285.2	228.2
S0.8-35		483.3	383.5	306.8
A0.8-15	97.1	97.3	237.4	189.9
A0.8-7.5		127.2	310.2	248.2
A2.0-15	86.3	275.7	114.3	228.6
A2.0-25		364.2	150.9	301.8
A2.0-35		596.0	246.8	493.5

When evaluating the results, the expected deflections are unrealistic, exposing several mid-point deflections larger than the actual length and width of the plate. The empirical model by Nurick and Martin is based on loadings in the impulsive domain. In the component experiments, the loading is characterized as dynamic. Since the impulse and dynamic loading are dependent on different characteristics of the pressure-time history curve, it is inadequate to use a model based on the wrong loading domain. Consequently, the empirical model by Nurick and Martin is not suitable when obtaining the mid-point deflection of the plates in this thesis.

## 6.2 Empirical Model for the Shock Tube Experiments

Since the empirical model by Nurick and Martin was not able to give a good approximation of the mid-point deflection of the plates, it is decided to establish an empirical model of the shock tube experiments. The empirical model is based on algebraic equations in correlation with experimental data. An easy way to establish an empirical relation is through a dimensional analysis based on the Buckingham Pi theorem [81]. The theorem states that if there exists a physical law that gives a relation among a certain number of physical quantities, then there is an equivalent law that can be expressed as a relation among certain dimensionless quantities. It is important to understand that the empirical relation is limited to the experimental conditions and the results can not be extrapolated [81]. The variables that are assumed to have the greatest impact on the deflection of the plate are displayed in Table 6.2.

**Table 6.2:** Selected input variables.

Variable	Symbol	Unit	Fundamental Dimension
Yield strength	$\sigma_0$	$N/m^2$	$F \cdot L^{-2}$
Thickness	$t$	m	L
Density	$\rho$	$kg/m^3$	$F \cdot T^2 \cdot L^{-4}$
Pressure	$P$	$N/m^2$	$F \cdot L^{-2}$
mid-point deflection	$u$	m	L

Based on the input variables, an expression of the mid-point deflection is found,

$$u = u(\sigma_0, t, \rho, P) \tag{6.9}$$

Due to the Buckingham Pi theorem, the chosen variables can be arranged on a matrix form. By performing Gaussian elimination, the matrix problem is solved and the solutions are displayed in Equation (6.10).

$$\begin{array}{c|ccccc} & a_1 & a_2 & a_3 & a_4 & a_5 \\ & \sigma_0 & t & \rho & P & u \\ \hline F & +1 & 0 & +1 & +1 & 0 \\ L & -2 & +1 & -4 & -2 & +1 \\ T & 0 & 0 & +2 & 0 & 0 \end{array} \implies \begin{array}{c|ccccc} & a_1 & a_2 & a_3 & a_4 & a_5 \\ & \sigma_0 & t & \rho & P & u \\ \hline F & +1 & 0 & 0 & +1 & 0 \\ L & 0 & +1 & 0 & 0 & +1 \\ T & 0 & 0 & +1 & 0 & 0 \end{array}$$

$$a_1 = -a_4, \quad a_2 = -a_5, \quad a_3 = 0 \quad (6.10)$$

The dimensional analysis requires the equations to be dimensionally homogeneous. Equation (6.11) must therefore be satisfied,

$$\begin{aligned} F^0 \cdot L^0 \cdot T^0 &= \sigma_0^{a_1} \cdot t^{a_2} \cdot \rho^{a_3} \cdot P^{a_4} \cdot u^{a_5} \\ &= \sigma_0^{-a_4} \cdot t^{-a_5} \cdot \rho^0 \cdot P^{a_4} \cdot u^{a_5} \end{aligned} \quad (6.11)$$

The terms with the same exponent are collected and the expression is rearranged as,

$$F^0 \cdot L^0 \cdot T^0 = \left( \frac{P}{\sigma_0} \right)^{a_4} \left( \frac{u}{t} \right)^{a_5} \quad (6.12)$$

or

$$\frac{u}{t} = f\left( \frac{P}{\sigma_0} \right) \quad (6.13)$$

Figure 5.14 in Chapter 5 indicates a linear relationship between the mid-point deflection and pressure. This is expressed as,

$$\frac{u}{t} = K \left( \frac{P}{\sigma_0} \right) \quad (6.14)$$

where K is a model constant which can be determined from a curve fit [65] of Equation (6.14) to the experimental data from the shock tube.

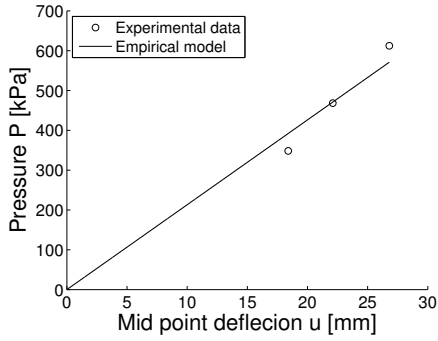
The final expression of the mid-point reflection reads,

$$u = K t \left( \frac{P}{\sigma_0} \right) \quad (6.15)$$

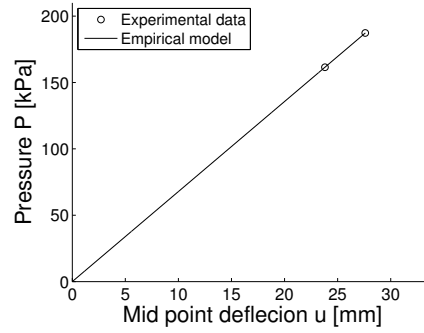
This is a very simple expression that only depends on a few variables. Since the empirical relation is linear, it may be sufficient to perform linear regression of the experimen-



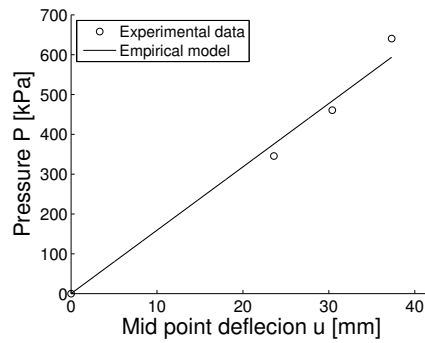
tal data. The empirical models obtained for the different plates are depicted in Figure 6.1. It should be noted that more experimental data are necessary to get a proper empirical model.



(a) The 0.8mm steel plates.



(b) The 0.8mm aluminium plates.



(c) The 2.0mm aluminium plates.

**Figure 6.1:** Empirical models for the different metal plates.

### 6.3 Yield Line Theory

Yield line theory is an ultimate load analysis. When a plate is loaded to its ultimate plastic capacity in bending, yield lines start to form in highly stressed areas. Subsequently, these yield lines develop into continuous plastic hinges forming a yield line pattern [82].

The collapse load may be found by applying the virtual work method. The fundamental principle of this approach states that the internal and external work must be equal. While the internal work corresponds to the work done in the rotating yield lines, the external work is equivalent to the work done by the external loads. This is mathematically expressed as,

$$W_e = W_i \quad (6.16)$$

where the external load is given as,

$$W_e = \begin{cases} \sum (q \times u)_{\text{for all regions}} & \text{for a point load} \\ \sum (q \times V)_{\text{for all regions}} & \text{for a uniformly distributed load} \end{cases} \quad (6.17)$$

and the internal load is expressed as,

$$W_i = \sum (m_p \times l \times \theta)_{\text{for all regions}} \quad (6.18)$$

where,

- $q$  is the load acting within a particular region of the plate
- $u$  is the vertical displacement of the load  $q$  on each region expressed as a fraction of unity
- $V$  is the volume that forms when the initial geometry of the plate deforms
- $m_p$  is the plastic moment capacity of the yield line
- $l$  is the length of the yield line or its projected length onto the axis of rotation for that region
- $\theta$  is the rotation of the region about its axis of rotation

In order to use the yield line approach, it is necessary to assume a collapse pattern of the plate. By evaluating the metal plates after the blast experiment, the yield pattern is similar to a square pyramid (Figure 6.2).

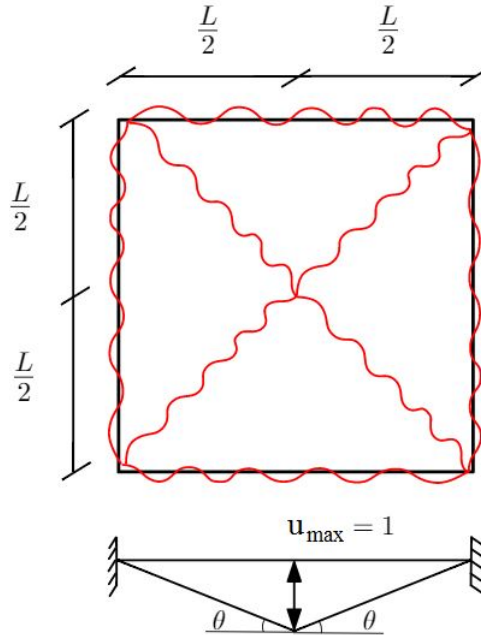


**Figure 6.2:** Yield lines of the metal plates.

During the experiments, the plates are subjected to a uniform pressure distribution. Hence, the second formula in Equation (6.17) is used. By studying the yield pattern in Figure 6.2, it is evident that the volume of the deformed plate corresponds to the volume of a pyramid. Consequently, the external work is given as,

$$W_e = q \times V = \frac{qL^2 u}{3} \quad (6.19)$$

By using trigonometry and assuming small deformations ( $\tan \theta \approx \theta$ ),  $\theta$  is obtained as  $\frac{u}{L/2} = \frac{2u}{L}$ . By summing the contributions from all the yield lines, the internal work is determined,

$$W_i = 16m_p u \quad (6.20)$$

As a result, the collapse load in bending becomes,

$$q = \frac{48m_p}{L^2} \quad (6.21)$$

where  $L = 0.3\text{m}$  and the plastic moment resistance is equal to  $\frac{\sigma_0 l^2}{4}$ . The plastic moment resistance is based on a static uniform loading. Since the loading applied to the plates is in the dynamic domain, a dynamic yield stress is also introduced. It can be expressed as Equation (6.22), by neglecting the strain hardening and temperature softening from the Johnson-Cook Equation (3.37) in Section 3.6.

$$\sigma_{dy} = \sigma_0 \left(1 + \frac{\dot{p}}{\dot{p}_0}\right)^C \quad (6.22)$$

As a simplification,  $C$  is set to 0.005 and  $\dot{p}$  is assumed to be  $100\text{s}^{-1}$  for both the materials. The plastic equivalent strain rate  $\dot{p}_0$  is equal to  $1\text{e}^{-4}\text{s}^{-1}$  and  $5\text{e}^{-4}\text{s}^{-1}$  for steel and aluminium, respectively.

The expected collapse loads in bending for the different plates are viewed in Table 6.3. Here,  $q_s$  and  $q_d$  represent the static and dynamic collapse load in bending of the plates. As the table displays, there is no significant difference of the two collapse loads.

**Table 6.3:** Expected failure loads in bending.

Plate		$m_{p,s}$ [kNm/m]	$q_s$ [kN/m <sup>2</sup> ]	$m_{p,d}$ [kNm/m]	$q_d$ [kN/m <sup>2</sup> ]
Steel	0.8mm	0.051	27.2	0.055	29.1
Aluminium	0.8mm	0.016	8.3	0.017	8.8
	2.0mm	0.086	46.0	0.092	48.9

By comparing the expected collapse loads in bending with the experimental data from Section 5.7, it is evident that the yield line approach severely underestimates the collapse loads of these experiments. This is counter-intuitive since the yield line approach should give an upper bound solution, making the collapse load either correct or too high [82].

There are several reasons why this approach should not be applied when dealing with blast experiments in this thesis. The yield line theory is a simplified method that is based on a perfect-plastic material, neglecting hardening of the materials. The presented approach is also based on small deformations, only including bending of the plate and ignoring membrane forces.

For plates undergoing finite deflections, membrane forces develop and they result in an increase of the load-carrying capacity [83]. In plates subjected to blast loading, membrane forces can be significant. It is therefore desirable to include these forces when finding the expected collapse load.

Amdahl [83] has developed an expression for the collapse load that includes both bending and membrane forces. The derived relationship is shown in Equation (6.23). The reader is referred to the literature [83] for a complete derivation of the expressions.

$$\frac{q}{q_0} = \begin{cases} 1 + z^2 \frac{\alpha + (3-2\alpha)^2}{9-3\alpha} & \text{if } z \leq 1 \\ 2z \left( 1 + \frac{\alpha(2-\alpha)}{3-\alpha} \left[ \frac{1}{3z^2} - 1 \right] \right) & \text{if } z \geq 1 \end{cases} \quad (6.23)$$

While the expression for  $\alpha$  is independent of the boundary conditions,  $z$  and  $q_0$  in Equation (6.24) is given for a clamped plate.

$$z = \frac{u}{t}, \quad q_0 = \frac{48m_p}{\alpha^2 L^2}, \quad \alpha = \frac{L}{B} \left( \sqrt{3 + \left( \frac{B}{L} \right)^2} - \frac{B}{L} \right) \quad (6.24)$$

where,

- L is the length of the plate
- B is the width of the plate
- u is the mid-point deflection of the plate
- t is the thickness of the plate

For a square plate  $\alpha$  is equal to one and  $q_0$  becomes equivalent to Equation (6.21). The collapse load in Equation (6.23) is then expressed as,

$$q = \begin{cases} q_0(1 + z^2 \frac{1}{3}) & \text{if } z \leq 1 \\ 2zq_0(1 + \frac{1}{2}[\frac{1}{z^2} - 1]) & \text{if } z \geq 1 \end{cases} \quad (6.25)$$

where  $q$  is a function of the mid-point deflection of the plate, the thickness of the plate and the collapse load in bending. The two latter variables are known and the collapse load  $q$  is plotted by choosing different values of the mid-point deflection. While the first expression in Equation (6.25) is used for values of  $u$  that lead to a  $z \leq 1$ , the second expression is used for values of  $u$  that result in  $z \geq 1$ . Figure 6.3 depicts the collapse load caused by bending only, and the collapse load due to the combination of bending and membrane forces for the different plates. The figure also displays the experimental data. The plots illustrate how the collapse-load capacity increases as membrane forces develop. By introducing membrane forces, the calculated collapse loads give a better approximation of the experimental data. However, by including membrane forces the expected mid-point deflections are overestimated. The conservative results can be explained by Amdahl's use of a static load.

In Section 5.3.3 in Chapter 5, the loading in experiment A2.0 – 35 is characterized as quasi-static. The experimental data from this test are therefore expected to correlate better with the results obtained from Amdahl's approach. By evaluating Figure 6.3c, it is seen that there is no significant difference between this test compared with the experiments with a loading in the dynamic domain.

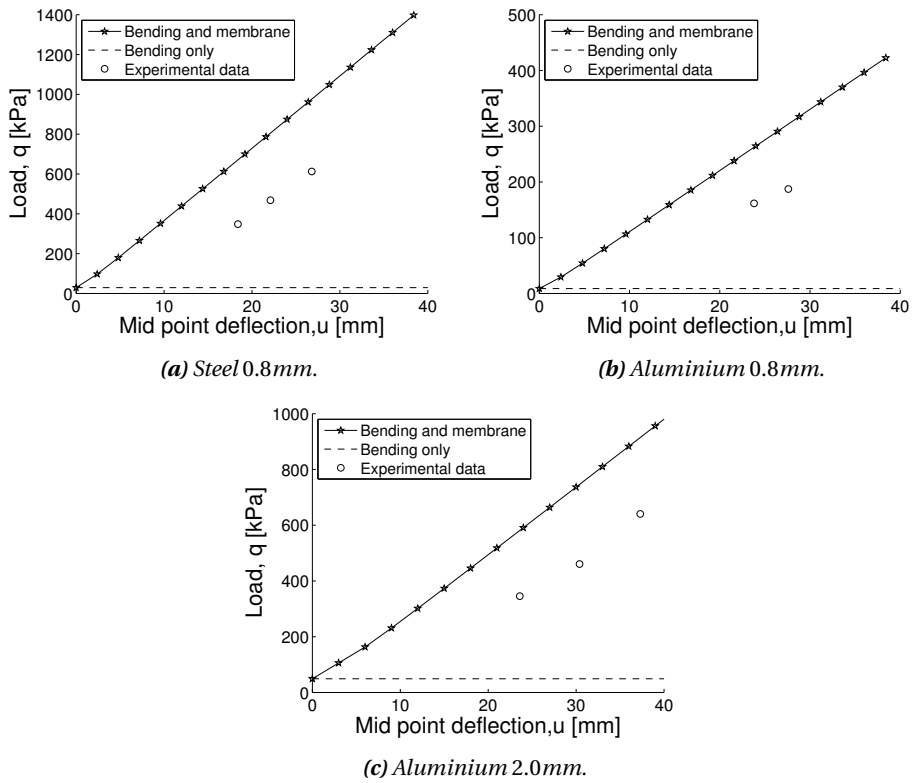


**Figure 6.3:** Failure loads  $w/$  and  $w/o$  membrane forces.

## 6.4 Pressure-Impulse Diagrams

A pressure-impulse (P-I) diagram is used when evaluating if a loading leads to structural damage [78]. In order to explain how P-I diagrams are established, it is necessary to explain the conditions of the different loading domains illustrated in Figure 6.4.

Quasi-static loading occurs for large values of  $\omega T$ , where  $\omega$  represents the frequency and  $T$  is the period of the plates. This means that only a small part of the loading dissipates before maximum deformation is reached. In the quasi-static domain, the deformation is related to the peak load  $P$  and the structural stiffness  $k$ . Hence, the response does not depend on the duration of the period  $T$  and the mass of the structure  $m$ .

$$\omega T_0 > 40 \implies u_{max} \approx \frac{2P_0}{k} \quad (\text{Quasi-static loading}) \quad (6.26)$$

Impulsive loadings are defined for small values of  $\omega T$ . In this domain, the structure is subjected to a loading that is removed before the structure has undergone significant deformation. In the impulsive domain, the deformation depends on the area under the load-time history curve. Consequently, different combinations of peak loads and durations that lead to the same impulse, will result in the same maximum deformation.

$$\omega T_0 < 0.4 \implies u_{max} \approx \frac{I_0}{\sqrt{km}} \quad (\text{Impulsive loading}) \quad (6.27)$$

The domain that exists for intermediate values of  $\omega T$  is called the dynamic domain. Here, the deformation depends on the entire load history. Both the pressure, the impulse, the structural stiffness and the mass, influence the response of the structure. As a result, it is difficult to apply idealizations and analytical solutions in this domain becomes complex.

$$0.4 < \omega T_0 < 40 \implies u_{max} = ? \quad (\text{Dynamic loading}) \quad (6.28)$$

Figure 6.4 can be replotted as the dimensionless pressure-impulse diagram in Figure 6.5. While  $P^0$  and  $I^0$  are the values for the real pressures and impulses,  $P^*$  and  $I^*$  are



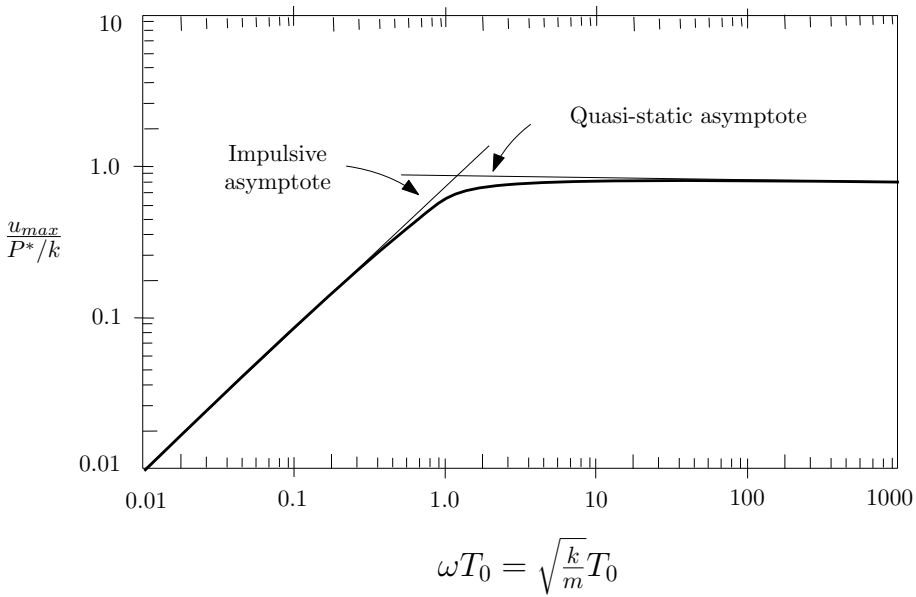


**Figure 6.4:** Impulsive and quasi-static asymptotes [78].

asymptotic values. If  $u_{max}$  is known, the asymptotic values for the quasi-static  $P^*$  and the impulsive  $I^*$  are given as  $P^* = \frac{k \times u_{max}}{2}$  and  $I^* = \sqrt{km} \times u_{max}$ . The rectangular hyperbola curve is called a isodamage curve. It is applied when characterizing the condition of a structure. If the applied pressure and impulse are located in the region above and to the right of the curve, the structure is damaged. If the pressure and impulse are positioned in any other region, the structure should be unharmed [78].

The P-I diagram can be established through numerical simulations. By conducting several analyses with different loadings, the quasi-static (force) asymptote can be determined. From each simulation, the loading  $P^*$  and maximum deflection are plotted in a diagram. By performing a curve adjustment of the points, an expression of  $P^*$  is found. The same procedure is executed when finding the impulsive asymptote. Here, analyses are run with different  $P^0$  and a time  $t_0$  that characterizes the loading as impulsive. By plotting  $I^*$  and  $u_{max}$ , and applying a curve fitting of the points, an expression for the impulse is defined. When both the asymptotes are determined, the isodamage curve can be found. For each of the analyses,  $\frac{P^0}{P^*}$  are plotted against  $\frac{I^0}{I^*}$ . Afterwards, a new curve fit is applied to the results from the analyses forming the isodamage curve [84].

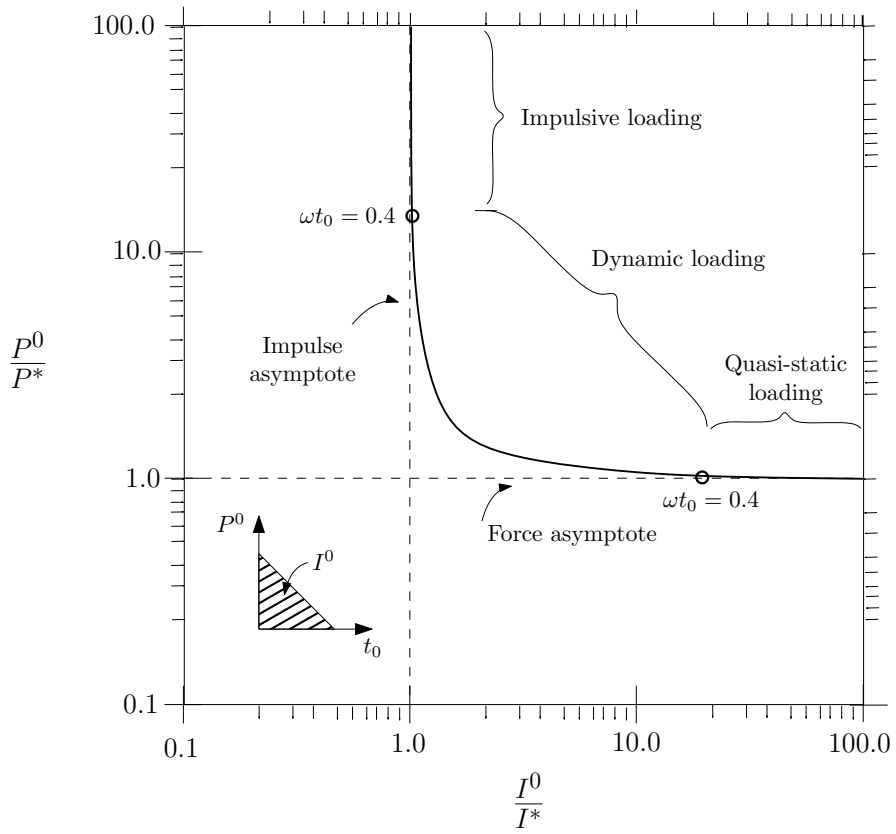


**Figure 6.5:** Pressure-impulse diagram [78].

## 6.5 Discussion of the Plate Problem

Empirical models are based on real component behaviour, and consequently it gives an approximate estimation of the structural response. It is an efficient and economic way to get an assessment of the mid-point deflection of the plate. However, there are restrictions regarding the use of the empirical models and they are only valid for experiments performed under the same conditions.

It is difficult to perform analytical calculations on a structure exposed to dynamic blast loading. The yield line theory is an efficient method, but it is based on several simplifications that are not suitable for the plate problem of this thesis. When only including bending, the yield line theory severely underestimates the collapse load. When introducing membrane forces the expected collapse loads increase and give a better representation of the plate problem.

Based on these observations, it is necessary to conduct numerical simulations in order to properly investigate the plate problem. This is supported by the theory behind the pressure-impulse diagram and Equation (6.4).



# Chapter 7

## Numerical Study

Since the analytical approaches do not provide sufficient solutions of the plate problem, numerical simulations are introduced. Numerical approaches are also favourable compared with real explosion experiments, due to economical aspects. The shock tube experiments are recreated using the finite element method (FEM) and the FE program Abaqus CAE. Further, the numerical model is validated by comparing the experimental data with the numerical results.

### 7.1 Abaqus/Explicit

An explosion is classified as a wave propagation problem. In addition, blast loading is a fast transient dynamic problem and the duration of the load applies in a few ms. This requires small time steps, and explicit time integration is therefore well suited. Abaqus uses the central difference method to solve the nonlinear dynamic equilibrium equations. When applying an explicit method to solve nonlinear problems, numerical instabilities may be difficult to detect. In order to discover these instabilities, an energy balance check is performed for all the simulations [67]. The reader is referred to Section A.1 in Appendix A for derivations and explanations of the explicit approach. To represent the geometry of the plate, the Lagrangian formulation described in Section A.2.2

in Appendix A is employed.

Three different computers are used when running the numerical analyses. For more time consuming analyses, Snurre, a cluster available at SIMLab with six processors is employed. The simulations run with this computer are marked with two stars (\*\*). The analyses run with an Intel Core i5 personal computer with two processors are marked with one star (\*). If not otherwise stated, an Intel Core i7 – 3517U CPU personal computer with two processors is applied.

### 7.1.1 Numerical Model

The numerical model is based on nominal geometry and material characteristics. Naturally, the thickness and applied load are adjusted for each of the experiments.

In Chapter 4, the Voce hardening rule were found to be the best fit for the behaviour of both steel and aluminium. Since the constitutive equation in Section 3.6 is defined with the power law, a modified equation is obtained. By replacing the first term in Equation (3.37) with the Voce rule, the constitutive equation reads,

$$\sigma_{eq}(\sigma) = (A + Bp^n) \left(1 + \dot{p}^*\right)^C \left[1 - (T^*)^m\right] = \left(A + \sum_{k=1}^2 Q_k \left(1 - e^{(-C_k p)}\right)\right) \left(1 + \dot{p}^*\right)^C \left[1 - (T^*)^m\right] \quad (7.1)$$

Since the Johnson-Cook model with the Voce hardening law is not implemented in Abaqus, a user-defined material model is applied [68]. The material card for the inverse steel and aluminium model can be viewed in Section D.1.2 in Appendix D. In case fracture of the plates occurs, the Cockcroft-Latham criterion is implemented. The parameters that are included in the material card are shown in Tables 7.1 and 4.8. While most of the parameters in Table 7.1 are found directly from the literature [72] [85], the strain rate hardening parameter and the equivalent plastic strain rate are modified to satisfy the material behaviour. Ideally, adiabatic conditions apply in shock tube experiments. This corresponds to  $\chi = 0.9$  in Equation (3.39). However, in the experiments conducted in this thesis, the effect of the temperature is undetermined. It is therefore decided to assume isotherm conditions ( $\chi = 0$ ) in the numerical model.

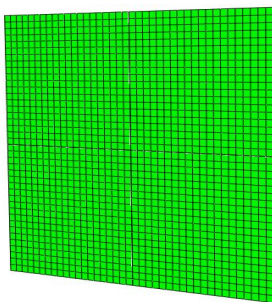
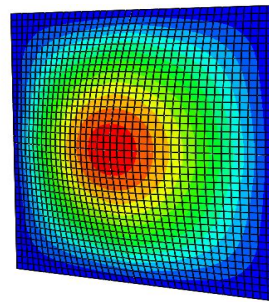
**Table 7.1:** Johnson-Cook material parameters and thermal properties [72] [85].

	$E$ [MPa]	$\nu$ [-]	$\rho$ [kg/m <sup>3</sup> ]	$C$ [-]	$m$ [-]	$\chi$ [-]	$T_r$ [K]	$T_m$ [K]	$C_p$ [J/kgK]	$\dot{\rho}_0$ [s <sup>-1</sup> ]
Docol 600DL	210 000	0.30	7800	0.005	1	0	293	1800	452	1e-4
EN AW-1050A-H14	71 000	0.33	2710	0.010	1	0	293	918	899	5e-4

When establishing a numerical model, a combination of efficiency and accuracy is evaluated. It is desirable to include all essential features and exclude superfluous details. Geometric irregularities, e.g. the thickness over the cross-section, may influence the behaviour of the plate by reducing the load-carrying capacity. However, such irregularities are neglected. Since the plates are slender, this simplification must be considered when evaluating the results.

When choosing boundary conditions, the original plates from the experiments have been studied. Since the plates experience minimal deformation in the bolt holes, it is decided to only model the blast subjected part of the plate. The computational time is reduced by modelling only a quarter of the plate and by applying two symmetry planes. To represent the clamped boundary conditions, the plate is fixed along the edges.

The pressure load in the numerical model is defined as the tabulated values of the extrapolated Friedlander curve. The Friedlander fit for each component experiment is shown in section C.3.1 in Appendix-C. Consequently, the applied pressure-time history in the numerical simulations are the same as in the shock tube experiments.

**(a)** Numerical model.**(b)** Deflection out of the plane.**Figure 7.1:** Illustration of the FE model in Abaqus CAE.

### 7.1.2 Sensitivity study

A sensitivity study is performed to make sure that the numerical model is not unnecessarily complex, but yet provides results that describe the problem with sufficient accuracy. With this in mind, solid and shell elements with different element sizes are evaluated.

There is no reason to believe that the outcome of the sensitivity study is different for the steel and aluminium plates. It is therefore sufficient to use one experiment when conducting this investigation. Experiment S0.8-15 is chosen as a point of reference when comparing the numerical results with the experimental data. In the shock tube experiment, this plate displayed a maximum and permanent deflection of 18.43mm and 15.41mm, respectively.

#### Element type

In order to choose a proper element type, it is important to understand how the structure is likely to respond and also how the different elements behave. Solid elements are preferable for bulky and complex 3D models. Since these elements can lead to large and expensive analyses, shell elements are introduced when a more economical solution is needed.

The solid elements used are C3D8R, a 8-node linear brick with reduced integration and hourglass control. The shell elements are defined as S4R. This is a general-purpose element that allows the element thickness to change during the analysis. Since the S4R accounts for finite membrane strains and arbitrarily large rotation, this element is suitable for large-strain analyses. By using a reduced integration rule with only one integration point, the CPU time decreases. A consequence of the reduced integration is hourglassing, hence Abaqus performs hourglass control of the S4R elements [86].

When applying solid elements, the length-thickness ratio should be close to three. In addition, to fully represent bending, the plate is defined with three elements through the thickness. The plate's thickness entails the use of very small elements in the solid model and to save computational time, the length of the elements is somewhat in-



creased. This result in each of the three elements through the thickness to have a size of  $1.00 \times 0.42 \times 0.26 \text{ mm}^3$ . To compare the solid and the shell model, the size of the shell elements are set to  $1.00 \times 1.00 \text{ mm}^2$ .

The results in Figure 7.2 and Table 7.2 imply that the shell model overestimates the response compared with the solid model. While the shell elements appear to give the best initial maximum response, the solid model gives a better fit of the permanent deflection. The most prominent difference in the two analyses, is the CPU time. While the solid model is relatively time consuming, the shell model is more effective. Since the numerical results are fairly similar, the computation cost is the decisive parameter. Consequently, solid elements are further neglected and a mesh sensitivity study is only performed of the shell elements.

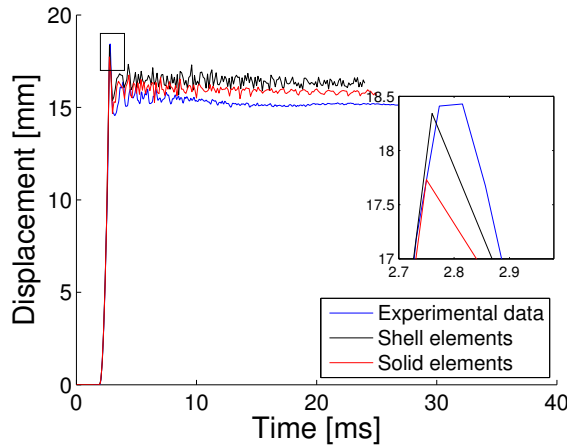


**Figure 7.2:** Displacement-time history of solid vs. shell elements.

**Table 7.2:** Maximum and permanent deflection for solid and shell elements.

Element type	Deflection [mm]		CPU time [h:min:s]
	$u_{max}$	$u_{perm.}$	
Solid	17.7	15.9	[11:28:19]**
Shell	18.3	16.4	[01:03:40]**

## Element Size

A rule of thumb states that when applying shell elements, the size of the elements should be between three and ten times the thickness. Hence, elements between three and eight mm are tested. To study if greater element sizes affect the maximum mid-point deflection, two additional analyses with an element size of ten and fifteen mm are performed. Since bending dominates the behaviour of the plate, the number of integration points through the thickness must be checked. The Simpson rule is applied when testing the number of integrations points of three, five and seven.

Table 7.3 and Figure 7.3 present the results from the mesh sensitivity study. The results show that while the maximum displacement  $u_{max}$  is underestimated, the permanent response  $u_{perm.}$  overestimates the deflection of the plate. The shape of the displacement-time history is fairly similar, but one feature is different. In the experimental data, the displacement is damped out over time, while in the simulations the vibration response presents no damping. This can be explained by the fact that no structural damping is embedded in the numerical model [72]. It is important to remember that from an engineer point of view, the maximum deflection is of main interest when designing a structure.

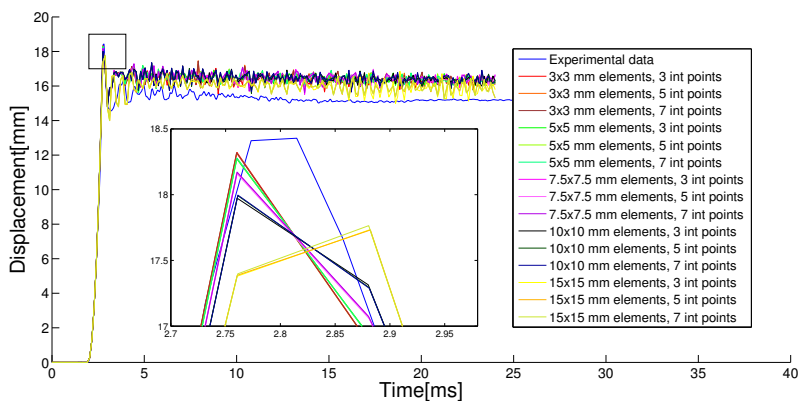


**Figure 7.3:** Displacement-time history for different element sizes.

**Table 7.3:** Different element sizes and the corresponding deflections.

Element size [mm]	Integration points through thickness	Deflection [mm]		CPU time [h:min:s]
		$u_{max}$	$u_{perm.}$	
3	3	18.32	16.37	[00:05:37]
	5	18.32	16.42	[00:08:08]
	7	18.32	16.39	[00:11:07]
5	3	18.27	16.42	[00:01:22]
	5	18.28	16.42	[00:01:51]
	7	18.28	16.41	[00:02:39]
7.5	3	18.17	16.44	[00:00:24]
	5	18.16	16.45	[00:00:36]
	7	18.17	16.45	[00:00:50]
10	3	17.97	16.44	[00:00:14]
	5	17.99	16.43	[00:00:19]
	7	17.80	16.45	[00:00:24]
15	3	17.73	15.97	[00:00:06]
	5	17.73	16.00	[00:00:08]
	7	17.76	16.01	[00:00:10]

### Results from the Sensitivity Study

By evaluating the results from the previous section, a choice can be made regarding the element size and the number of integration points of the numerical model. Both efficiency and accuracy of the analyses are considered. The element size of 3mm gives the best correlation with the maximum response. However, the variation of the maximum mid-point deflection for the three smallest elements sizes is insignificant. Consequently, the computational time is the decisive parameter regarding the choice of element size.

When evaluating the number of integration points through the thickness, it is evident that by increasing the number of integration points, the computational time increases. There is no significant change in the maximum mid-point deflection when the number of integration points are altered.

Based on these observations, it is decided to use a numerical model with an element size of 7.5 mm and with five integration points through the thickness. To verify that numerical instabilities are not present in the simulation, an energy balance check is performed. In a finite element model the sum of all energy components should be con-

stant. In addition, the artificial strain energy which includes energy stored in hourglass resistance and transverse shear, should be insignificant compared with the internal energy. Finally, a simulation with full integration is run to ensure that reduced integration is sufficient. The results are displayed in Figures 7.4a and 7.4b. As seen, there is no numerical instabilities in the model, and reduced integration is adequate.

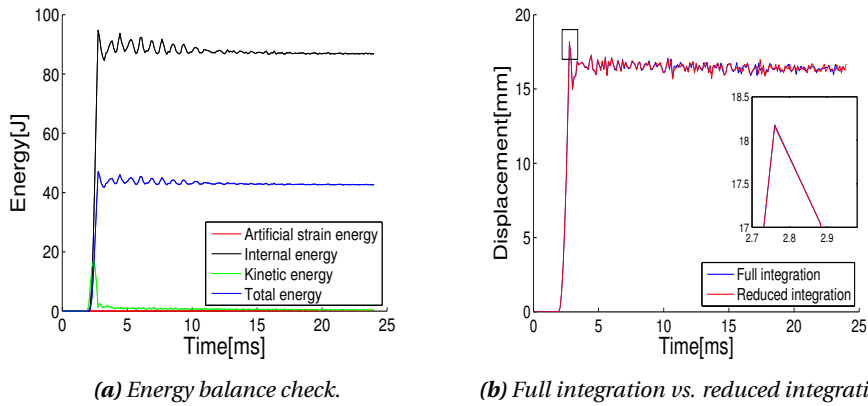


**Figure 7.4:** Verification of the established numerical model.

### 7.1.3 Numerical Results

All the shock tube experiments are simulated using the numerical model presented. To verify the use of this numerical model, the experimental data and the numerical results are compared. In the next sections, the results are displayed graphically. In addition, tables show the deviation of the maximum deflection obtained by the numerical simulations.

#### Steel Plates

The results from the numerical simulations of the steel plates are in accordance with the experimental data. While tests S0.8 – 15 and S0.8 – 25 slightly overestimates the maximum deflection, the S0.8 – 35 experiment underestimates the peak response by 0.34 %. The deviations are, however, insignificant and the steel model displays excellent results compared with the component tests.

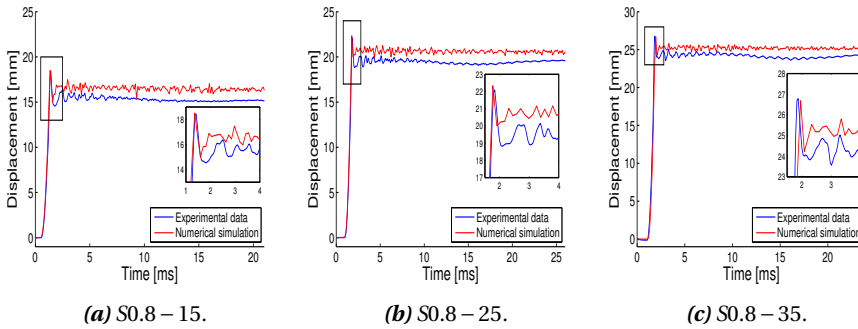


**Figure 7.5:** Numerical analyses of the 0.8mm steel plate.

**Table 7.4:** Experimental data vs. numerical results for the 0.8mm steel plate.

	Test	$u_{max}$ [mm]	Deviation [%]
Experimental data	S0.8-15	18.43	0.43
Numerical result		18.51	
Experimental data	S0.8-25	22.09	1.13
Numerical result		22.34	
Experimental data	S0.8-35	26.78	0.34
Numerical result		26.69	

### Aluminium Plates

The thinnest aluminium plates displays a larger deviation from the maximum deflection than the steel plates with the same thickness. Both tests A0.8 – 5 and A0.8 – 7.5 overestimates the initial peak with 10.51% and 7.39%, respectively. This may be reasoned in a overestimated Friedlander extrapolation, leading to a too high peak reflected pressure. Another possibility is that the actual plate thickness deviates for the nominal value used in the modelling of the numerical model. The latter statement however, contradicts the observations of the A0.8 – 7.5 plate in the metallurgic study performed in Section 5.4.

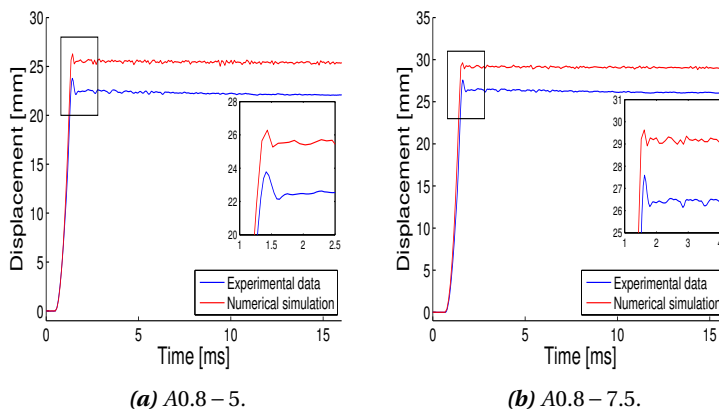


**Figure 7.6:** Numerical analyses of the 0.8mm aluminium plate.

**Table 7.5:** Experimental data vs. numerical results for the 0.8mm aluminium plate.

	Test	$u_{max}$ [mm]	Deviation [%]
Experimental data	A0.8-5	23.78	10.51
Numerical result		26.28	
Experimental data	A0.8-7.5	27.59	7.39
Numerical result		29.63	

The numerical results of the thicker aluminium plates give a better estimation of the experimental data. While the tests A2.0 – 15 and A2.0 – 25 underestimates the initial peak, the A2.0 – 35 simulation overestimates the experimental results by 5.95%. When exposed to the blast waves in the shock tube, the A2.0 – 35 experiment experience a fracture along one of the sides. In the numerical simulation, this rupture does not occur. This may be reasoned in the simplification of the boundary conditions. It may also imply that the numerical model exhibit a too stiff response.

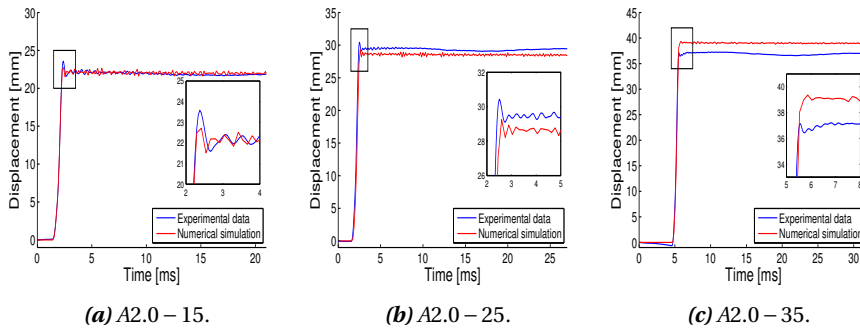


**Figure 7.7:** Numerical analyses of the 2.0mm aluminium plate.

**Table 7.6:** Experimental data vs. numerical results for the 2.0mm aluminium plate.

	Test	$u_{max}$ [mm]	Deviation [%]
Experimental data	A2.0-15	23.58	3.69
Numerical result		22.71	
Experimental data	A2.0-25	30.43	3.84
Numerical result		29.26	
Experimental data	A2.0-35	37.16	5.95
Numerical result		39.37	

### **Discussion of the Numerical Results**

It is important to be critical when evaluating the numerical results. It is challenging to recreate the shock tube experiments perfectly and consequently the simulations are based on several simplifications. The boundary conditions are not ideally represented and the same applies for the thickness of the plates. The plate thicknesses are taken from the material cards from the supplier and the variation of the thickness over the cross-section is ignored. This contradicts the discoveries that were done when measuring the dog bone specimens.

The numerical results of the steel plates are in good agreement with the experimental data. The deviations of the numerical results are greater for the aluminium plates, especially for the simulations performed of the thinnest plates. If the material input is disregarded, the numerical models for the steel and aluminium plates are identical. In Chapter 4 the material characteristics were optimized, providing a good fit for both the steel and aluminium materials. It should be noted that in the optimization procedure, one parameter is altered at a time. Therefore, the value of each parameter depends on one another. Consequently, the dependency of the parameters should be taken into consideration when evaluating the results. It is also possible that there may be an inaccuracy in the implemented Friedlander curves, causing errors in the numerical simulations.

Experiment A2.0 – 35 exhibits a fracture along one of the boundaries. However, the numerical model is not able to capture this behaviour and fracture does not occur in the simulation. This may indicate that the numerical model exhibit a too stiff response. The lack of fracture may also be a result of the simplified boundary conditions.

From an industrial perspective, the numerical simulations display sufficient accuracy. The simulation with the greatest deviation displays a maximum deflection of only 2.5mm more than the experimental data. From an design point of view, this error is insignificant. However, some of the simulations underestimates the maximum response of the plates. This implies a non-conservative solution of the plate problem, which is unfortunate in structural design.



## Chapter 8

# Parameter Studies

To investigate how different parameters influence the response of the plate, several parameter studies are conducted. The investigation of some of the parameters are based on observations done in previous chapters of this thesis. The numerical model of the 0.8mm aluminium plate displayed larger deviations than the other numerical simulations. It has been speculated if the deviations are a result of an inaccurate Friedlander curve or by a variation of the thickness over the cross-section. Consequently, it is natural to investigate these two parameters. In addition, it was not performed any blast experiments on the 2.0mm steel plates. A study is therefore performed in order to evaluate the capacity of the steel plates. Several other parameters are also investigated.

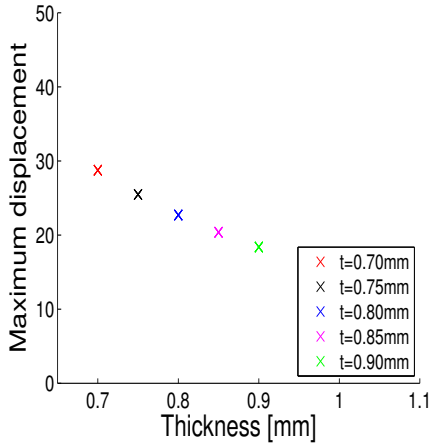
## 8.1 Plate Thickness

The plates applied in this thesis are relatively thin. When managing such small thicknesses, a small variation may be crucial for the response. It is therefore decided to study the effect of the response by altering the magnitude of the thickness. The maximum deviation from the nominal thickness is set to  $\pm 0.10\text{mm}$ .

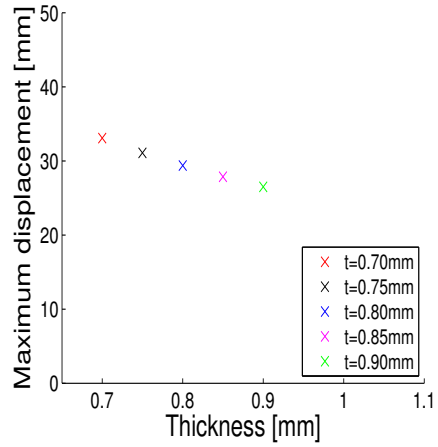
**Table 8.1:** Maximum mid-point deflection for different thicknesses.

Test	Plate Thickness [mm]	$u_{max}$ [mm]	Deviation [%]	CPU time [h:min:s]
S0.8-15	0.70	20.12	9.35	[00:00:44]*
	0.75	19.10	3.80	[00:00:44]*
	0.80	18.16	1.30	[00:00:37]*
	0.85	17.32	5.87	[00:00:37]*
	0.90	16.55	10.05	[00:00:37]*
A0.8-7.5	0.70	33.08	19.86	[00:00:42]*
	0.75	31.09	12.64	[00:00:40]*
	0.80	29.87	8.22	[00:00:37]*
	0.85	27.87	0.98	[00:00:38]*
	0.90	26.50	3.99	[00:00:38]*
A0.8-25	1.90	30.54	0.46	[00:00:41]*
	1.95	29.83	1.88	[00:00:40]*
	2.00	29.14	4.14	[00:00:35]*
	2.05	28.49	6.28	[00:00:40]*
	2.10	27.87	8.32	[00:00:38]*

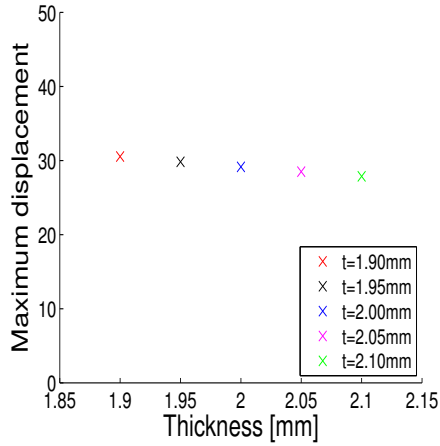
While Table 8.1 gives the tabulated values from the parameter study, Figure 8.1 graphically illustrates the maximum displacement as the thickness is altered. The numerical simulation of the steel plate gives the most accurate result when using the nominal thickness. For the A0.8 – 7.5 experiment, the simulation with an increased nominal thickness of 0.05mm gives the best accuracy. It is observed that by underestimating the thickness, the error of the simulations rapidly increases. This illustrates the sensitivity of this parameter. For the A2.0 – 25 experiment, a thickness of 1.90mm results in the least deviation from the experimental data. Consequently, different trends are shown for the various plates. The overall impression indicates that the thinnest metal plates are most affected by a change in thickness. This is naturally explained by a higher percentage increase of the thickness compared with the 2.0mm plates.



(a) S0.8-15.



(b) A0.8-7.5.



(c) A2.0-25.

Figure 8.1: Maximum displacement when altering the thickness of the plates.

## 8.2 Steel vs. Aluminium Plates

Steel and aluminium have similar structural applications. However, the two materials display important differences in both physical and mechanical properties. This must be accounted for in the design process.

Figure 8.2a shows a steel and aluminium plate with a thickness of 0.8mm subjected to the same peak reflected pressure of 348.3 kPa. While the aluminium plate displays a mid-point deflection of 52.6mm, the steel plate only experience a displacement of 18.2mm. This is related to the characteristics of the two materials.

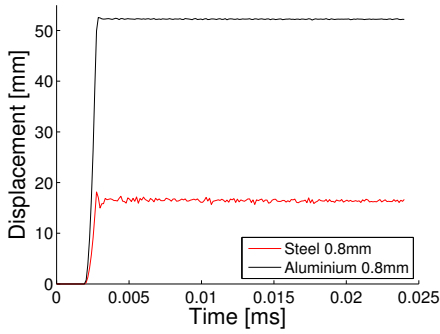
Research is conducted on an aluminium plate with a scaled thickness exposed to the same peak reflected pressure. The thickness is increased by a factor equal to the ratio of the two densities,  $\frac{\rho_{\text{steel}}}{\rho_{\text{aluminium}}}$ . This result in a plate thickness of 2.3mm.

The time-displacement history for the steel and the scaled aluminium plate are depicted in Figure 8.2b. As expected, the mid-point deflection of the aluminium plate decreases. The mid-point deflection is now 20.2mm, which corresponds to a decrease in the maximum response of 78 %.

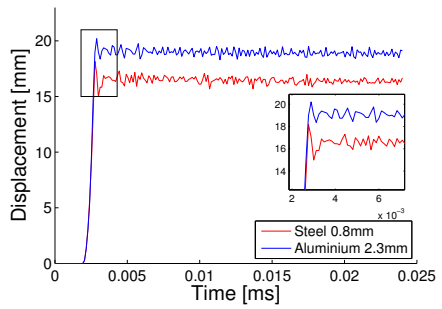
Even though the thickness has been adjusted, the 2.3mm aluminium plate still displays a maximum deflection that is greater than for steel. The mid-point deflection is 11.2 % greater for the aluminium plate than for the steel plate. It is thereby observed that even by scaling the thickness of the aluminium plate, it still can not compensate for the reduced strength that aluminium displays compared with steel.

**Table 8.2:** Physical properties and maximum mid-point displacement.

Test	$\rho$ [kg/m <sup>3</sup> ]	$E$ [MPa]	$u_{max}$ [mm]
S0-8-15	7800	210 000	18.2
A0.8-15	2710	71 000	52.6
A2.3-15			20.2



(a) Steel 0.8mm vs. aluminium 0.8mm.



(b) Steel 0.8mm vs. aluminium 2.3mm.

**Figure 8.2:** Displacement-time histories for plates exposed to a peak reflected pressure of 348.3kPa.

### 8.3 Strain rate sensitivity

The viscoplastic material parameter  $C$ , is a value determined by material tests. Since these tests are not performed in this thesis, the strain rate parameter is unknown. This variable plays an important role in how the strain hardening term in the modified Johnson-Cook model hardens. Naturally, a high  $C$  factor results in a more resistant material response.

Since the viscoplastic material parameter is not identified, a point of reference is needed. In the literature,  $C$  is given the value of 0.01 and 0.014 for steel and aluminium, respectively [1] [85]. When performing the optimization of the material behaviour, values of 0.005 and 0.01 for steel and aluminium were found to be more representative. Table 8.3 displays the different values of  $C$  that are used when performing this study.

**Table 8.3:** Maximum mid-point deflection for the viscoplastic material parameter.

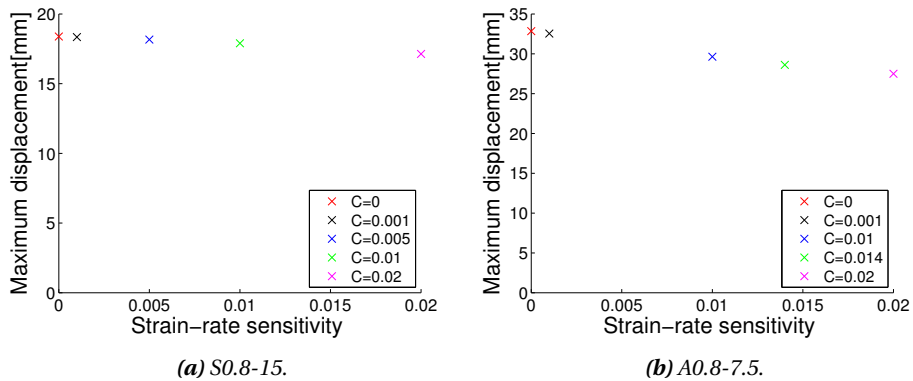
Test	C [-]	$u_{max}$ [mm]	Deviation [%]	CPU time [h:min:s]
S0.8-15	0.000	18.38	0.11	[00:00:33]
	0.001	18.34	0.33	[00:00:34]
	0.005	18.16	1.30	[00:00:34]
	0.010	17.90	2.72	[00:00:37]
	0.020	17.13	6.90	[00:00:38]
A0.8-7.5	0.000	32.84	18.99	[00:00:30]
	0.001	32.54	17.89	[00:00:30]
	0.010	29.63	7.36	[00:00:30]
	0.014	28.60	3.62	[00:00:33]
	0.020	27.49	0.39	[00:00:31]

Table 8.3 indicates that by neglecting the strain hardening term the simulation of the S0.8 – 15 experiment gives the best accuracy. By increasing the value of  $C$ , the stiffness of the response is greater and consequently the error of the simulation increases. The value applied in the numerical model provides an improved result compared to the value given in the literature.

For the A0.8 – 7.5, the numerical simulations display better accuracy as the  $C$  parameter increases. This may illustrate that the aluminium is a viscoplastic material. As mentioned in Chapter 4, a material as pure as the aluminium alloy EN AW-1050A-H14 is very strain rate sensitive. Consequently, the material is more effected by the value

of the strain rate parameter compared with Docol 600 DL steel. The  $C$  parameter from the literature is more suitable than the value obtained from the inverse modelling. This illustrates one of the consequences by optimizing a material behaviour dependent on several parameters.

The results from this parameter study are illustrated in Figure 8.3.



**Figure 8.3:** Maximum displacement for the chosen strain-rates.

## 8.4 Pressure Distribution

The pressure applied to the plate is described by the Friedlander Equation (3.5). In Section 5.3.2, a curve fitting tool were used to obtain the three unknown parameters of this equation; the reflected overpressure  $P_r$ , the positive duration  $t_+$  and the decay coefficient  $b$ . When investigating how the pressure distribution influences the response of the plate, two approaches are possible,

- $P_r$  and  $b$  are held constant, while  $t_+$  varies
- $t_+$  and  $b$  are held constant, while  $P_r$  varies

The procedures are illustrated in Figure 8.4.

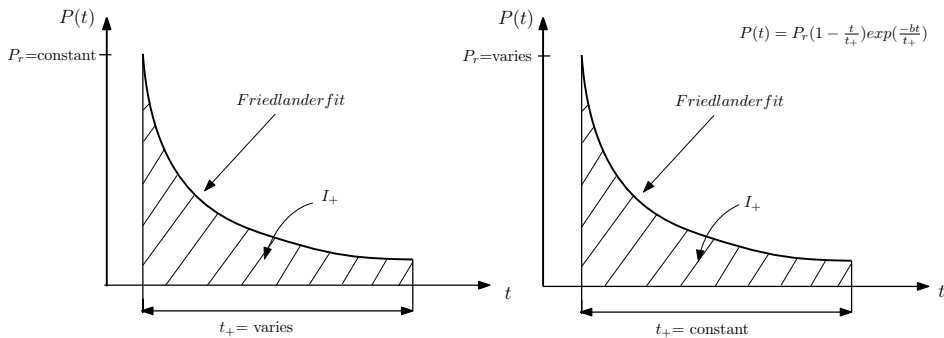


**Figure 8.4:** Friedlander fit with constant pressure and period, respectively.

The Friedlander parameters for the chosen steel and aluminium experiments are displayed in Table 8.4.

**Table 8.4:** Friedlander parameters for the experiments.

Test	$P_r$ [kPa]	$t_+$ [ms]	$b$ [-]
S0.8-15	348.3	22.9	1.3
A0.8-7.5	187.3	18.6	0.8

The chosen peak pressures and periods together with the impulse of the positive phase and the maximum displacement, are displayed in Tables 8.5 and 8.6. The values obtained in the experiment are used as a reference, when choosing which peak pressures to test. To get a representative selection of the peak pressures, both lower and higher



values of the reference pressure are tested. To focus on the effect of altering the peak pressure and the period, it is desirable to exclude the possibility of the plate to go to fracture. Hence, when studying the aluminium plate, only peak reflected pressures less than 345.4 kPa are used in the analyses.

The blast loads applied to the plates are characterized as dynamic. Consequently, an increase of the maximum deflection is expected as the magnitude of the peak reflected pressure increases. This trend is clearly shown in Figure 8.5. Compared with the steel plate, the maximum deflection of the aluminium plate increases more rapidly as a greater peak reflected pressure is applied. This is related to the material characteristics.

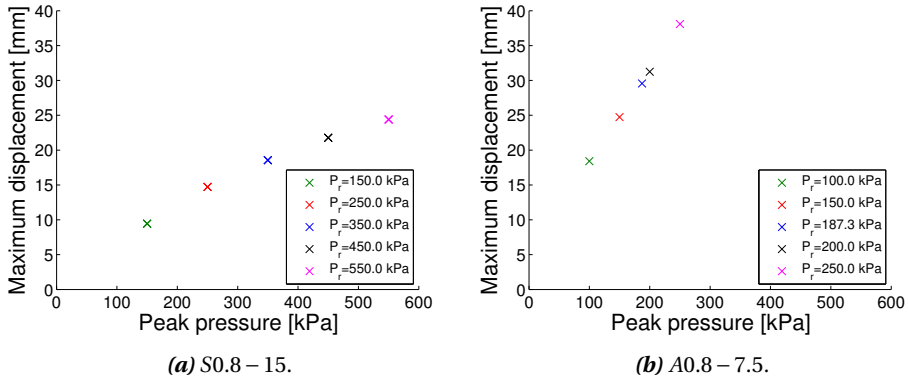
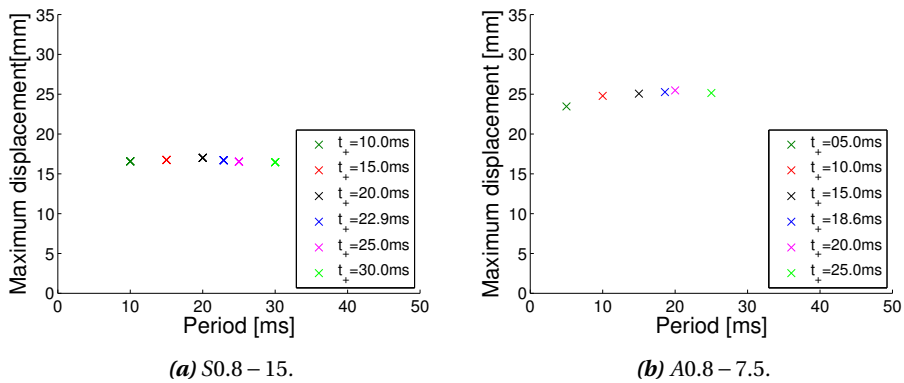


Figure 8.5: Maximum mid-point deflection for different peak reflected pressures.

Table 8.5: Maximum mid-point deflection for different peak reflected pressures.

Test	$P_r$ [kPa]	$I_+$ [kPa × ms]	$u_{max}$ [mm]	CPU time [h:min:s]
S0.8-15	150	1154.30	9.44	[00:00:36]*
	250	2680.30	14.71	[00:00:34]*
	350	2693.40	18.56	[00:00:39]*
	450	3462.90	21.77	[00:00:39]*
	550	4232.50	24.39	[00:00:34]*
A0.8-7.5	100	712.32	18.41	[00:00:29]*
	150	1068.59	24.74	[00:00:36]*
	187	1334.20	29.57	[00:00:28]*
	200	1424.60	31.25	[00:00:33]*
	250	1780.80	38.10	[00:00:32]*

The period does not affect the deflection of the plates to the same extent as when altering the peak pressure. The plates only expose a small change of the maximum displacement when the positive duration is altered. This is illustrated in Figure 8.6. Intuitively, the maximum displacement should increase as the impulse increases. While the aluminium plate displays these characteristics, the steel plate has a rather counter-intuitive behaviour. When the duration exceeds 20 ms, the displacement decreases as the impulse increases. It is assessed if these results are caused by discretization of the pressure-time history curve in Abaqus.



**Figure 8.6:** Maximum mid-point deflection for different positive durations.

**Table 8.6:** Maximum mid-point deflection for different positive durations.

Test	$t_+$ [ms]	$I_+$ [kPa × ms]	$u_{max}$ [mm]	CPU time [h:min:s]
S0.8-15	10	1005.80	16.57	[00:00:23]*
	15	1524.70	16.74	[00:00:26]*
	20	2040.00	17.00	[00:00:34]*
	23	2338.10	16.71	[00:00:39]*
	25	2553.90	16.53	[00:00:41]*
	30	3067.20	16.46	[00:00:48]*
A0.8-7.5	5	266.30	23.46	[00:00:16]*
	10	579.29	24.79	[00:00:19]*
	15	880.49	25.06	[00:00:27]*
	19	1095.30	25.26	[00:00:32]*
	20	1179.20	25.47	[00:00:32]*
	25	1476.90	25.15	[00:00:40]*

The results from this parameter study reveals some important aspects of the blast loading. Since the loading is defined in the dynamic domain, the entire pressure-time history is important for the response of the plate. It is observed that by keeping the peak reflected pressure and the decay coefficient constant, and by only changing the period, the mid-point deflection displays small variations. This illustrates the importance of the peak reflected pressure compared with the duration of the period.

## 8.5 Material Parameters

In order to obtain a representative material response, it is crucial to have a good description of the material. In Chapter 4, both direct and inverse methods are used when characterizing the material behaviour. While the direct model (two Voce terms) gives a good description of the material before necking, the inverse model (three Voce terms) gives the best fit after necking. It is interesting to investigate if the initial model gives sufficient results or if a more complex model is necessary to achieve a satisfying plate response.

The direct model applied in the simulations is based on the specimen that displayed the best fit of the material behaviour during the tensile tests in Chapter 4. The numerical results of the two methods are displayed in Table 8.7. In addition, the material curves and the displacement-time history of the two modelling approaches and the experimental data are obtained.

**Table 8.7:** Maximum mid-point deflection for different material models.

Test	Model	$u_{max}$ [mm]	Deviation [%]	CPU time [h:min:s]
S0.8-35	Direct	27.7	3.4	[00:00:30]
	Inverse	26.7	0.4	[00:00:40]
A0.8-7.5	Direct	27.5	0.4	[00:00:27]
	Inverse	29.6	7.2	[00:00:31]
A2.0-35	Direct	37.9	1.6	[00:00:40]
	Inverse	39.4	5.6	[00:00:54]

The material curves for the 0.8mm steel plate in Figure 8.7a, are almost identical for the direct and inverse methods. However, Figure 8.7b illustrates how the direct model slightly overestimates the initial peak compared with the inverse approach. While the inverse model deviates 0.4% from the maximum response, the direct model displays an error of 3.4% from the experimental data.

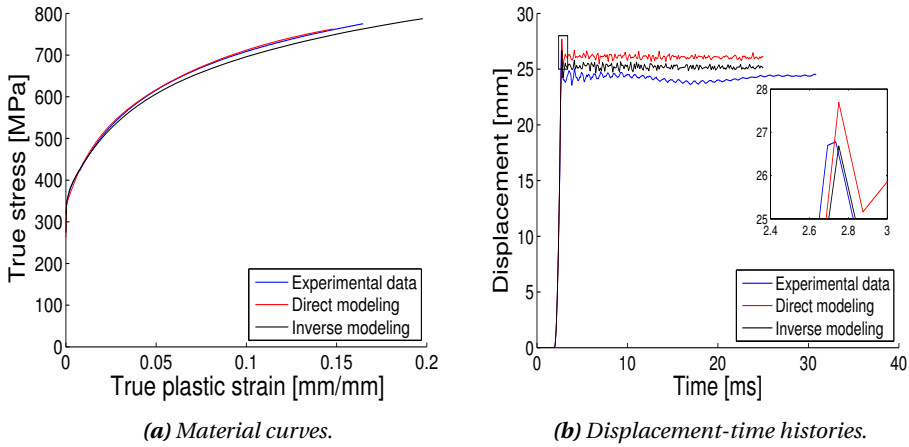


**Figure 8.7:** Numerical results of test S0.8 – 35 for direct and inverse material models.

By studying Figure 8.8a, there is a significant change in the curves of the direct and inverse method, for small plastic strains. This may be related to the direct approach using too few data points when creating the curve. In general, the plate problem exhibits small strains. Consequently, the beginning of the plastic strain curve is important. Since the direct model experiences smaller stresses than the inverse model in this area, the direct model may exhibit a smaller mid-point deflection. This leads to a better fit of the direct model compared with the experimental data.

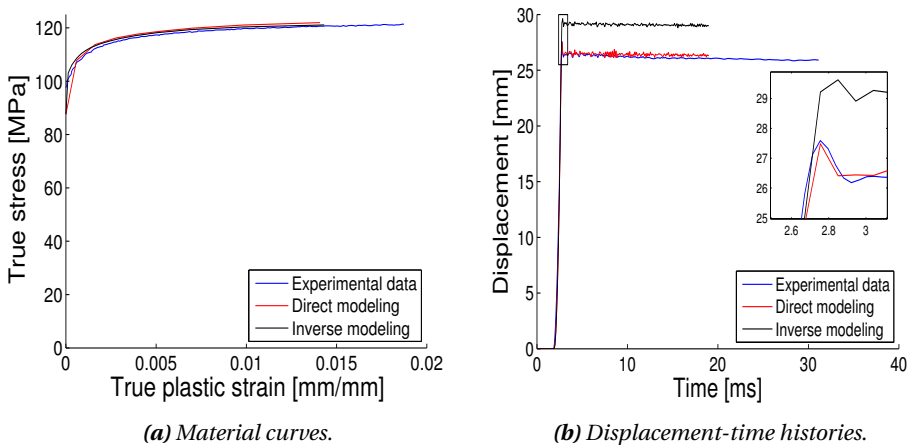


**Figure 8.8:** Numerical results of test A0.8 – 7.5 for direct and inverse material models.

Figure 8.9a displays material curves of the 2.0mm aluminium plate. The curves exhibit the same trend as for the thinner plates. In the beginning of the curve, the inverse model experiences higher stresses than the direct model. This leads to a better representation of the mid-point deflection by utilizing a direct approach.

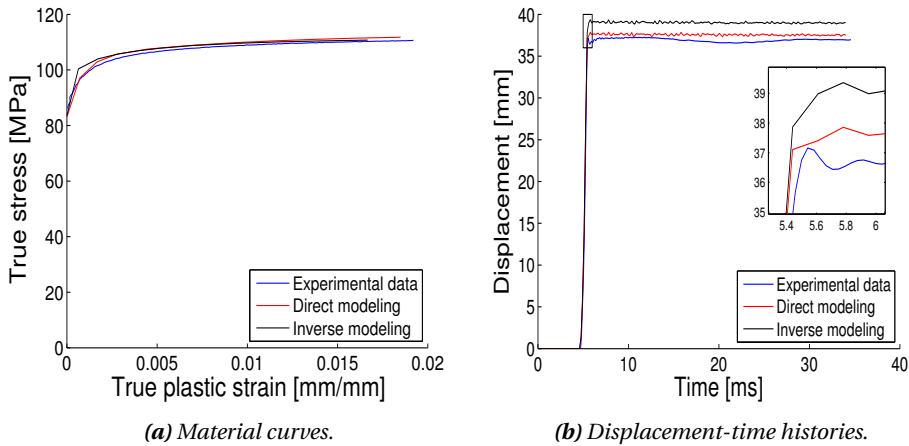


**Figure 8.9:** Numerical results of test A0.8 – 35 for direct and inverse material models.

It is reasonable to be familiar with the strains occurring in the experiments, before choosing a suitable material approach. From an industrial point of view, simple models are preferable when finding the material characteristics. While the inverse model is time consuming and requires experience to execute, the direct method is more effective. By evaluating the results from this numerical study, it is revealed that for the aluminium plates a direct approach is suitable concerning both the accuracy and efficiency of the analyses. For the analyses of the steel plate, the inverse model gives a slightly better result. However, the difference in accuracy of the direct and inverse method are too small to make up for the computational time it takes to execute the inverse analyses. Consequently, for the analyses performed in this thesis, a direct approach is sufficient.

## 8.6 Temperature

The shock tube experiments generate a high-speed blast wave. Consequently, it is interesting to investigate the temperature development when impact occurs. The finite element method calculates a temperature change independent on how rapid the strains in the structure develop. However, the temperature increase is highly coupled to the strain rate. If a load is applied quasi-static, heat transfer to the environment occurs. On the contrary, if the loading is applied rapidly (as in the shock tube experiments) the temperature increase remains concentrated in the material. The latter effect is called an adiabatic process, where there is no heat transfer into or out of the system.

When considering the temperature, there are three options regarding the temperature mechanism. Either the process is defined as isotropic, as adiabatic or as a thermo-coupling. Due to the complexity of a thermo-coupling, only the isotropic and adiabatic processes are investigated in this study.

Until now, the thermal softening term included in the constitutive relation in Equation (7.1) in Chapter 3, has been neglected by defining an isotherm process. Equation (8.1) illustrates the temperature change. It includes the Taylor-Quinney factor  $\chi$ , which presents the part of plastic work converted into heat. To represent adiabatic and isotherm conditions,  $\chi$  is set to 0.9 and 0.0, respectively.

$$\Delta T = \int_0^p \frac{\chi \sigma_{eq}}{C_p \rho} dp \quad (8.1)$$

Figure 8.10 illustrates the transformation from isothermal to adiabatic conditions. The relation between the total strain rate and the thermodynamic conditions is deduced by Lindholm and Johnson [87]. The threshold values are only approximate and they are normally used as a rule of thumb. As depicted, the thermodynamic state changes from isotherm to adiabatic as the total strain rate increases. For aluminium, the alteration of the conditions starts at a strain rate of 100. For steel this transition does not occur until the strain rate reaches 1000. In Equation (8.1) it is evident that the temperature supplement depends on the equivalent plastic strain rate and not the total strain rate used in Figure 8.10. However, as long as the load is applied monotonically, the total

strain rate gives a fair approximation of the equivalent plastic strain rate.

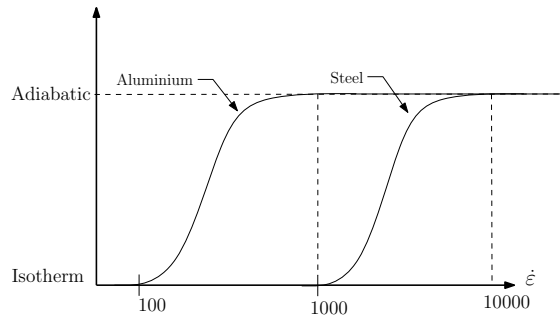


**Figure 8.10:** Transition from isothermal to adiabatic conditions [87].

By evaluating Table 8.8 and Figure 8.11, the results imply that the materials are not remarkably affected by the temperature softening term. Both steel and aluminium exhibit relatively small strain rates, hence it is not a large temperature change in the material.

**Table 8.8:** Maximum mid-point deflection for different values of  $\chi$ .

Test	$\chi$ [-]	$u_{max}$ [mm]	$\dot{p}_{max}$ [s <sup>-1</sup> ]	CPU time [h:min:s]
S0.8-15	0.00	18.16	104.4	[00:00:37]
	0.90	18.16	104.5	[00:00:33]
A0.8-7.5	0.00	29.63	236.9	[00:00:35]
	0.90	29.67	237.1	[00:00:35]

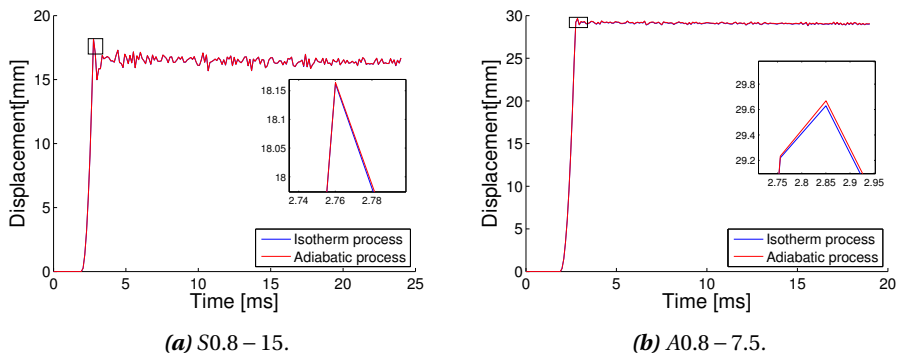


**Figure 8.11:** Displacement-time history for isotherm and adiabatic processes.



## 8.7 Capacity of the Steel Plates

By conduction numerical simulations of the steel plates, it is possible to get an estimation of the maximum mid-point deflection for various peak reflected pressures. It is desirable to investigate the magnitude of the peak reflected pressure that leads to fracture of the 0.8mm and 2.0mm steel plates.

The pressure applied to the plates is described by the Friedlander equation. In this study, the decay coefficient  $b$  and the positive duration  $t_+$  is set to 2.5 and 35.7ms, respectively. These values are based on observations from the previous shock tube experiments. The peak reflected pressure  $P_r$  is altered and adjusted before performing the simulations.

A considerable amount of simulations have been run, but only a few are displayed in Table 8.9. The results imply that a peak reflected pressure of approximately 4200 kPa will lead to fracture of the thinnest plates. For the thicker plates, the pressure must exceed 10000 kPa for fracture to occur. As explained in Chapter 5, the maximum driver pressure is limited by the volume of the driver section and the tolerance level of the shock tube. With these factors considered, the maximum obtainable driver pressure is of 17MPa. Due to the accessible diaphragms and the adjusted volume, it is only possible to subject the plates in this thesis to a peak reflected pressure of 2400kPa. As observed, greater pressures are needed to obtain fracture of either of the plates.

**Table 8.9:** Maximum mid-point deflection for different peak reflected pressures.

Test	$P_r$ [kPa]	$I_+$ [kPa×ms]	$u_{max}$ [mm]	CPU time [h:min:s]
S0.8	1000	8998	37.23	[00:00:34]
	2100	18896	66.22	[00:00:37]
	3100	27894	94.27	[00:00:41]
	4100	36892	128.99	[00:00:41]
	4200	37792	Fracture	[00:00:48]
S2.0	1800	16196	28.41	[00:00:35]
	5000	44990	60.96	[00:00:36]
	9000	80982	106.67	[00:00:39]
	10000	89980	121.29	[00:00:39]
	10700	96279	Fracture	[00:02:02]

In figure 8.12, an illustration of a 0.8mm steel plate that fractures is given. As depicted, the propagation of the yield lines is prominent. As already mentioned, the simulations are based on a number of simplifications. When using the Cockcroft-Latham fracture criterion, an element size less than  $1.0 \times 1.0\text{mm}^2$  is recommended. It is evident that the mesh of this model is too coarse to fulfill this requirement. In addition, the boundary conditions are not perfectly represented, and the energy balance is off. All these factors influence the fracture pattern of the plate, which is seen to not be entirely realistic.

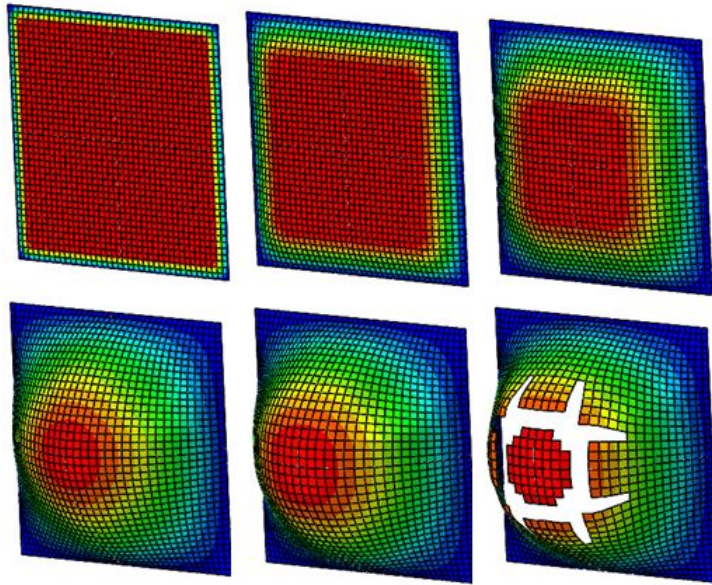


*Figure 8.12: Fracture process of a 0.8mm steel plate.*

## 8.8 Forming Limits

Based on theory around the subject of forming limits given in Section 3.4 in Chapter 3, Hopperstad et al. have developed an FLD calculator [88]. By entering certain information about the material characteristics, the calculator determines the forming limit diagram (FLD) and the strain path for the material of interest. Some of the input variables are the strain ratio  $\beta$ , the critical strain rate ratio  $\beta_{cr}$ , the strain rate, the hardening rule, the yield criterion and an inhomogeneity factor.

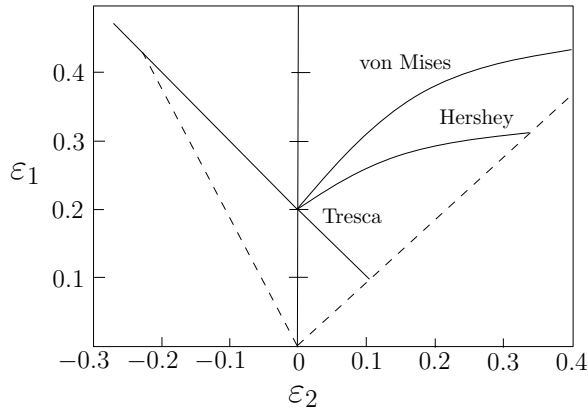


**Figure 8.13:** Forming limit diagram for the three yield criteria; Von Mises, Tresca and Hershey.

While all the numerical simulations performed in this thesis apply the von Mises yield criterion, the FLD calculator employs the high-exponent Hershey criterion. The motivation for using another yield criterion is reasoned in a more conservative solution, as illustrated in Figure 8.13. The Hershey criterion is a generalized isotropic and pressure independent yield criterion, where the yield surface is located between the Tresca and von Mises surface. The criterion is expressed as,

$$f(\sigma_1, \sigma_2, \sigma_3) = \left( \frac{1}{2} \left( |\sigma_1 - \sigma_2|^m + |\sigma_2 - \sigma_3|^m + |\sigma_3 - \sigma_1|^m \right) \right)^{\frac{1}{m}} - \sigma_Y = 0 \quad (8.2)$$

where  $\sigma_1$ ,  $\sigma_2$  and  $\sigma_3$  are the three principal stresses,  $\sigma_Y$  is the stress at yielding, and  $m$  determines the curvature of the yield surface.

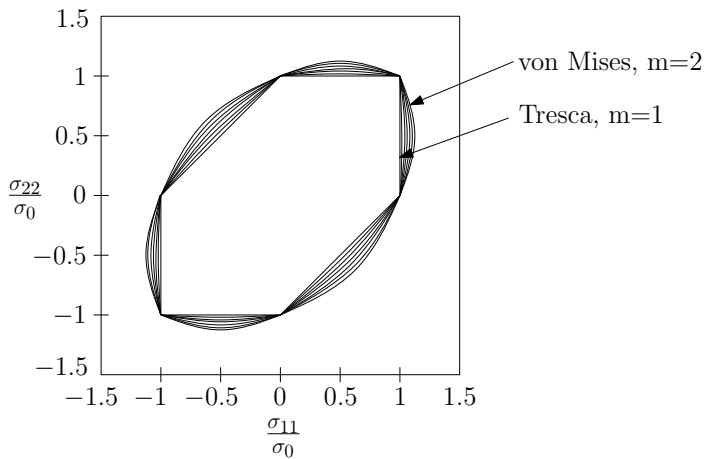


**Figure 8.14:** Geometric representation of the high-exponent yield criteria for plane stress [52].

Figure 8.14 illustrates the yield surface for different values of the  $m$  parameter. While using  $m = 2$  corresponds to the von Mises criterion,  $m = 1$  is equivalent to the Tresca criterion. It is seen that by increasing the value of  $m$ , the equation approaches the Tresca criterion. For ferrite steels with a body centred cubic (bcc)  $m = 6$ , and for aluminium alloys with a faced centred cubic (fcc)  $m = 8$ . Since the numerical model uses the von Mises yield criterion, a modification of the material card is necessary. Consequently,  $m$  is set to 6 and 8 for steel and aluminium [89], respectively. To increase the accuracy of the simulation, the element size is reduced to  $1 \times 1\text{mm}^2$ .

Numerical simulations are run to observe where the major  $\varepsilon_1$  and minor  $\varepsilon_2$  principle strains are located in the forming limit diagram. The different forming limit diagrams and strain path plots are depicted in Figures 8.15-8.18. As shown in Table 8.10, simulations are conducted for all the shock tube experiments. The analyses also include the 2.0mm steel plate where the applied blast load is taken from the capacity study of the steel plates.

**Table 8.10:** Major and minor principle strains for the different analyses.

Test	$\epsilon_1$ [-]	$\epsilon_2$ [-]	CPU time [h:min:s]
S0.8-15	0.0120	0.0117	[01:17:22]**
S0.8-25	0.0162	0.0161	[01:15:05]**
S0.8-35	0.0236	0.0236	[01:01:17]**
S2.0-50	0.1123	0.1122	[01:04:45]**
S2.0-90	0.3152	0.2417	[01:14:47]**
S2.0-1070	0.5850	0.2815	[00:34:55]**
A0.8-5	0.0263	0.0263	[01:36:01]**
A0.8-7.5	0.0335	0.0335	[01:10:10]**
A0.8-10	0.0896	0.0866	[01:10:39]**
A2.0-15	0.0166	0.0166	[01:27:57]**
A2.0-25	0.0274	0.0274	[01:38:16]**
A2.0-35	0.0502	0.0502	[01:29:06]**

When evaluating the FLD for the steel plate with a thickness of 0.8mm, the major and minor principle strains for the various experiments are positioned in the same area. The points are located underneath the FLC, hence localized necking is not a problem. This is in good agreement with the experimental results.

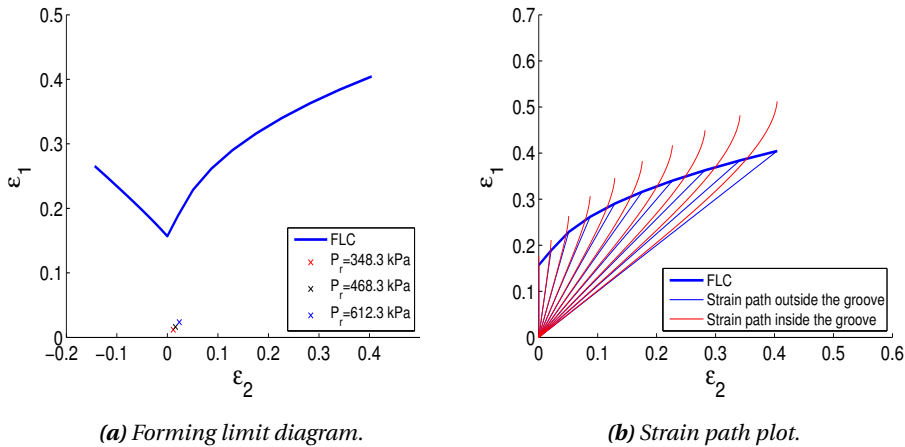


**Figure 8.15:** The 0.8mm steel plate.

When choosing the applied pressure of the 2.0mm steel plates, the highest pressure that leads to fracture is used. In addition, two pressures that only lead to deformation of the plate are chosen. In accordance with the study in Section 8.7, the FLD illustrates fracture of the plate subjected to a peak reflected pressure of 10,7 MPa. The FLD also

correctly indicates that the two smaller pressures do not lead to localized necking.

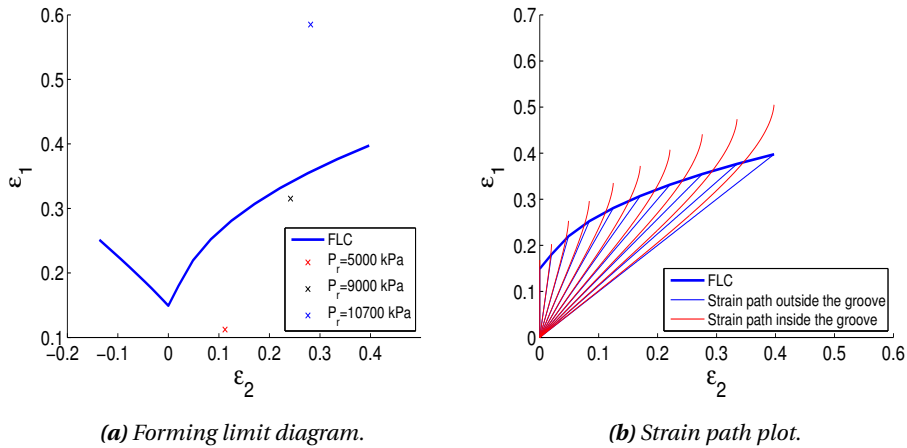


**Figure 8.16:** The 2.0mm steel plate.

As expected, the strain points of the 0.8mm aluminium plate with pressures of 161.5kPa (A0.8 – 5) and 187.3kPa (A0.8 – 7.5), are localized under the FLC. In the shock tube experiment the A0.8 – 10 plate is completely torn out of the clamping frame. Ideally, this should be revealed by the FLD with a localization of the point over the forming limit curve. As seen, the point is mistakenly placed underneath the FLC. This is reasoned in an imprecise material behaviour of the numerical model. Since fracture does not occur in the numerical analyses, the major and minor principal strains imply that structural damage will not occur. This illustrates the importance of using an accurate numerical model when evaluating a structure based on the forming limit diagram.

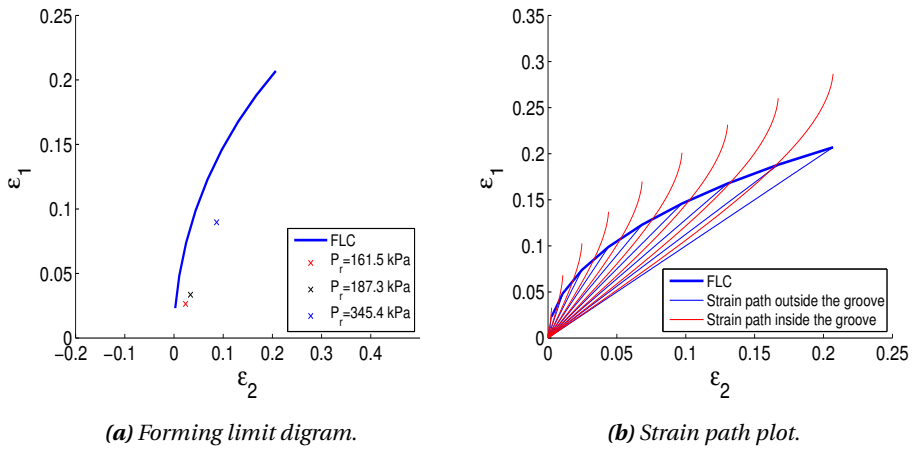


**Figure 8.17:** The 0.8mm aluminium plate.

The results from the 2.0mm aluminium plate display the same trend as for the thinner plate. While two of the points are positioned correctly under the curve, the third point is mistakenly given a characteristic that says fracture is not a problem. This is misleading since fracture did occur along one of the boundaries.

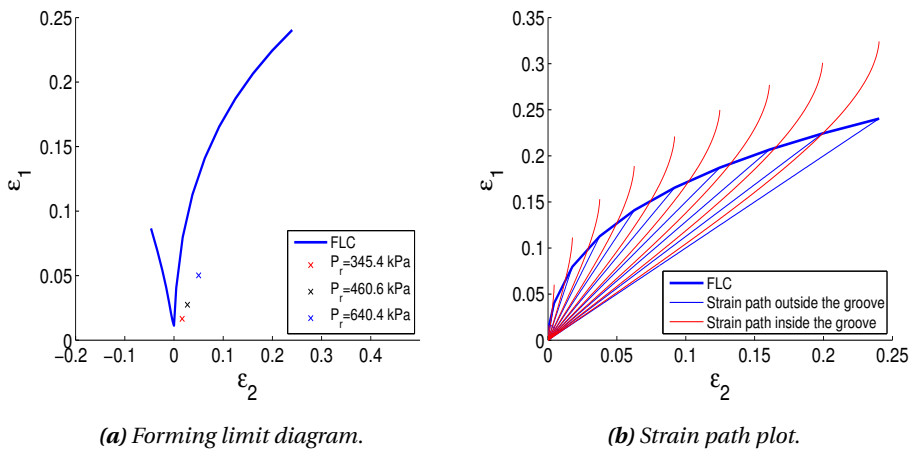


**Figure 8.18:** The 2.0mm aluminium plate.





# Chapter 9

## Discussion

The main observations from the previous sections are presented and discussed in this chapter. This includes findings from the shock tube experiments and the analytical study, in addition to the results from the numerical analyses.

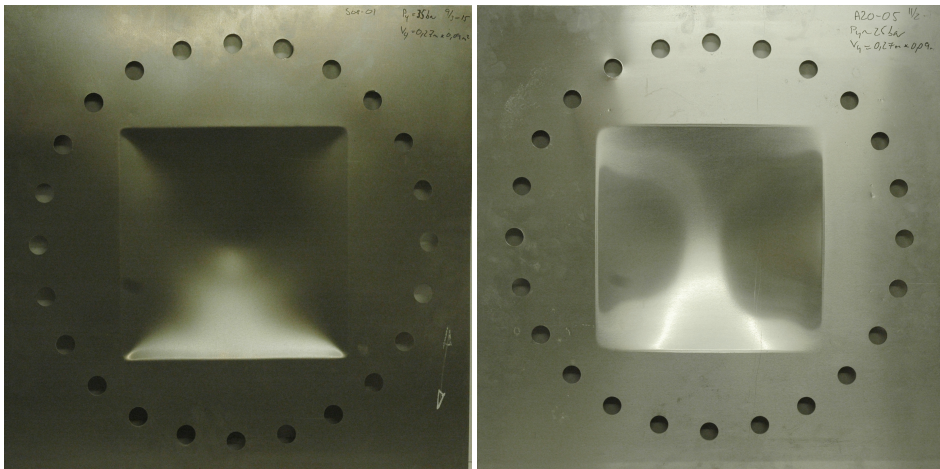
### Shock Tube Experiments

#### Calibration Tests

The pressure distribution and the repeatability of the shock tube experiments are investigated in Chapter 5.2. The results display a uniform pressure distribution over the plate for all the experiments. However, in some of the repeatable tests there are irregularities in the peak reflected pressure and noise in the recorded pressure-time history. This may be caused by variations in the firing pressure, and debris from ruptured diaphragms located in the driven section during the experiments. By evaluating the shape of the pressure-time histories from the calibration experiments, it is evident that the shock tube is able to recreate far-field explosion scenarios.

**Component Tests**

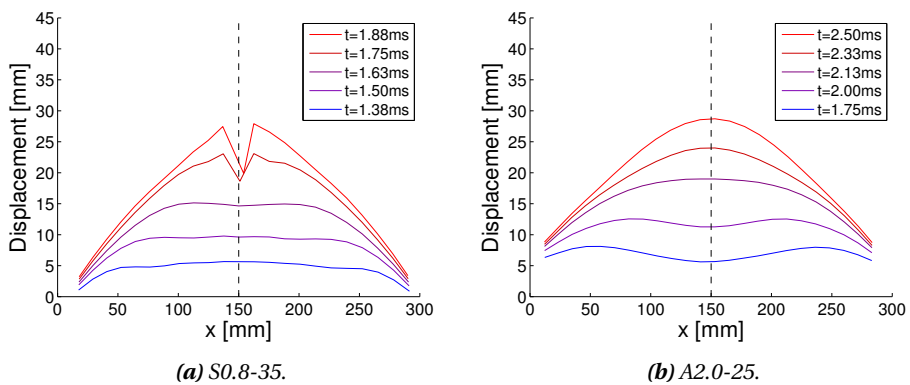
When studying the plates after being exposed to blast loading, a similar deformation pattern is identified for the two materials. Figure 9.1 illustrates a typical deformation pattern of both a steel and aluminium plate. As depicted, the yield lines are more prominent for the steel plate as the aluminium plate displays a more arced response. This may be related to the difference in stiffness between the two plates.



(a) S0.8-35.

(b) A2.0-25.

**Figure 9.1:** Deformation of the plates from the shock tube experiments.



(a) S0.8-35.

(b) A2.0-25.

**Figure 9.2:** Response process over the cross-section for shock tube experiments.

Figure 9.2 displays the mid-point deflection over the cross-section of the plates illustrated in Figure 9.1. Five time steps are shown to illustrate the progression of the deflection process. While the first frame shows the response immediately after loading, the last frame is taken when the plate reaches maximum deflection. The illustrations display how the yield line initiates from the edge and gradually propagates towards the center of the plates. For the aluminium plate, the response rapidly converges to a smooth response. The initial curvature of the aluminium plate and the disturbance of the two last frames of the steel plate, are caused by noise in the DIC data.

As mentioned in Chapter 5.3.3, two of the aluminium plates experience fracture. While experiment A2.0 – 35 displays a tearing along one of the boundaries, test A0.8 – 10 is completely torn out of the clamping frame. For both of the plates, the fracture is initiated at the boundary. This may be related to the clamping of the plates to the end flange. By evaluating the clamping set up, it is observed that sharp edges might influence the response by provoking damage, especially for the aluminium plates. This is shown in the metallurgical study in Section 5.4. The sharp edges must be investigated to make sure that the clamping mechanisms do not interfere with the response of the plate.

## **Analytical Calculations**

In impact related problems, the underlying mechanisms are often so complex that it is problematic to establish an exact mathematical model. The different analytical techniques are therefore based on multiple assumptions and simplifications.

As seen in Chapter 6, the empirical model by Nurick and Martin give a poor representation of the expected mid-point deflection of the plate. This is related to a difference in loading domains between the shock tube experiments and the experiments used to obtain the empirical model. The general yield line theory severely underestimates the collapse load of the plates. By including membrane forces, the result improves leading to collapse loads that are slightly overestimated. This is in agreement with the yield line theory providing an upper bound solution.

The poor approximations of the analytical methods can be related to the characterization of the loading. The pressure load is classified as dynamic, making the plate problem too complex for an analytical approach. By establishing a pressure-impulse diagram as explained in Section 6.4, it is possible to evaluate if the structure is exposed to a loading that causes structural damage. Unfortunately, there was not enough time to develop a P-I diagram for the shock tube experiments in this thesis. It is therefore suggested that this is a subject for further work.

## **Numerical Simulations**

The numerical model is effective and simple, yet it manages to recreate the response process of the plates in a good manner. The model generates the same yield lines as shown in the plates from the experiments, and the maximum response is reasonably represented for all of the plates tested in this thesis.

In order to achieve such an efficient model, some simplifications have been made. In the shock tube facility, the plates are clamped to the end flange using bolts and a clamping frame. This results in boundary conditions that are somewhere between simply supported and fixed. In the numerical model the boundary conditions are in general assumed fixed. A complete design of the plate with the bolts and the clamping frame is possible. However, this is time consuming and more assumptions must be introduced. Consequently, errors can easily occur when managing such a complex model. Due to the sufficient results of the numerical analyses, it is both economic and efficient to employ a simplified model.

When considering flexible structures exposed to blast loadings, fluid-structure interaction (FSI) may be employed. In order to solve a FSI problem efficiently, a fully coupled Eulerian-Lagrangian analysis can be applied. In this thesis, it has been chosen to omit the fluid description of the loading. Instead, an explicit approach with a Lagrangian formulation has been applied in all the simulations. Since the plate problem is relative simple and with finite deflections, it has been shown that a Lagrangian approach is sufficient for the applications of this thesis.

Figure 9.3 illustrates the deflection over the cross-section for the simulated steel and

aluminium plates. The numerical response processes are compared with the experimental results in Figure 9.2. The response pattern for the steel plate are in accordance with the experimental results. When evaluating the aluminium plate, the numerical results display prominent yield lines. The experimental data, however, experience a more smooth response over the entire cross-section of the plate.

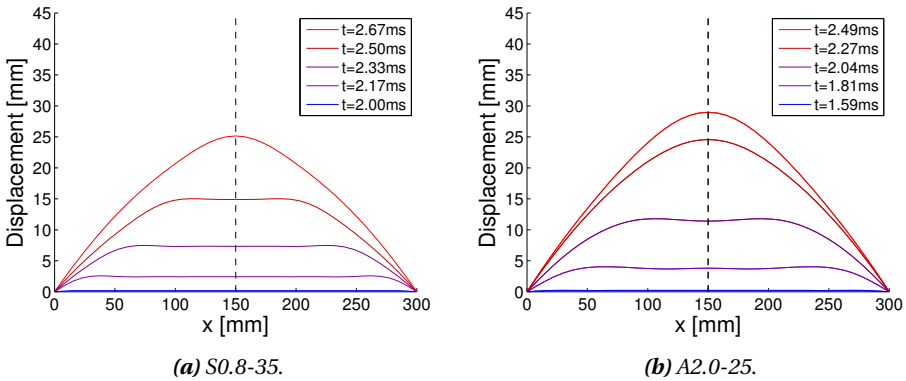


**Figure 9.3:** Response process over the cross-section for numerical simulations.

By evaluating the numerical simulations with the shock tube experiments, the results are adequate. While the 0.8mm steel plate provides the most accurate results, the numerical model of the 0.8mm aluminium plate deviates the most from the experimental data. In the parameter study of the thickness, the result of a 0.85mm aluminium plate experiences the smallest deviation of only 0.98 %. This may indicate an actual plate thickness slightly greater than the nominal value. This is counter-intuitive compared with the observations obtained from the metallurgic study in Section 5.4, which showed a good correlation between the measured and nominal thickness. It is important to know that there are several factors affecting the outcome of the numerical simulations.

From the results in Chapter 8, it can be seen that the magnitude of the peak reflected pressure has a considerable influence on the maximum deflection. This is a natural outcome as the blast load is characterized in the dynamic domain. The result also reveals that a small change of the plate's thickness can cause significant alterations of the mid-point deflection. The effect is greater for the thinner plates. This is reasonable since both thicknesses are subjected to the same alteration in mm. Hence, the thinnest plates are changed with a higher percentage of its initial thickness.

In Section 8.8, forming limit diagrams are constructed. Even though such diagrams are developed to discover potential structural damage, the FLDs calculated in this study were not able to capture the effects of the fractured aluminium plates. The diagrams indicate that the capacity of the plates are sufficient, and that local necking or fracture will not occur. This provides non-conservative results of the plate response for these simulations.

Since two of the aluminium plates experience failure, it is interesting to evaluate if the numerical model is able to detect this behaviour. In the simulations performed in this thesis, the Crockcroft Latham failure criterion is employed. According to this criterion, an element size of  $1 \times 1 \text{mm}^2$  provides a more realistic material behaviour than by using a coarser mesh. Figure 9.4 illustrates the fracture pattern of two analyses with element sizes of  $7.5 \times 7.5 \text{mm}^2$  and  $1.0 \times 1.0 \text{mm}^2$ . While the simulation with a coarse mesh experiences fracture in the middle of the plate, the refined model experiences a more complex fracture response. The latter fracture pattern is compared with the high-speed images from Chapter 5. The plates subjected to the blast load in the shock tube, experience tearing along the boundaries before the entire plate is torn out of the clamping frame. In the numerical model, a distinct fracture is displayed in the middle of the plates simultaneously as they rupture along the boundaries. Consequently, there are some differences between the response of the numerical model and the experimental results. However, the main objective of this thesis has been to compare the mid-point deflections. Since these deflections are relatively small, fracture has not been investigated in detail. It is therefore proposed that this is a subject for further work.

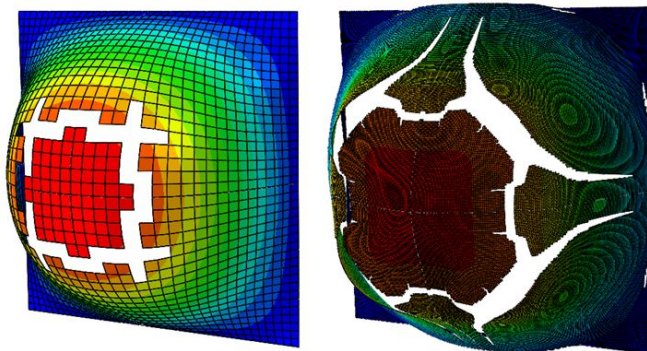


**Figure 9.4:** Fracture patterns of FE models with element sizes of  $7.5 \times 7.5 \text{mm}^2$  and  $1.0 \times 1.0 \text{mm}^2$ .

# Chapter 10

## Conclusion

In this thesis, experiments and numerical simulations have been conducted in order to investigate the response of steel and aluminium plates exposed to blast loading. The experiments were performed in the new shock tube facility at SIMLab at NTNU. One of the intentions with this thesis was to verify the pressure distribution on the test objects in the shock tube. In addition, the component experiments were recreated numerically. Subsequently, the numerical model was studied and compared with the experimental results.

After conducting the experimental and numerical research of this thesis, the following conclusions have been drawn,

- The shock tube facility at SIMLab has proven to be an effective laboratory instrument, that provides reliable results without significant costs.
- Analytical solutions of the plate problem did not provide sufficient results due to the complexity of the dynamic blast loading.
- By introducing a simple numerical model, the finite element program Abaqus CAE managed to recreate the blast problem efficiently and with adequate accuracy. Consequently, a complex FSI model has proven to be redundant for the analyses performed in this thesis.

- By performing parameter studies, the peak reflected pressure and the assigned thickness of the plate were found to affected the maximum mid-point deflection the most.
- Due to relatively small strains in the component experiments, a direct modelling approach proved to give sufficient results of the numerical analyses.



# Chapter 11

## Further Work

Due to limited time when writing this thesis, it was not possible to conduct all the research initially intended. There were several aspects related to the experimental work and the numerical simulations that would be interesting to investigate further. The following studies can therefore be subject for further work,

- Conducting experimental research on the 2.0mm steel plates. Applying the different loadings given in the parameter study and see if the deformation corresponds to the numerical results.
- Performing several experiments with the same driver pressure in order to validate the reliability of the shock tube facility.
- Implementing the blast load in Abaqus CAE by applying the Conventional Weapons Effects Program (ConWep) developed by the U.S Defence.
- Investigating the boundary conditions and study the effects of the numerical results.
- Establishing a pressure-impulse diagram through numerical analyses.
- Conducting the numerical research by employing other finite element programs, such as IMPETUS and LS-DYNA. Comparing the numerical results obtained from Abaqus CAE with the other programs.



# References

- [1] K. Spranghers, I. Vasilakos, D. Lecompte, H. Sol, and J. Vantomme. Numerical simulation and experimental validation of the dynamic response of aluminum plates under free air explosions. *International Journal of Impact Engineering*, 54:83–95, 2012.
- [2] J. Donea, A. Huerta, J.-Ph. Ponthot, and A. Rodriguez-Ferran. *Arbitrary Lagrangian-Eulerian Methods*, volume 1. John Wiley & Sons, Ltd., 2004.
- [3] T. Børvik, A.G. Hanssen, M. Langseth, and L. Olovsson. Response of structures to planar blast loads—A finite element engineering approach. *Computers & Structures*, 87(9):507–520, 2009.
- [4] S.B. Menkes and H.J. Opat. Broken beams. *Experimental Mechanics*, 13(11):480–486, 1973.
- [5] R.G. Teeling-Smith and G.N. Nurick. The deformation and tearing of thin circular plates subjected to impulsive loads. *International Journal of Impact Engineering*, 11:77–91, 1991.
- [6] M.D. Olson, G.N. Nurick, and J.R. Fagnan. Deformation and rupture of blast loaded square plates— Predictions and experiments. *International Journal of Impact Engineering*, 13:279–291, 1993.
- [7] G.N. Nurick and G.C. Shave. The deformation and tearing of thin square plates subjected to impulsive loads - An experimental study. *International Journal of Impact Engineering*, 18:99–116, 1996.

- [8] G.N. Nurick and J.B. Martin. Deformation of thin plates subjected to impulsive loading - A review, Part ii: Experimental studies. *International Journal of Impact Engineering*, 8:159–170, 1989.
- [9] R.B. Schubak, M.D. Olson, and D.L. Anderson. Rigid-plastic modelling of blast-loaded stiffened plates - Part i: One-way stiffened plates. *International Journal of Impact Engineering*, 35:289–306, 1993.
- [10] R.B. Schubak, M.D. Olson, and D.L. Anderson. Rigid-plastic modelling of blast-loaded stiffened plates - Part ii: Two-way stiffened plates. *International Journal of Impact Engineering*, 35:307–324, 1993.
- [11] G.K. Schleyer, S.S. Hsu, M.D. White, and R.S. Birch. Pulse pressure loading of clamped mild steel plates. *International Journal of Impact Engineering*, 28:223–247, 2002.
- [12] G.N. Nurick, M.D. Olson, J.R. Fagnan, and A. Levin. Deformation and tearing of blast-loaded stiffened square plates. *International Journal of Impact Engineering*, 16:273–291, 1995.
- [13] C.K.S. Yuen and G.N. Nurick. Experimental and numerical studies on the response of quadrangular stiffened plates. Part i: Subjected to uniform blast load. *International Journal of Impact Engineering*, 31:55–83, 2005.
- [14] G.N. Nurick and T. Wierzbicki. Large deformations of thin plates under localised impulsive loading. *International Journal of Impact Engineering*, 18:899–918, 1996.
- [15] K.G. Rakvåg, N.J. Underwood, G.K. Schleyer, T. Børvik, and O.S. Hopperstad. Transient pressure loading of clamped metallic plates with pre-formed holes. *International Journal of Impact Engineering*, 53:44–55, 2012.
- [16] A.C. Jacinto, R.D. Ambrosini, and R.F. Danesi. Experimental and computational analysis of plates under air blast loading. *International Journal of Impact Engineering*, 25:927–947, 2001.
- [17] A. Alia and M. Souli. High explosive simulation using multi-material formulations. *Applied Thermal Engineering*, 26:1032–1042, 2005.

- 
- [18] L. Olovsson, A.G. Hanssen, T. Børvik, and M. Langseth. A particle-based approach to close-range blast loading. *European Journal of Mechanics-A/Solids*, 29:1–6, 2009.
- [19] T. Børvik, L. Olovsson, A.G. Hanssen, K.P. Dharmasena, H. Hansson, and H.N.G. Wadley. A discrete particle approach to simulate the combined effect of blast and sand impact loading of steel plates. *Journal of the Mechanics and Physics of Solids*, 59:940–958, 2011.
- [20] P.O.K. Krehl. *History of Shock Waves, Explosions and Impact*. Springer, 2009.
- [21] N.A. Fomin. 110 years of experiments on shock tubes. 83(6), 2010.
- [22] Q. Li, D. Liu, D. Templeton, and B. Raju. A shock tube-based facility for impact testing. 2007.
- [23] W. Tsang and A. Lifshitz. Shock tube techniques in chemical kinetics. 1990.
- [24] R.K. Hanson, D.F. Davidson, D. Haylett, A. Farooq, S. Vasu, and S. Ranganath. Shock tube/laser diagnostics for fuel and surrogate kinetics. pages 25–28, 2008.
- [25] R.K. Hanson and D.F. Chang, A.Y. and Davidson. Modern shock tube methods for chemical studies in high temperature gases. 1988.
- [26] S. Downes, A. Knott, and I. Robinson. Towards a shock tube method for the dynamic calibration of pressure sensors. 2014.
- [27] N. Ray, G. Jagadeesh, and S. Suwas. Response of shock wave deformation in AA5086 aluminum alloy. *Materials Science and Engineering: A*, 622:219–227, 2015.
- [28] L.T. Zaczek, K.Y. Lam, D.F. Davidson, and R.K. Hanson. A shock tube study of  $\text{CH}_3\text{OH} + \text{OH} \rightarrow \text{Products}$  using oh laser absorption. *Proceedings of the Combustion Institute*, 35(1):377–384, 2015.
- [29] S. Li, D.F. Davidson, and R.K. Hanson. Shock tube study of dimethylamine oxidation. *International Journal of Chemical Kinetics*, 47(1):19–26, 2015.
- [30] A.J. Newman, S.H. Hayes, A.S. Rao, B.L. Allman, S. Manohar, D. Ding, D. Stolzberg, E. Lobarinas, J.C. Mollendorf, and R. Salvi. Low-cost blast wave generator for studies of hearing loss and brain injury: Blast wave effects in closed spaces. *Journal of neuroscience methods*, 2015.

- [31] M. Busquet, P. Barroso, T. Melse, and D. Bauduin. Miniature shock tube for laser driven shocks. 2010.
- [32] W.E. Baker, P.A. Cox, P.S. Westine, Kulesz J.J., and R.A. Strechlow. *Explosion Hazards and Evaluation*. Elsevier, 1983.
- [33] P.S. Bulson. *Explosive Loading of Engineering Structures*. E & FN SPON, 1997.
- [34] H. Draganić and V. Sigmund. Blast loading on structures. 2012.
- [35] P.H. Smith and J.G. Hetherington. *Blast and Ballistic Loading of Structures*. Butterworth Heinemann, 1994.
- [36] D. Bjerketvedt, J.R. Bakke, and K. van Wingerden. *Gas explosion handbook*. Gex-Con, 1993.
- [37] J.D. Anderson. *Fundamentals of Aerodynamics (In SI Units)*. McGraw-Hill Higher Education, 2013.
- [38] T. Krauthammer. *Modern Protective Structures*. CRC Press; 1st edition, 2008.
- [39] W.E. Baker. *Explosions in Air*. University of Texas press, Austin and London, 1973.
- [40] W. Wilkinson, D. Cormie, and M. Arkininstall. Calculation of blast loads for design against terrorism. 166:132–139, 2013.
- [41] Joly P. Kaber S.M. Postel M. Danaila, I. *Gas Dynamics: The Riemann Problem and Discontinuous Solutions: Application to the Shock Tube Problem*. Springer, 2007.
- [42] C.E. Needham. *Blast Wave Propagation*. Springer, 2010.
- [43] H.J. Davis and H.D. Curchack. Shock tube techniques and instrumentation. *U.S. Army Material Command*, 45(1), 1969.
- [44] J.K. Wright. *SHOCK TUBES*. Structural Impact Laboratory, 1961.
- [45] G.N. Nurick, M.D. Olson, J.R. Fagnan, and A. Levin. Deformation and tearing of blast-loaded stiffened square plates. *International Journal of Impact Engineering*, 16(2):273–291, 1995.

- 
- [46] W.Q. Shen and N. Jones. Dynamic response and failure of fully clamped circular plates under impulsive loading. *International journal of impact engineering*, 13(2):259–278, 1993.
- [47] G.N. Nurick and G.C. Shave. The deformation and tearing of thin square plates subjected to impulsive loads—an experimental study. *International Journal of Impact Engineering*, 18(1):99–116, 1996.
- [48] G.N. Nurick, M.E. Gelman, and N.S. Marshall. Tearing of blast loaded plates with clamped boundary conditions. *International Journal of Impact Engineering*, 18(7):803–827, 1996.
- [49] W.F. Hosford and R.M. Caddell. *Metal Forming - Mechanics and Metallurgy*. Prentice-Hall, 1993.
- [50] O.S. Hopperstad. NTNU internal report: Formability of aluminum alloys. *Structural Impact Laboratory (SIMLab), Department of Structural Engineering, NTNU*, 2015.
- [51] O.S. Hopperstad. Lecture notes plasticity theory: Phenomenology of plastic deformations. 2003.
- [52] O.S. Hopperstad and T. Børvik. Lecture notes, Material mechanics part 1. 2013.
- [53] A. Kane, T. Børvik, T. Berstad, A. Benallal, and O.S. Hopperstad. Failure criteria with unilateral conditions for simulation of plate perforation. *European Journal of Mechanics A/Solids*, 30:468–476, 2011.
- [54] T. Børvik, O.S. Hopperstad, T. Berstad, and M. Langseth. A computational model of viscoplasticity and ductile damage for impact and penetration. *European Journal of Mechanics - A/Solids*, 20:685–712, 2001.
- [55] N. McCormick and J. Lord. Digital image correlation. *Materials today*, 13(12):52–54, 2010.
- [56] E. Fagerholt. *Field Measurements in Mechanical Testing Using Close-range Photogrammetry and Digital Image Analysis*. Doctoral thesis at the Norwegian University of Science and Technology, 2012.

- [57] M.A. Sutton, J.H. Yan, V. Tiwari, H.W. Schreier, and J.J. Orteu. The effect of out-of-plane motion on 2D and 3D digital image correlation measurements. *Optics and Lasers Engineering*, 46:746–757, 2008.
- [58] X. Chen, N. Xu, L. Yang, and D. Xiang. High temperature displacement and strain measurement using a monochromatic light illuminated stereo digital image correlation system. *Measurement Science and Technology*, 23(12):125603, 2012.
- [59] Docol high strength steel, February. URL: <http://www.ssab.com/en/Brands/Doco11/Products/Doco1-600-DL/> [cited:09.02.15].
- [60] Aluminium alloy - commercial alloy-1050A-H14 sheet, December 2013. URL: [http://www.aalco.co.uk/datasheets/Aluminium-Alloy-1050A-H14-Sheet\\_57.ashx](http://www.aalco.co.uk/datasheets/Aluminium-Alloy-1050A-H14-Sheet_57.ashx) [cited:15.02.15].
- [61] Materials science and engineering, 2010. URL: <http://aluminium.matter.org.uk> [cited:15.02.15].
- [62] I. Assakaf. *Introduction to structural steel design*. Department of Civil and Environmental Engineering, University of Maryland, 2002.
- [63] R. Cobden. *Aluminium: Physical properties, characteristics and alloys*. 1994.
- [64] J.A. Zukas, T. Nicholas, H.F. Swift, L.B. Grezczuk, and D.R. Curran. *Impact dynamics*. 1992.
- [65] Curve fitting toolbox, 2015. URL: <http://se.mathworks.com/products/curvefitting/> [cited:10.02.15].
- [66] F. Grytten, T. Børvik, O.S. Hopperstad, and M. Langseth. Low velocity perforation of AA5083-H116 aluminium plates. *International Journal of Impact Engineering*, 36(4):597–610, 2009.
- [67] K.M. Mathisen. Lecture 9: Solution of the nonlinear dynamic equilibrium equation. 2014.
- [68] Structural Impact Laboratory. Simlab metal model (SMM)- theory, user's and example manual. 2015.



- 
- [69] Simlab toolbox, 2015. URL: <http://www.ntnu.edu/simlab> [cited:13.04.15].
- [70] Large strain isotropic hardening, 2014. URL: [http://folk.ntnu.no/davidmor/Tutorial\\_1.html](http://folk.ntnu.no/davidmor/Tutorial_1.html) [cited:03.03.15].
- [71] D. Morin. Personal communication. 2015.
- [72] K. Spranghers, I. Vasilakos, D. Lecompte, H. Sol, and J. Vantomme. Numerical simulation and experimental validation of the dynamic response of aluminum plates under free air explosions. *International Journal of Impact Engineering*, 54:83–95, 2013.
- [73] V. Aune, T. Børvik, and M. Langseth. Behaviour of plated structures subjected to blast loading. *EDP Sciences*, pages 1–6, 2015.
- [74] V. Aune, M. Langseth, and T. Børvik. Development of a shock tube facility to study blast loading on structures, work in progress. 2015.
- [75] Ideal gas law, May 2015. URL: <http://hyperphysics.phy-astr.gsu.edu/hbase/kinetic/idegas.html> [cited:21.05.15].
- [76] Specific heat ratio of air, May 2015. URL: [http://www.engineeringtoolbox.com/specific-heat-ratio-d\\_602.html](http://www.engineeringtoolbox.com/specific-heat-ratio-d_602.html) [cited:21.05.15].
- [77] J.M. Biggs. *Introduction to Structural Dynamics*. McGraw Hill, Inc., 1964.
- [78] W.E. Baker, P.A. Cox, P.S. Westine, J.J. Kulesz, and R.A. Strehlow. Explosion hazards and evaluation. *Fundamental studies in engineering*, 5:273–285, 1983.
- [79] ecorr 4.0 documentation, May 2015.
- [80] G.N. Nurick and J.B. Martin. Deformation of thin plates subjected to impulsive loading - A review, Part i: Theoretical considerations. *International Journal of Impact Engineering*, 8:171–186, 1989.
- [81] T. Børvik, M. Langseth, K.A. Malo, and O.S. Hopperstad. Empirical equations for ballistic penetration of metal plates. pages 1–19, 1998.

- [82] Practical yield line design, May 2015. URL: [http://www.ucviden.dk/student-portal/files/12633041/Practical\\_yield\\_design.pdf](http://www.ucviden.dk/student-portal/files/12633041/Practical_yield_design.pdf) [cited: 21.05.15].
- [83] J. Amdahl. Response of structures exposed to explosion. pages 1–13, 2005.
- [84] A.G. Hanssen, M. Langseth, and T. Børvik. p-i diagrammer for ekstruderte aluminiumsplater. pages 1–20, 2011.
- [85] J.K. Holmen, O.S. Hopperstad, and T. Børvik. Low-velocity impact on multi-layered dual-phase steel plates. *International Journal of Impact Engineering*, 78:161–177, 2014.
- [86] Abaqus Analysis User's Manual. Abaqus analysis user's manual (6.12). 2012.
- [87] U.S. Lindholm and G. R. Johnson. Strain-rate effects in metals at large shear strains. 29:61–79, 1983.
- [88] O.S. Hopperstad and O.G. Lademo. Classical FLD calculator in excel/visual basic. sintef report stf24 f04203. 2004.
- [89] W.F. Hosford and R.M. Caddell. *Metal Forming. Mechanics and Metallurgy*. Prentice-Hall, 1993.
- [90] R.D. Cook, D.S. Malkus, M.E. Plesha, and R.J. Witt. *Concepts and applications of finite element analysis*. John Wiley & Sons, Inc., 2002.
- [91] D.J. Benson. Explicit finite element methods for large deformation problems in solid mechanics. 2007.
- [92] K.M. Mathisen. Lecture 7: Solution of the dynamic equilibrium equations by explicit direct integration. 2014.
- [93] T. Belytschko, W.K. Liu, and B. Moran. *Nonlinear Finite Elements for Continua and Structures*. John Wiley & Sons Ltd., 2000.

# Appendix A

## Theory (Ch. 3)

This appendix includes essential theory that is not directly discussed in this thesis.

### A.1 Numerical Integration

The various numerical integration methods can be divided into explicit and implicit algorithms. In practical application, the main differences are related to stability and economy. It is possible to choose between an explicit method with low cost per time step but with many steps required, and an implicit method with higher cost per time step but fewer steps required [90]. The explicit algorithm is considered to be the best choice when simulating the blast scenario in Abaqus CAE.

#### A.1.1 Explicit Direct Integration

The explicit methods are conditionally stable and the numerical solution will blow up if the critical time step is exceeded. These methods are designed to efficiently solve large-scale, short-duration problems in nonlinear structural dynamics, e.g. strong shocks generated by explosives [91]. An advantage of the explicit algorithm is that the coefficient matrix of  $D_{n+1}$  is diagonalized leading to a low computational cost [92].

### A.1.2 Classical Central Difference

The expressions for velocity and acceleration are obtained by performing Taylor series expansions of  $D_{n+1}$  and  $D_{n-1}$  and combining the equations. All the terms that contain  $\Delta t$  higher than second order are discarded, subsequently  $D$  has second order accuracy [90].

$$\dot{D}_n = \frac{1}{2\Delta t} (D_{n+1} - D_{n-1}) \quad (\text{A.1}) \quad \ddot{D}_n = \frac{1}{\Delta t^2} (D_{n+1} - 2D_n + D_{n-1}) \quad (\text{A.2})$$

The two equations are substituted into the equilibrium equation for a non-linear multi degree of freedom system,

$$M\ddot{D}_n + C\dot{D}_n + R_n^{int} = R_n^{ext} \quad (\text{A.3})$$

The expression for the displacement are obtained,

$$D_{n+1} = [K^{eff}]^{-1} R_n^{eff} \quad (\text{A.4})$$

where,

$$K^{eff} = \left[ \frac{1}{\Delta t^2} M + \frac{1}{2\Delta t} C \right] \quad (\text{A.5})$$

$$R^{eff} = R_n^{ext} - R_n^{int} + \frac{2}{\Delta t^2} M D_n - \left[ \frac{1}{\Delta t^2} M - \frac{1}{2\Delta t} C \right] D_{n-1} \quad (\text{A.6})$$

Note that if linear conditions prevail,  $R_n^{int} = K D_n$ .

By studying Equation (A.5), we do certain observations. Unless the mass  $M$  and damping  $C$  matrices are diagonal, it is necessary to establish and factorize the effective stiffness  $K^{eff}$  in order to obtain displacements  $D_{n+1}$ . If lumped mass matrices are employed, and the damping is either zero or corresponds to mass-proportional damping  $C = \alpha M$ , the displacements  $D_{n+1}$  may be computed efficiently. Since mass-proportional

Rayleigh damping damps lower modes mainly, the dynamic response will contain high-frequency numerical noise which is undesirable. To damp out the higher-frequency noise, it may be desirable to include stiffness-proportional damping  $C = \beta K$ . This leads to a non-diagonal effective stiffness matrix and the solution of an equation system is required. Since it is necessary to solve an equation system for each time step, the computational cost increases [92].

### A.1.3 Half-Step Central Difference

The half-step method is the preferred form of the central difference. It is established by lagging the velocity half a time step [90],

$$\dot{D}_{n-\frac{1}{2}} = \frac{1}{\Delta t} [D_n - D_{n-1}] \quad (\text{A.7}) \quad \dot{D}_{n+\frac{1}{2}} = \frac{1}{\Delta t} [D_{n+1} - D_n] \quad (\text{A.8})$$

The acceleration is calculated by the expression below,

$$\ddot{D}_n = \frac{1}{\Delta t} [\dot{D}_{n+\frac{1}{2}} - \dot{D}_{n-\frac{1}{2}}] = \frac{1}{\Delta t^2} [D_{n+1} - 2D_n + D_{n-1}] \quad (\text{A.9})$$

The equation of motion is rewritten with the velocity lagging half a time step. Equation (A.3) becomes,

$$M\ddot{D}_n + C\dot{D}_{n-\frac{1}{2}} + R_n^{int} = R_n^{ext} \quad (\text{A.10})$$

Repeating the same procedure as for the conventional central difference, we get the expressions for the effective stiffness  $K^{eff}$  and force  $R^{eff}$ ,

$$K^{eff} = \frac{1}{\Delta t^2} M \quad (\text{A.11})$$

$$R^{eff} = R_n^{ext} - R_n^{int} + \frac{1}{\Delta t^2} M [D_n + \Delta t \dot{D}_{n-\frac{1}{2}}] - C \dot{D}_{n-\frac{1}{2}} \quad (\text{A.12})$$

Since the effective stiffness does not contain any terms dependent of the stiffness  $K$ , the half-step central difference has a reduced cost per time step. However, by introducing

lagging of the velocity the accuracy decreases from second to first order.

### A.1.4 Stability of Explicit Direct Integration

Explicit integration methods are conditionally stable, which means that the solution is bounded only when the time increment  $\Delta t$  is less than the stable time increment  $\Delta t_{cr}$ . If  $\Delta t > \Delta t_{cr}$ , the solution is no longer stable. For linear problems, oscillations will occur in the response history and the solution grows without limits. Numerical instability in nonlinear problems are harder to detect because the solution may seem reasonable despite being in error by 10-100 %. To warn of possible numerical instability, an energy balance check should be performed on nonlinear problems.

In general form, the stability criterion is dependent on the damping ratio  $\xi_i$ ,

$$\Delta t_{cr} \leq \min \left[ \frac{2}{\omega_i} \left( \sqrt{1 - \xi_i^2} - \xi_i \right) \right] \quad (\text{A.13})$$

Where  $i$  is the mode number and  $\xi_i$  the damping ratio in that mode. If the damping is small for all modes, the limit is determined from the highest natural frequency.

If there is no damping in the material, the expression abbreviates to,

$$\Delta t_{cr} \leq \frac{2}{\omega_{max}} \quad (\text{A.14})$$

where  $\omega_{max}$  is the maximum frequency.

For a linear, elastic material, the stable time increment can be computed from the dilatational wave speed  $c_d$ ,

$$\Delta t_{cr} = \frac{L^e}{c_d} \quad (\text{A.15}) \quad c_d = \sqrt{\frac{E}{\rho}} \quad (\text{A.16})$$

where  $L^e$  is the characteristic length of the smallest element in the finite element model,  $E$  is Young's Modulus and  $\rho$  is the material density.

In addition to the mathematical descriptions above, there is also a physical interpretation of the critical time step.  $\Delta t$  must be small enough so that information does not

propagate more than the distance between adjacent nodes during a single time step [92].

Note that stability and accuracy is not the same. It is possible to choose a time step that will produce a stable, but inaccurate solution. The accuracy of the solution depends on the employed time step. It is observed that choosing a time increment that is slightly smaller than  $\Delta t_{cr}$  provides excellent accuracy [90].

## A.2 Finite Element Formulations

There are three different finite element formulations, the Lagrangian, the Eulerian and the Arbitrary Lagrangian-Eulerian (ALE) formulation. They are based on the same set of conservation laws. These equations must always be satisfied by physical systems. Considering thermodynamics, the following conservation laws apply,

- i. Conservation of mass
- ii. Conservation of linear momentum
- iii. Conservation of angular momentum
- iv. Conservation of energy

Since it is only the Lagrangian formulation that will be applied in this thesis, the reader is referred to the literature [93] for information about the other formulations. As seen in the Section A.2.2, the conservations laws are usually expressed as partial differential equations. The theory and kinematic relations in the following sections are taken from [93] unless stated otherwise.

### A.2.1 Preliminary Kinematics

In continuum mechanics it is important to separate between different configurations. The initial or undeformed configuration  $\Omega_0$ , is the domain of a body in the initial state. However, using the term undeformed configuration is an idealization since undeformed objects rarely exist in reality. When describing the motion and deformation of a body, the reference configuration is applied. Unless otherwise is specified, the initial configuration is used as the reference configuration. To describe the deformed body, the domain of the current configuration  $\Omega$  is utilized. The boundaries of the domains of the initial and current configuration are denoted  $\Gamma_0$  and  $\Gamma$ , respectively.

Equation A.17 shows how the material and spatial coordinates relates through the motion of the material points by the application  $\phi$ . The function  $\phi(X, t)$  represents a mapping of the reference configuration into the current configuration at time  $t$ .



$$\boldsymbol{\phi}(\mathbf{X}, t) = (\mathbf{x}, t) \quad (\text{A.17})$$

The difference between the current and original position gives the displacement of a material point. This is written as follows,

$$\mathbf{u}(\mathbf{X}, t) = \boldsymbol{\phi}(\mathbf{X}, t) - \mathbf{X} \quad (\text{A.18})$$

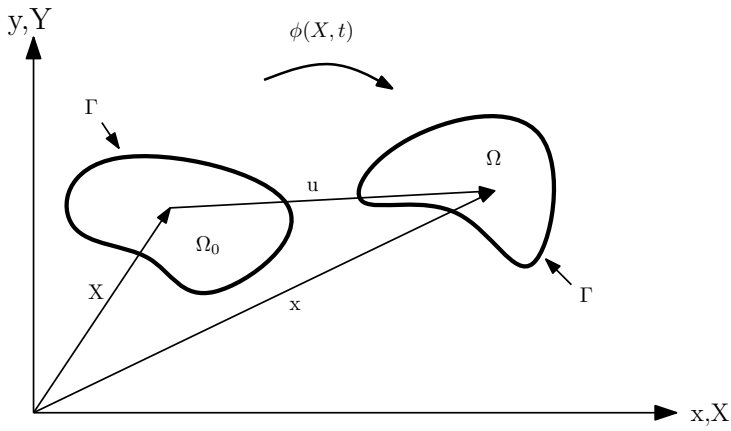


**Figure A.1:** Initial  $\Omega_0$  and current  $\Omega$  configuration[93].

The velocity  $\mathbf{v}(\mathbf{X}, t)$  is defined as the rate of change of the position vector for a material point. The velocity can be expressed as material time derivatives, meaning the time derivative with the  $\mathbf{X}$  held constant,

$$\mathbf{v}(\mathbf{X}, t) = \frac{\partial \boldsymbol{\phi}(\mathbf{X}, t)}{\partial t} = \frac{\partial \mathbf{u}(\mathbf{X}, t)}{\partial t} \equiv \dot{\mathbf{u}} \quad (\text{A.19})$$

The acceleration is the time derivative of the velocity, representing the rate of change of velocity of a material point,

$$\mathbf{a}(\mathbf{X}, t) = \frac{\partial \mathbf{v}(\mathbf{X}, t)}{\partial t} = \frac{\partial \dot{\mathbf{u}}(\mathbf{X}, t)}{\partial t} \equiv \dot{\mathbf{v}} \quad (\text{A.20})$$

To describe the deformation and the measure of strain, a deformation gradient is necessary. It is defined by,

$$F_{ij} = \frac{\partial \phi_i}{\partial X_j} \equiv \frac{\partial x_i}{\partial X_j} \quad \text{or} \quad \mathbf{F} \equiv \frac{\partial \boldsymbol{\phi}}{\partial \mathbf{X}} \equiv (\nabla_0 \boldsymbol{\phi})^T \quad (\text{A.21})$$

where  $\mathbf{F}$  is the Jacobian matrix of the motion  $\boldsymbol{\phi}(\mathbf{X}, t)$  and  $\nabla_0$  is the left gradient with respect to the material coordinates.

The Lagrangian formulation can be used when describing the deformation and response of a continuum. The approach is explained in the next section.

## A.2.2 Lagrangian Formulation

The Lagrangian approach is based on a material description. From a computation viewpoint, the grid follows the motion of the continuum. This leads to grid nodes that are constantly connected to the same material points. Figure A.2 illustrates how the Lagrangian meshes deforms with the material.

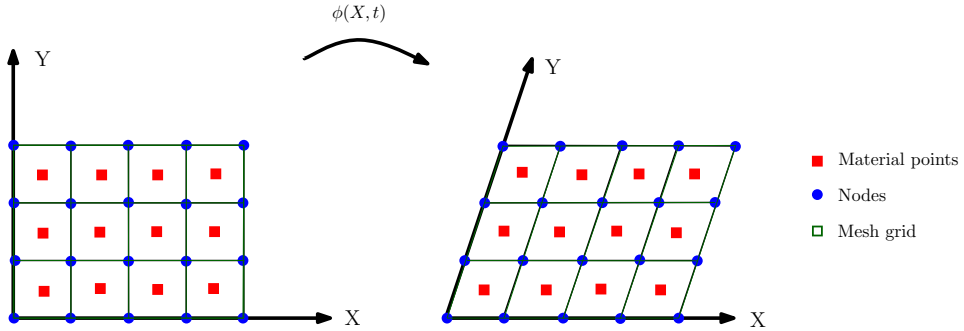


*Figure A.2: The Lagrangian formulation[93].*

The Lagrangian approach is preferable for solid and structural mechanics problems. This is reasoned in how Lagrangian meshes handle complicated boundaries. Another advantage is that history-dependent materials can be treated accurately due to the ability of Lagrangian meshes to follow material points. One drawback with this approach is that since the material points remain coincident with the mesh points, the elements will deform with the material. This entails a severely distorted Lagrangian mesh. Since the element accuracy is related to the level of distortion, the magnitude of deformation that can be simulated with a Lagrangian mesh is limited.

There are three different Lagrangian formulations,

- Total Lagrangian (TL)
- Updated Lagrangian (UL)
- Co-Rotational (CR)

In the TL and UL formulations, the strain and stress measures are referred to the initial and deformed configuration. In the CR formulation, a local reference frame is attached to each element and translates and rotates with the element as a rigid body. The rest of

the derivations in this section will be based on the Total Lagrangian formulation.

In the Lagrangian formulation the independent variables are the material coordinates  $X_i$  and the time  $t$ , while the dependent variables are the initial density  $\rho_0$ , the displacement  $\mathbf{u}(\mathbf{X}, t)$  and the Lagrangian measures of stress and strain. The conservation equations for this approach are,

Mass conservation

$$\rho(\mathbf{X}, t)J(\mathbf{X}, t) = \rho_0(\mathbf{X}) \quad \text{or} \quad \rho J = \rho_0 \quad (\text{A.22})$$

Linear momentum conservation

$$\rho_0 \frac{\partial \mathbf{v}(\mathbf{X}, t)}{\partial t} = \nabla_0 \mathbf{P} + \rho_0 \mathbf{b} \quad \text{or} \quad \rho_0 \frac{\partial v_i(\mathbf{X}, t)}{\partial t} = \frac{\partial P_{ij}}{\partial X_j} + \rho_0 b_i \quad (\text{A.23})$$

Angular momentum conservation

$$\mathbf{F}\mathbf{P} = \mathbf{P}^T \mathbf{F}^T, \quad F_{ij}P_{kj} = P_{ik}^T F_{kj}^T = F_{jk}P_{ki}, \quad \mathbf{S} = \mathbf{S}^T \quad (\text{A.24})$$

Energy conservation

$$\rho_0 \dot{w}^{int} = \rho_0 \frac{\partial w^{int}(\mathbf{X}, t)}{\partial t} = \dot{\mathbf{F}}^T : \mathbf{P} - \nabla_0 \tilde{\mathbf{q}} + \rho_0 s \quad (\text{A.25})$$

where,

- $\rho$  is the current density
- $\rho_0$  is the initial density
- $s$  is the specific heat term
- $w$  is the hyperelastic potential on reference configurations
- $J$  is determinant of Jacobian between spatial and material coordinates,  $J = \det[\partial x_i / \partial X_j]$
- $\mathbf{P}$  is the nominal stress tensor
- $\mathbf{b}$  is the body force vector
- $\mathbf{F}$  is the deformation gradient,  $F_{ij} = \partial x_i / \partial X_j$
- $\mathbf{S}$  is the second Piola-Kirchhoff stress tensor
- $\mathbf{q}$  is the collection of internal variables in the constitutive model

# **Appendix B**

## **Material Information (Ch. 4)**

### **B.1 Material cards from the supplier**

APPENDIX B. MATERIAL INFORMATION (CH. 4)

**SSAB** Lasterortteckning / VIII sheet ocn / and  
Provningstyg / Test certificate

Sida/  
Page  
1

Intygstyp/Type of certificate  
EN 10204-3.1 Kontrollintyg

Stålsort/Steel grade D00DL 600 DL A		Faktura nr/invoice No. 2640048		Vår/Our order 833891	
Standard, specifikation enligt beställning/Standard specification according to the order				Köparens/Buyer's order (Date) 14120 4027535	
Produkt/Product Kallv konti glödg format				Köpare/Buyer E. A. SMITH AS 70086	
				POSTBOKS 9410 SLUPPEN NO-7493 TRONDHEIM NORGE	

Pos/ Item	Charge/Cast	*p	*p	Provnr/Test No.	Dimension			Kg/Kilos	St/Pieces	*LEV TILLST
1	25-8861	LD	S	16613935	2000 X	1250	.80	59	4	

Chargeanalysis/Ladle Analysis, %

Charge/Cast	*Ec	C	Si	Mn	P	S	N	Cr	Ni	Cu	Mo	Al	Nb	V	Ti	B	Desox
25-8861	37	100	28	155	12	3	4	2	3	0	0	41	0	1	0	3	SI+AL


Provningresultat/Test result

Prov nr Test No	*L	RP02 N/mm2	RM N/mm2	A% A80	A% mm	x 10 <sup>-2</sup>	x 10 <sup>-3</sup>	x 10 <sup>-2</sup>	x 10 <sup>-3</sup>	x 10 <sup>-2</sup>	x 10 <sup>-4</sup>
1661393	T	299	677	25							

ANM/NOTES	ANM/NOTES	ANM/NOTES
-----------	-----------	-----------

14-001 EDITA ROBERGS FALLIN 9357 MS

Vi intygar härmed att materialet är tillverkat och provat i överensstämmelse med vår ovan angivna order.  
We hereby certify that the material has



Tillverkarens  
märke/  
Mark of the

BORLÅNGE 14-12-16

*Oliver Kvarn*

AVD MATERIALPROVNING

Inspektör's stamp

Figure B.1: Material card of steel 0.8mm.

**SSAB**

Sida 1 (1)

SSAB EMEA AB, SE-781 84 BORLÄNGE, Sweden

Kontrollintyg 3.1 EN 10 204 - 3.1		A02	Utfärdande avdelning Kvalitetsavdelningen		A05	Köparens ordernr 4027535		A07	Vårt ordernr 623891-2		A08	Fakturanr 2640048		A19	Intygns och datum 15184962 2014-12-16		A03						
Köpare E.A. SMITH AS POSTBOKS 9410 SLUPPEN NO-7489 TRONDHEIM NORGE		A11	70086		Produkt Kallv konti glödg format			B01	Märkning Tillverkare, MATERIALID			B06	Standard Stålsort		B02 DOCOL 600 DL A M								
Antal		B08	Dimensioner (mm)		B09-B11		Vikt [kg]		B12	Lev. tillst.		B04		Referens nummer									
1			T 2 B 1250 L 2000				155																
MATERIALID 29-2993-16626411					A06	Kundens märke			B15														
E.A. SMITH AS POSTBOKS 9410 SLUPPEN NO-7489 TRONDHEIM NORGE																							
Kemisk sammansättning														C71-C92		Carbon eqivalent etc.		C93-C99					
Charge		C	Si	Mn	P	S	Cr	Ni	Mo	V	Ti	Cu	Al	Nb	B	N	Colv	Colv = C + Mn/6 + (Ni + Cu)/15 + (Cr + Mo + V)/5					
29-2993		.103	.31	1.51	.010	.001	.02	.03	.00	.01	.00	.01	.045	.000	.0003	.003	.36						
Provtyp		C04	Verkskod		C00	Provstavs position		C01	Riktning		C02	Behandling		B05	Provstavs typ		C10	Temp [gr C]		C03	Proverresultat		
Dragnavn			BJC395			Topp			Tvärs			Leverans- tillstånd			Platt 250x20						C11 Rp0.2 [MPa] 334		
																					C12 Rm [MPa] 664		
																					C13 AB0 [%] 29.5		
Produktionstid: 2014-10-23																							

Härmed intygas att ovannämnt material		Z02			Intyget är framställt elektroniskt och gäller utan signering		Z01			A22			A04
upplysifier ordrens föringdar.				Material Testing: L. Smadhv M Eriksson/ L. Söderqvist								www.docol.com	

Figure B.2: Material card of steel 2.0mm.



APPENDIX B. MATERIAL INFORMATION (CH. 4)

**ADITYA BIRLA HINDALCO INDUSTRIES LIMITED**  
 Aluma Centre, 1st Floor, Kankarbagich, Cross, Sector-1, Gurgaon (Haryana)  
 India - 122002  
 Fax: +91-122-44917250, Email: export.hindalco@alcoa.com  
 Regd. Office: Convent, Bherm, Dr. Ambedkar Road, Worli,  
 Mumbai - 400 025, INDIA.

CERT. 3.1 B DIN EN 10204  
 ASTRUP AS POSITROSKA HALLINGSTIA, 2815 OSLO, NORWAY  
 ALUMINIUM PLAIN SHEET IN T030 H14 TEMPER WILL FINISH CONFORMING TO ENAW STANDARDS  
 P.O. NO. 115833 PRG0201502

THE TEST RESULTS OF THE SAMPLES DRAWN FROM THE ABOVE LOT AND TESTED IN OUR LABORATORY ARE AS FOLLOWS:

Batch No./ Temp	Alloy	Size (mm)	QY (N/T)	Call No.	Card No./Sheet No	%Si	%Fe	%Mn	%Mg	%Cu	%Zn	%MgZn	%Zr	%Ti	%Pb	%Al	Mechanical Properties	Weight	Brand Test	UTS (N/mm <sup>2</sup> )	PS (N/mm <sup>2</sup> )
AA1050	H14	3000 X 1500 X 0.80	1108	ACT1150/2	1431050-2E-01/4	1	2.20	0.02	0.02	0.01	0.02	0.02	0.02	0.02	0	99.92	12	0.2	148.2	13.02	
AA1050	H14	2000 X 1250 X 0.80	1108	ACT1150/2	1431050-2E-01/4	1	2.20	0.02	0.02	0.01	0.02	0.02	0.02	0.02	0	99.92	7	0.2	148.2	13.02	
AA1050	H14	2000 X 1250 X 0.80	1108	ACT1150/2	1431050-2E-01/4	1	2.20	0.02	0.02	0.01	0.02	0.02	0.02	0.02	0	99.92	7	0.2	148.2	13.02	
AA1050	H14	2000 X 1250 X 0.80	1108	ACT1150/2	1431050-2E-01/4	1	2.20	0.02	0.02	0.01	0.02	0.02	0.02	0.02	0	99.92	7	0.2	148.2	13.02	
AA1050	H14	2000 X 1250 X 0.80	1108	ACT1150/2	1431050-2E-01/4	1	2.20	0.02	0.02	0.01	0.02	0.02	0.02	0.02	0	99.92	7	0.2	148.2	13.02	
AA1050	H14	2000 X 1250 X 0.80	1108	ACT1150/2	1431050-2E-01/4	1	2.20	0.02	0.02	0.01	0.02	0.02	0.02	0.02	0	99.92	7	0.2	148.2	13.02	
AA1050	H14	2000 X 1250 X 0.80	1108	ACT1150/2	1431050-2E-01/4	1	2.20	0.02	0.02	0.01	0.02	0.02	0.02	0.02	0	99.92	7	0.2	148.2	13.02	
AA1050	H14	2000 X 1250 X 0.80	1108	ACT1150/2	1431050-2E-01/4	1	2.20	0.02	0.02	0.01	0.02	0.02	0.02	0.02	0	99.92	7	0.2	148.2	13.02	
AA1050	H14	2000 X 1250 X 0.80	1108	ACT1150/2	1431050-2E-01/4	1	2.20	0.02	0.02	0.01	0.02	0.02	0.02	0.02	0	99.92	7	0.2	148.2	13.02	
AA1050	H14	2000 X 1250 X 0.80	1108	ACT1150/2	1431050-2E-01/4	1	2.20	0.02	0.02	0.01	0.02	0.02	0.02	0.02	0	99.92	7	0.2	148.2	13.02	
AA1050	H14	2000 X 1250 X 0.80	1108	ACT1150/2	1431050-2E-01/4	1	2.20	0.02	0.02	0.01	0.02	0.02	0.02	0.02	0	99.92	7	0.2	148.2	13.02	
AA1050	H14	2000 X 1250 X 0.80	1108	ACT1150/2	1431050-2E-01/4	1	2.20	0.02	0.02	0.01	0.02	0.02	0.02	0.02	0	99.92	7	0.2	148.2	13.02	
AA1050	H14	2000 X 1250 X 0.80	1108	ACT1150/2	1431050-2E-01/4	1	2.20	0.02	0.02	0.01	0.02	0.02	0.02	0.02	0	99.92	7	0.2	148.2	13.02	
AA1050	H14	2000 X 1250 X 0.80	1108	ACT1150/2	1431050-2E-01/4	1	2.20	0.02	0.02	0.01	0.02	0.02	0.02	0.02	0	99.92	7	0.2	148.2	13.02	
AA1050	H14	2000 X 1250 X 0.80	1108	ACT1150/2	1431050-2E-01/4	1	2.20	0.02	0.02	0.01	0.02	0.02	0.02	0.02	0	99.92	7	0.2	148.2	13.02	
AA1050	H14	2000 X 1250 X 0.80	1108	ACT1150/2	1431050-2E-01/4	1	2.20	0.02	0.02	0.01	0.02	0.02	0.02	0.02	0	99.92	7	0.2	148.2	13.02	
AA1050	H14	2000 X 1250 X 0.80	1108	ACT1150/2	1431050-2E-01/4	1	2.20	0.02	0.02	0.01	0.02	0.02	0.02	0.02	0	99.92	7	0.2	148.2	13.02	
AA1050	H14	2000 X 1250 X 0.80	1108	ACT1150/2	1431050-2E-01/4	1	2.20	0.02	0.02	0.01	0.02	0.02	0.02	0.02	0	99.92	7	0.2	148.2	13.02	
AA1050	H14	2000 X 1250 X 0.80	1108	ACT1150/2	1431050-2E-01/4	1	2.20	0.02	0.02	0.01	0.02	0.02	0.02	0.02	0	99.92	7	0.2	148.2	13.02	
AA1050	H14	2000 X 1250 X 0.80	1108	ACT1150/2	1431050-2E-01/4	1	2.20	0.02	0.02	0.01	0.02	0.02	0.02	0.02	0	99.92	7	0.2	148.2	13.02	
AA1050	H14	2000 X 1250 X 0.80	1108	ACT1150/2	1431050-2E-01/4	1	2.20	0.02	0.02	0.01	0.02	0.02	0.02	0.02	0	99.92	7	0.2	148.2	13.02	
AA1050	H14	2000 X 1250 X 0.80	1108	ACT1150/2	1431050-2E-01/4	1	2.20	0.02	0.02	0.01	0.02	0.02	0.02	0.02	0	99.92	7	0.2	148.2	13.02	
AA1050	H14	2000 X 1250 X 0.80	1108	ACT1150/2	1431050-2E-01/4	1	2.20	0.02	0.02	0.01	0.02	0.02	0.02	0.02	0	99.92	7	0.2	148.2	13.02	
AA1050	H14	2000 X 1250 X 0.80	1108	ACT1150/2	1431050-2E-01/4	1	2.20	0.02	0.02	0.01	0.02	0.02	0.02	0.02	0	99.92	7	0.2	148.2	13.02	
AA1050	H14	2000 X 1250 X 0.80	1108	ACT1150/2	1431050-2E-01/4	1	2.20	0.02	0.02	0.01	0.02	0.02	0.02	0.02	0	99.92	7	0.2	148.2	13.02	
AA1050	H14	2000 X 1250 X 0.80	1108	ACT1150/2	1431050-2E-01/4	1	2.20	0.02	0.02	0.01	0.02	0.02	0.02	0.02	0	99.92	7	0.2	148.2	13.02	
AA1050	H14	2000 X 1250 X 0.80	1108	ACT1150/2	1431050-2E-01/4	1	2.20	0.02	0.02	0.01	0.02	0.02	0.02	0.02	0	99.92	7	0.2	148.2	13.02	
AA1050	H14	2000 X 1250 X 0.80	1108	ACT1150/2	1431050-2E-01/4	1	2.20	0.02	0.02	0.01	0.02	0.02	0.02	0.02	0	99.92	7	0.2	148.2	13.02	
AA1050	H14	2000 X 1250 X 0.80	1108	ACT1150/2	1431050-2E-01/4	1	2.20	0.02	0.02	0.01	0.02	0.02	0.02	0.02	0	99.92	7	0.2	148.2	13.02	
AA1050	H14	2000 X 1250 X 0.80	1108	ACT1150/2	1431050-2E-01/4	1	2.20	0.02	0.02	0.01	0.02	0.02	0.02	0.02	0	99.92	7	0.2	148.2	13.02	
AA1050	H14	2000 X 1250 X 0.80	1108	ACT1150/2	1431050-2E-01/4	1	2.20	0.02	0.02	0.01	0.02	0.02	0.02	0.02	0	99.92	7	0.2	148.2	13.02	
AA1050	H14	2000 X 1250 X 0.80	1108	ACT1150/2	1431050-2E-01/4	1	2.20	0.02	0.02	0.01	0.02	0.02	0.02	0.02	0	99.92	7	0.2	148.2	13.02	
AA1050	H14	2000 X 1250 X 0.80	1108	ACT1150/2	1431050-2E-01/4	1	2.20	0.02	0.02	0.01	0.02	0.02	0.02	0.02	0	99.92	7	0.2	148.2	13.02	
AA1050	H14	2000 X 1250 X 0.80	1108	ACT1150/2	1431050-2E-01/4	1	2.20	0.02	0.02	0.01	0.02	0.02	0.02	0.02	0	99.92	7	0.2	148.2	13.02	
AA1050	H14	2000 X 1250 X 0.80	1108	ACT1150/2	1431050-2E-01/4	1	2.20	0.02	0.02	0.01	0.02	0.02	0.02	0.02	0	99.92	7	0.2	148.2	13.02	
AA1050	H14	2000 X 1250 X 0.80	1108	ACT1150/2	1431050-2E-01/4	1	2.20	0.02	0.02	0.01	0.02	0.02	0.02	0.02	0	99.92	7	0.2	148.2	13.02	
AA1050	H14	2000 X 1250 X 0.80	1108	ACT1150/2	1431050-2E-01/4	1	2.20	0.02	0.02	0.01	0.02	0.02	0.02	0.02	0	99.92	7	0.2	148.2	13.02	
AA1050	H14	2000 X 1250 X 0.80	1108	ACT1150/2	1431050-2E-01/4	1	2.20	0.02	0.02	0.01	0.02	0.02	0.02	0.02	0	99.92	7	0.2	148.2	13.02	
AA1050	H14	2000 X 1250 X 0.80	1108	ACT1150/2	1431050-2E-01/4	1	2.20	0.02	0.02	0.01	0.02	0.02	0.02	0.02	0	99.92	7	0.2	148.2	13.02	
AA1050	H14	2000 X 1250 X 0.80	1108	ACT1150/2	1431050-2E-01/4	1	2.20	0.02	0.02	0.01	0.02	0.02	0.02	0.02	0	99.92	7	0.2	148.2	13.02	
AA1050	H14	2000 X 1250 X 0.80	1108	ACT1150/2	1431050-2E-01/4	1	2.20	0.02	0.02	0.01	0.02	0.02	0.02	0.02	0	99.92	7	0.2	148.2	13.02	
AA1050	H14	2000 X 1250 X 0.80	1108	ACT1150/2	1431050-2E-01/4	1	2.20	0.02	0.02	0.01	0.02	0.02	0.02	0.02	0	99.92	7	0.2	148.2	13.02	
AA1050	H14	2000 X 1250 X 0.80	1108	ACT1150/2	1431050-2E-01/4	1	2.20	0.02	0.02	0.01	0.02	0.02	0.02	0.02	0	99.92	7	0.2	148.2	13.02	
AA1050	H14	2000 X 1250 X 0.80	1108	ACT1150/2	1431050-2E-01/4	1	2.20	0.02	0.02	0.01	0.02	0.02	0.02	0.02	0	99.92	7	0.2	148.2	13.02	
AA1050	H14	2000 X 1250 X 0.80	1108	ACT1150/2	1431050-2E-01/4	1	2.20	0.02	0.02	0.01	0.02	0.02	0.02	0.02	0	99.92	7	0.2	148.2	13.02	
AA1050	H14	2000 X 1250 X 0.80	1108	ACT1150/2	1431050-2E-01/4	1	2.20	0.02	0.02	0.01	0.02	0.02	0.02	0.02	0	99.92	7	0.2	148.2	13.02	
AA1050	H14	2000 X 1250 X 0.80	1108	ACT1150/2	1431050-2E-01/4	1	2.20	0.02	0.02	0.01	0.02	0.02	0.02	0.02	0	99.92	7	0.2	148.2	13.02	
AA1050	H14	2000 X 1250 X 0.80	1108	ACT1150/2	1431050-2E-01/4	1	2.20	0.02	0.02	0.01	0.02	0.02	0.02	0.02	0	99.92	7	0.2	148.2	13.02	
AA1050	H14	2000 X 1250 X 0.80	1108	ACT1150/2	1431050-2E-01/4	1	2.20	0.02	0.02	0.01	0.02	0.02	0.02	0.02	0	99.92	7	0.2	148.2	13.02	
AA1050	H14	2000 X 1250 X 0.80	1108	ACT1150/2	1431050-2E-01/4	1	2.20	0.02	0.02	0.01	0.02	0.02	0.02	0.02							



**Hydro Aluminium  
Rolled Products**

NO 104701  
ASTRUP A.S  
HAAVARD MARTINSENS VEI 34  
0978 OSLO  
Norway

**Inspection Certificate no: KRM 101575 - 6**

According to EN 10204 - 3.1.

Date : 06/02/2014 Page : 1

Customer order no : 1166695  
Our order no : 531420-6  
Invoice no :  
Packing list no : KRM101575  
Product : 2.000 x 1250 x 2500  
Gross weight : 5947 Kg  
Net weight : 5767 Kg  
Customer part no :  
Alloy/temper : 105025 14  
Customer Spec. :

	Si	Fe	Cu	Mn	Mg	Zn	Ti	Al
Min								99.50
Max	0.25	0.40	0.05	0.05	0.05	0.07	0.05	
410855	0.06	0.32	0.001	0.002	0.001	0.006	0.009	99.61

**Mechanical properties**

	Rp0.2	Rm	Elong A50			Thick- ness			
Cust. Min	85	105	4			1.890			
Max		145				2.110			
Coil no. 410855	110	117	9			1.990			

Material Specification and Test Results  
Standard EN 485/515/573

Kristian Stray (sign.)  
Plant Metallurgist



Hydro Aluminium   
Rolled Products AS   
Karmøy Rolling Mill   
N-4265 HAVIK

Vat no: 975 934 578 MVA  
Tel: +47 52 85 40 00  
Fax: +47 52 85 43 50



**Figure B.4:** Material card of aluminium 2.0mm.

## B.2 Data from the Tension Test

### B.2.1 Initial Measurements of the Dog-Bone Specimen

*Table B.1: Geometry of Docol 600 DL steel.*

Test	Rolling Direction	Thickness [mm]	Width [mm]	Exstensometer
S08-01	0°	0.80	12.55	Yes
S08-02	0°	0.82	12.58	-
S08-03	0°	0.82	12.62	-
S08-04	45°	0.83	12.76	Yes
S08-05	45°	0.84	12.88	-
S08-06	45°	0.85	12.76	-
S08-07	90°	0.82	12.74	Yes
S08-08	90°	0.83	12.65	-
S08-09	90°	0.83	12.60	-
S20-01	0°	2.00	12.68	Yes
S20-02	0°	2.00	12.66	-
S20-03	0°	1.98	12.59	-
S20-04	45°	1.95	12.63	Yes
S20-05	45°	2.00	12.72	-
S20-06	45°	1.95	12.69	-
S20-07	90°	1.95	12.97	Yes
S20-08	90°	2.00	12.72	-
S20-09	90°	1.98	13.00	-

*Table B.2: Geometry of aluminium alloy EN AW-1050A-H14.*

Test	Rolling Direction	Thickness [mm]	Width [mm]	Exstensometer
A08-01	0°	0.79	12.50	Yes
A08-02	0°	0.77	12.43	-
A08-03	0°	0.75	12.45	-
A08-04	45°	0.76	12.46	Yes
A08-05	45°	0.74	12.47	-
A08-06	45°	0.77	12.48	-
A08-07	90°	0.74	12.50	Yes
A08-08	90°	0.74	12.52	-
A08-09	90°	0.75	12.48	-
A20-01	0°	1.98	12.54	-
A20-02	0°	2.02	12.56	Yes
A20-03	0°	2.00	12.62	-
A20-04	45°	1.98	12.55	Yes
A20-05	45°	2.00	12.54	-
A20-06	45°	2.00	12.55	-
A20-07	90°	2.01	12.52	Yes
A20-08	90°	2.02	12.54	-
A20-09	90°	2.00	12.49	-

### B.2.2 Verification of 2D-DIC

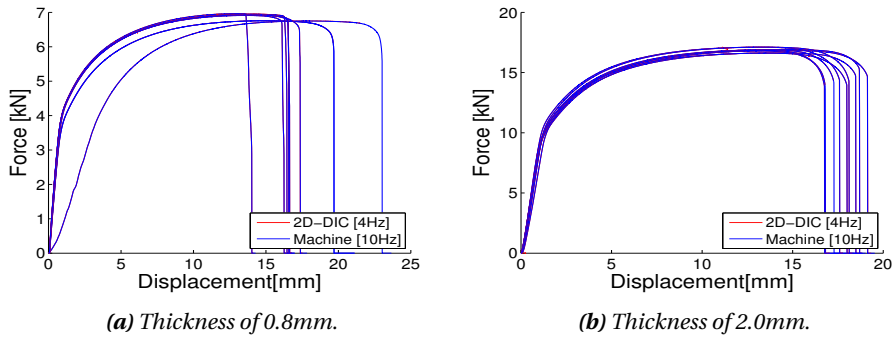


Figure B.5: Verification of the steel plates.

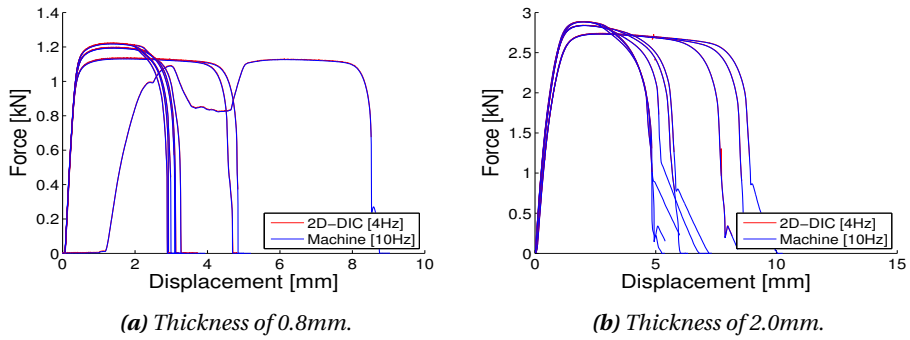


Figure B.6: Verification of the aluminium plates.

### B.2.3 Calibration of the Tension Test

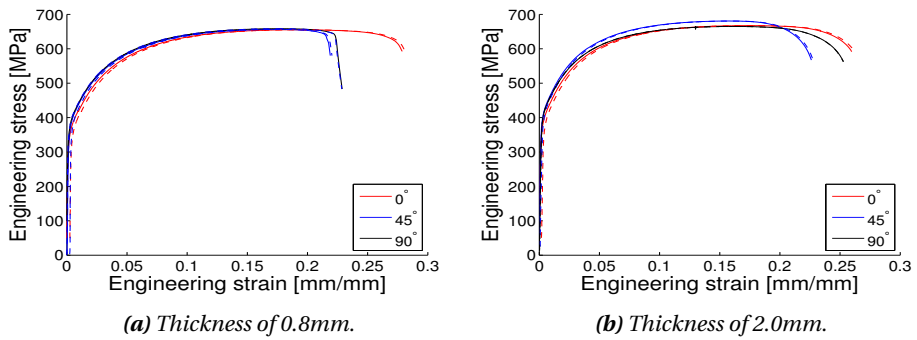


Figure B.7: Correction of the steel plates.

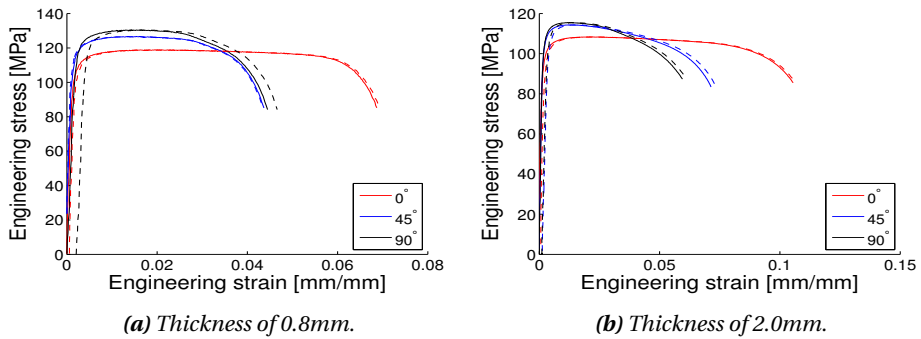
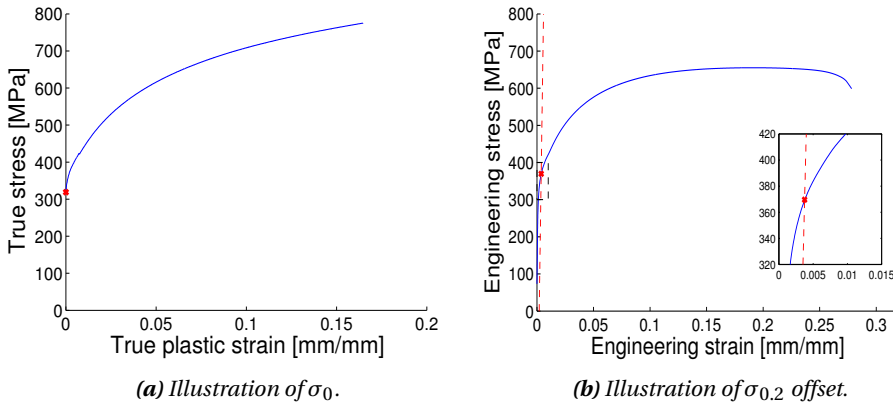


Figure B.8: Correction of the aluminium plates.



**Figure B.9:** Calibration of yield strength for a steel specimen.

### B.2.4 Parameters for the isotropic hardening models

**Table B.3:** Docol 600 DL steel.

Test	Voce rule					Power law		
	A [MPa]	$Q_1$ [MPa]	$Q_2$ [MPa]	$C_1$	$C_2$	A [MPa]	K [MPa]	n
S08-02	334.5	117.1	379.7	84.9	11.4	277.5	989.3	0.4
S08-04	185.0	223.1	385.2	973.6	16.3	183.2	970.7	0.3
S08-08	1.6e-06	380.3	411.4	16.2	1647.0	1.3	1072.0	0.2
S20-03	355.6	345.0	135.0	11.8	85.8	296.8	942.6	0.3
S20-06	379.7	116.2	339.8	99.0	13.5	324.9	946.5	0.4
S20-09	306.6	354.5	128.7	18.3	602.8	283.3	899.8	0.3

**Table B.4:** Aluminium alloy EN AW-1050-H14.

Test	Voce rule					Power law		
	A [MPa]	$Q_1$ [MPa]	$Q_2$ [MPa]	$C_1$	$C_2$	A [MPa]	K [MPa]	n
A08-02	97.6	13.2	10.6	1458.0	185.9	95.2	57.9	0.2
A08-04	110.9	8.4	10.6	143.1	1000.0	107.3	62.7	0.2
A08-09	5.8	107.4	18.6	6000.0	402.2	50.0	137.7	0.1
A20-03	86.8	8.5	16.5	103.3	993.6	83.6	58.7	0.2
A20-04	90.2	16.2	9.5	1689.0	275.9	86.7	74.9	0.2
A20-09	87.3	9.5	20.8	261.1	2000.0	81.1	74.1	0.2

# Appendix C

## Experimental Data (Ch.5)

### C.1 Membrane Capacity

The membrane capacity for the polyester Melinex is tested by SIMLab, and the various combinations and tolerance levels are shown below.

*Table C.1: Pressure tolerance of the diaphragms.*

Test nr. Thickness [mm]	1 [kPa]	2 [kPa]	3 [kPa]	4 [kPa]	5 [kPa]	Composition of membranes
0.125	156.2	158.3	160.5	158.7	160.5	1×0.125
0.190	213.6	210.0	209.4	207.2	207.8	1×0.190
0.250	301.0	293.6	296.9	290.5	292.1	1×0.250
0.250	314.3	303.0	315.0	303.7	311.6	2×0.125
0.315	364.0	363.8	362.3	363.9	364.1	0.125+0.190
0.380	411.6	413.2	411.7	411.0	411.7	2×0.190
0.440	492.0	499.9	504.6	498.4	495.6	0.190+0.250
0.500	439.7	431.5	434.3	428.2	434.3	1×0.500
0.500	606.7	589.9	591.4	585.0	593.3	2×0.250
0.690	648.5	654.6	652.5	638.1	669.6	0.190+0.500
0.750	719.3	705.6	720.5	720.8	717.8	0.250+0.500
0.100	888.0	862.5	866.7	861.5	863.7	2×0.500

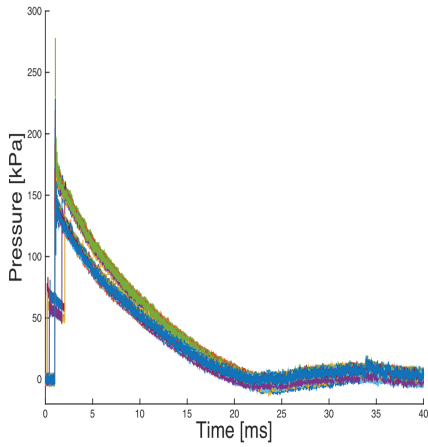
## C.2 Calibration of the pressure in the Shock Tube

*Table C.2: Membrane combinations for different driver pressures.*

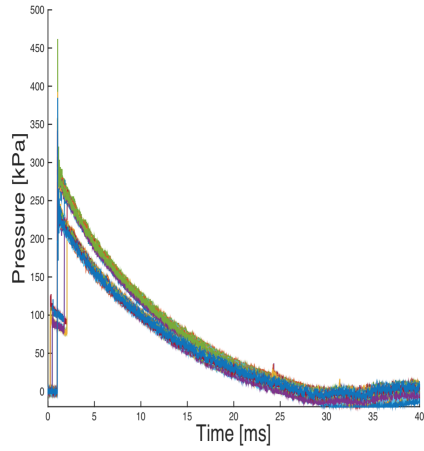
Driver pressure [kPa]	Membrane thickness [mm]	# chambers	# repetitions
500	0.25+0.25	2	3
1000	(0.25x2)+(0.25x2)	2	3
1500	(0.25+0.25) + (0.25+0.25) + (0.25+0.25)	3	3
2000	(0.25+0.5) + (0.25+0.5)+(0.25+0.5)	3	3
2500	(0.5x2) + (0.5x2) + (0.5x2)	3	3
3500	2x(0.25+0.5) + 2x(0.25+0.5) + 2x(0.25+0.5)	3	1
4000	2x(0.25+0.5) + 2x(0.25+0.5) + 2x(0.25+0.5)	3	1



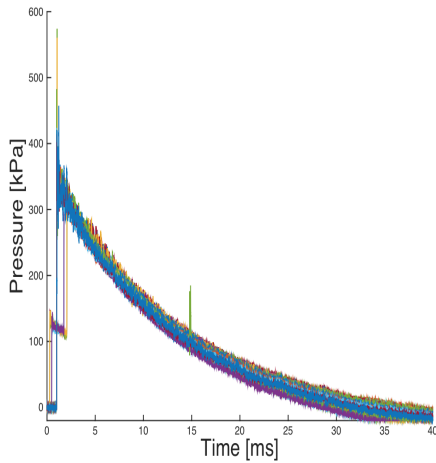
### C.2.1 Pressure Distribution on the Rigid Plate



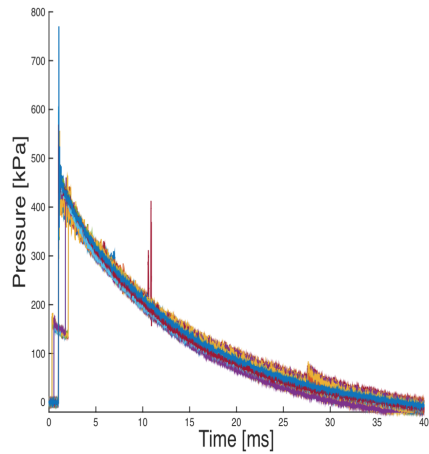
(a) Intended driver pressure of 500 kPa



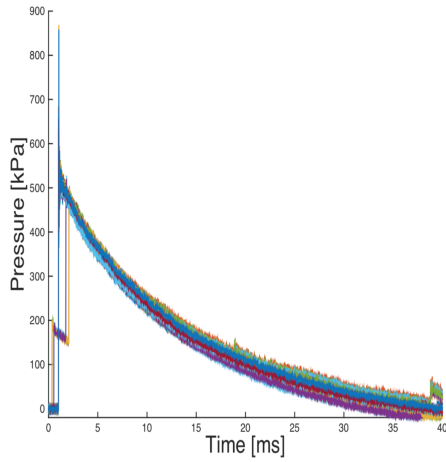
(b) Intended driver pressure of 1000 kPa



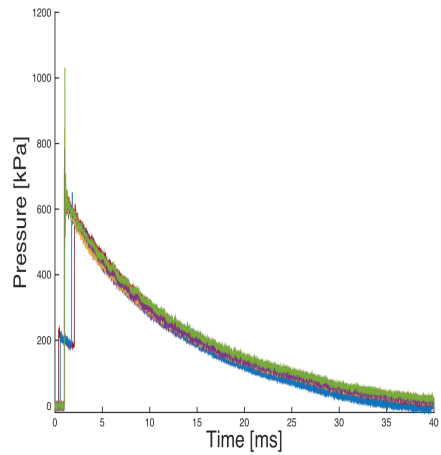
(c) Intended driver pressure of 1500 kPa



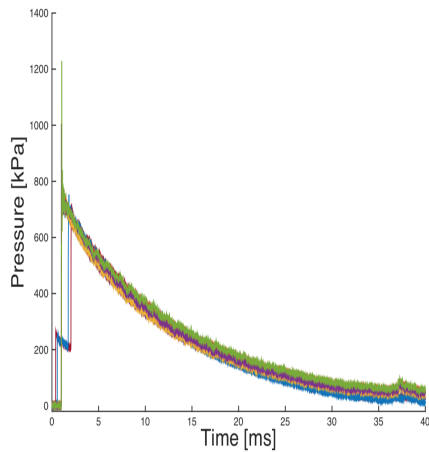
(d) Intended driver pressure of 2000 kPa



*(e) Intended driver pressure of 2500 kPa*



*(f) Intended driver pressure of 3500 subfigure*



*(g) Intended driver pressure of 4000 kPa*

**Figure C.1:** Pressure distribution on the plate.

### C.3 Component Experiments

**Table C.3:** Experiments performed on the steel plates.

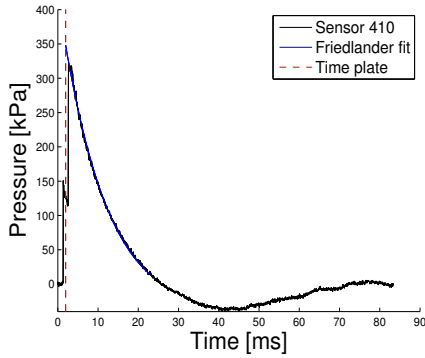
Test #	Composition of membranes [mm]
S0.8-15	(0.25+0.25)x3
S0.8-25	(0.50+0.50)x3
S0.8-35	((0.25+0.50)x2)x3

**Table C.4:** Experiments performed on the aluminium plates.

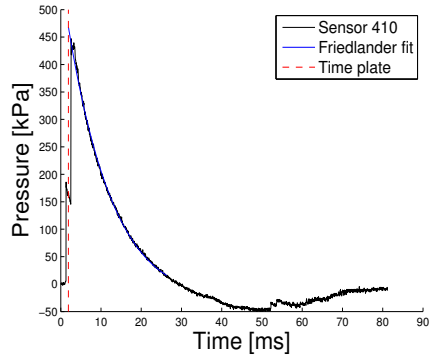
Test #	Composition of membranes [mm]
A0.8-5	0.25+0.25
A0.8-7.5	(0.25x2)+(0.25x2)
A0.8-10	(0.25+0.25)x3
A2.0-15	(0.25+0.25)x3
A2.0-25	(0.50+0.50)x3
A2.0-35	((0.25+0.50)x2)x3

### C.3.1 Pressure distribution on the plates

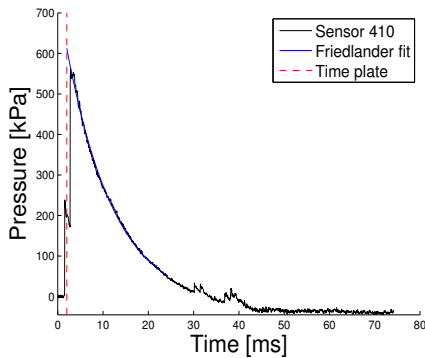
The pressure is extrapolated back in time using the Friedlander equation. The dashed, red line shows where the blast wave encounters the plate. Note that for 0.8mm aluminium there is only two graphs. Since the plate in the experiment A0.8 – 10 fractured, the Friedlander curve was not plotted.



(a) S0.8-15.

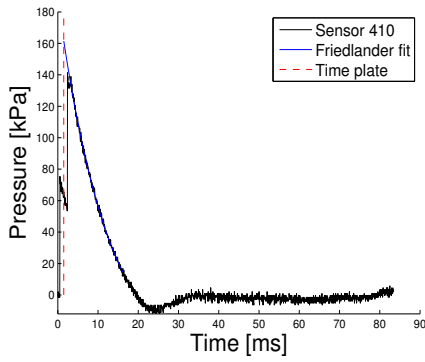


(b) S0.8-25.

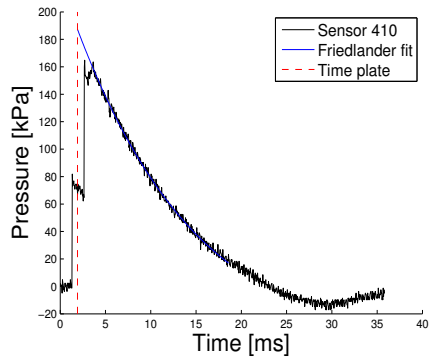


(c) S0.8-35.

Figure C.2: The 0.8mm steel plates.

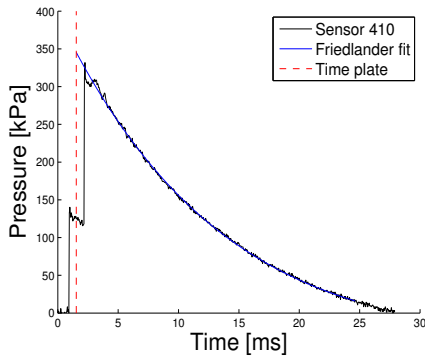


(a) A0.8-5.

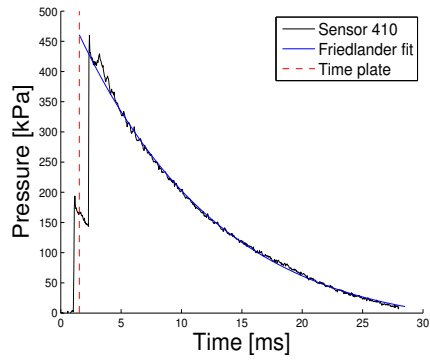


(b) A0.8-7.5.

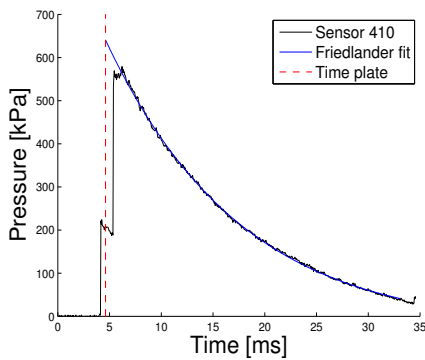
**Figure C.3:** The 0.8mm aluminium plates.



(a) A2.0-15.



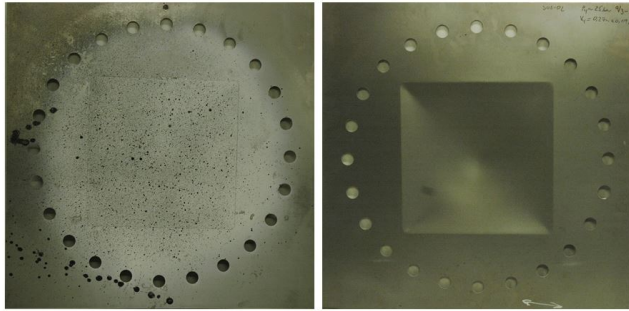
(b) A2.0-25.



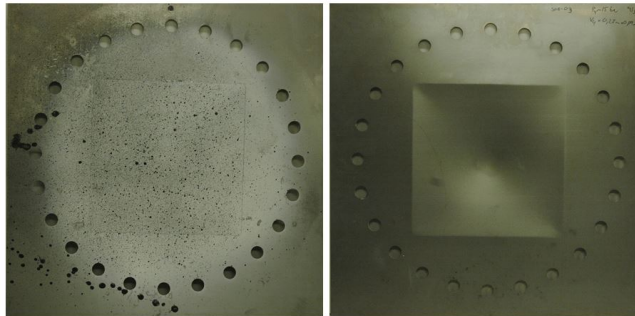
(c) A2.0-35.

**Figure C.4:** The 2.0mm aluminium plates.

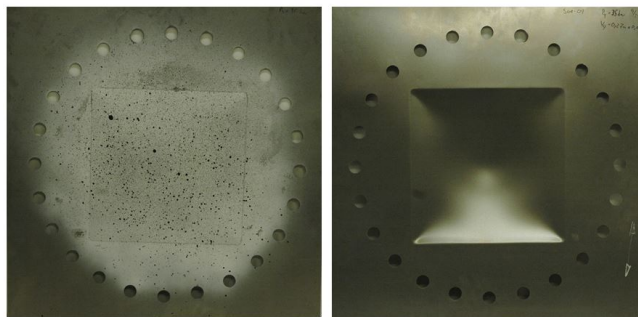
### C.3.2 Deformed plates



(a) S0.8-15.

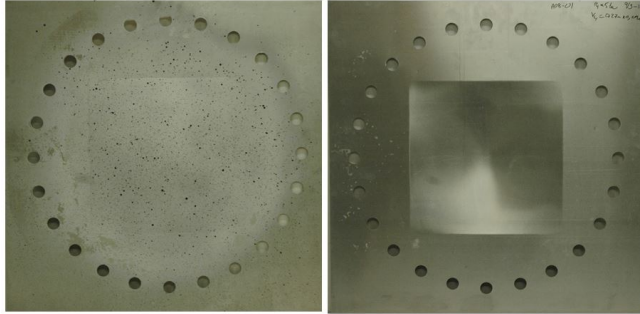


(b) S0.8-25.

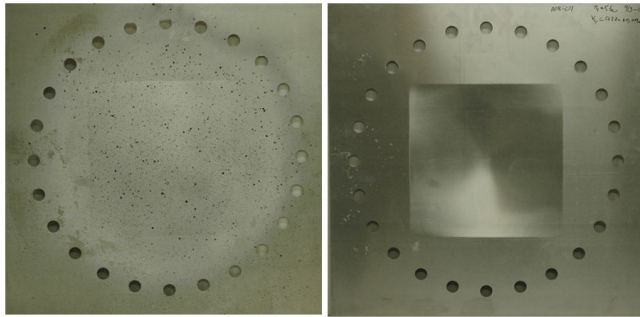


(c) S0.8-35.

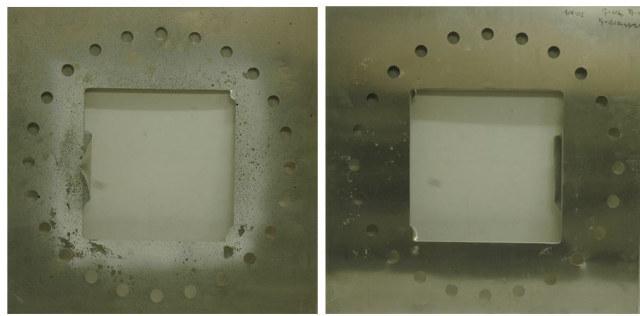
**Figure C.5:** Deformed 0.8mm steel plates.



**(a)** A0.8-5.

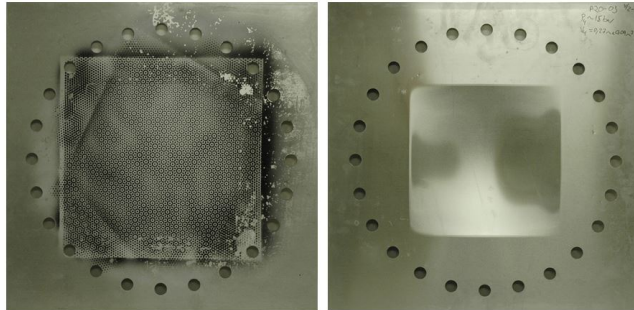


**(b)** A0.8-7.5.

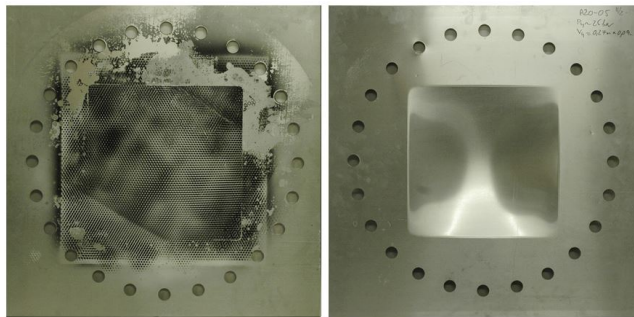


**(c)** A0.8-10

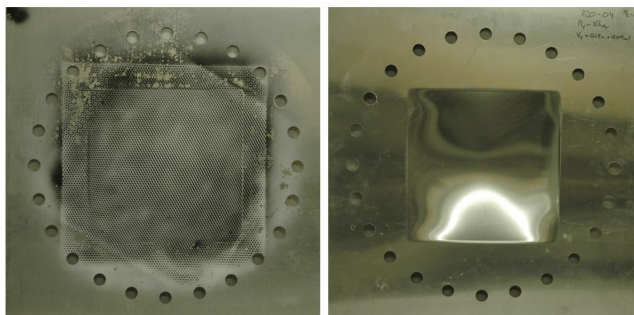
**Figure C.6:** Deformed 0.8mm aluminium plates.



(a) A2.0-15.



(b) A2.0-25.



(c) A2.0-35.

**Figure C.7:** Deformed 2.0mm aluminium plate



### C.3.3 Matlab script

Matlab script to obtain 3D-plots of the DIC results.

```
%Script for generating 3D-plots of DIC data

clear
close all
clc

%input picture number
foi = [2 43 49 52 57 61 67 70 73 78 82 106 109 114 119]; %A20-05-01
numb = 5;
id = foi(numb);

%minClim specifies the data value that maps to the first colour into the
%colourmap and maxClim specifies the data value that maps to the last colour
%in the colourmap.

minClim = 0;
maxClim = 25; %A20-05-01

eyecam = [0 600, 5]; %A20-05-01, numb = 1-13

cat = 'C:/Tess/A20-05-01/dic25/';
pre = 'c1_test';

name = '';
if(id < 10)
    name = ['000' num2str(id)];
elseif(id < 100)
    name = ['00' num2str(id)];
elseif(id < 1000)
    name = ['0' num2str(id)];
elseif(id < 10000)
    name = [num2str(id)];
end

if(~strcmp(cat(length(cat)-1),'/')) cat = [cat '/']; end
fpath = [cat pre name '.eco'];
```

```
dicmesh = ReadMeshBinary(fpath);
dicmesh = RigidBodyTransform(dicmesh, -0.28, -3.20, 0, 0, 0, -12.55); %%A20-05-01

corrX = 143; %%A20-05-01
corrY = 163; %%A20-05-01

dicmesh.nlocX(:,1) = dicmesh.nlocX(:,1) + corrX;
dicmesh.nlocX(:,2) = dicmesh.nlocX(:,2) + corrY;

if(~isempty(dicmesh.nlocX))
    [elmGrid, nodeGrid] = Mesh2ElementQ4Grid(dicmesh);
    ndX = dicmesh.nlocX + dicmesh.ndefX;
    X = zeros(size(nodeGrid)); Y = X; Z = X; dZ = X;
    for i = 1:length(nodeGrid(:,1))
        for j=1:length(nodeGrid(1,:))
            X(i,j) = ndX(nodeGrid(i,j), 1);
            Y(i,j) = ndX(nodeGrid(i,j), 2);
            Z(i,j) = ndX(nodeGrid(i,j), 3);
            dZ(i,j) = dicmesh.ndefX(nodeGrid(i,j), 3);
        end
    end
end

%%2D-plot: Distribution of the displacement over the cross-section

xtl = [150 150];
ytl = [-1000 1000];

hFig = figure(2);
set(hFig, 'units','normalized', 'Position', [0.4 0.1 0.6 0.7])
hand = plot(X(14,:), -Z(14,:), 'k');
set(hand, 'LineWidth', 1.5);

hold on
hand3 = plot(xtl,ytl, 'k--');
set(hand3, 'LineWidth', 1);

set(gca, 'XTick', 0:50:300, 'YTick', 0:4:32, 'FontSize', f3); %%A20-05-01
axis([0 300 0 32]) %%frame id: [21 25 35 40 49]; %%A20-05-01
```

```

xlabel('x [mm]','FontName','Arial','fontSize',f3,'color','k');
ylabel('Displacement [mm]','FontName','Arial','fontSize',f3,'color','k')

%3D-plot of the plate

hFig4 = figure(4);
set(hFig4, 'units','normalized', 'Position', [0.005 0.04 0.5 0.85])
surf(X,Y,-Z,-dZ);
camlight left;
lighting phong
colormap gray
material dull
shading interp

axis([0 300 0 300 -60 30])
set(gca,'CLim',[minClim maxClim])
cb = colorbar('Location','NorthOutside','FontSize',f3);
axpos=get(gca,'position');
cpos=get(cb,'Position');
cpos(4)=2*cpos(4); %Height colorbar
cpos(2)=0.98*cpos(2); %Vertical position colorbar
set(cb,'Position',cpos)
set(gca,'position',axpos)

h = camlight;
set(h,'Position',eyecam)

scale = 20;
iLen = length(X(:,1))*scale;
jLen = length(X(1,:))*scale;
Xi = zeros(iLen,jLen);
Yi = zeros(iLen,jLen);

for i= 1:iLen,
    for j= 1:jLen,
        Xi(i,j) = j / scale;
        Yi(i,j) = i / scale;
    end
end
end

```

```
ZZ = interp2(Z,Xi,Yi);
XX = interp2(X,Xi,Yi);
YY = interp2(Y,Xi,Yi);
dZZ = interp2(dZ,Xi,Yi);

mini = 1;
for i = 1:length(ZZ(:,1))
    if(length(find(isnan(ZZ(i,:)))) < length(ZZ(i,:)))
        mini = i;
        break;
    end
end
minj = 1;
for i = 1:length(ZZ(1,:))
    if(length(find(isnan(ZZ(:,i)))) < length(ZZ(:,1)))
        minj = i;
        break;
    end
end

XX = XX(mini:length(XX(:,1)), minj:length(XX(1,:)));
YY = YY(mini:length(YY(:,1)), minj:length(YY(1,:)));
ZZ = ZZ(mini:length(ZZ(:,1)), minj:length(ZZ(1,:)));
dZZ = dZZ(mini:length(dZZ(:,1)), minj:length(dZZ(1,:)));

%Generate colour picture that displays displacement
min_x = min(min(XX));
min_y = min(min(YY));
max_x = max(max(XX));
max_y = max(max(YY));

% The image data you want to show as a plane.
planeimg = -ZZ;

% Desired z position of the image plane.
imgzposition = -60;

minplaneimg = minClim; % Specified minimum.
maxplaneimg = maxClim; % Specified maximum.
```

```
scaledimg = (floor(((planeimg - minplaneimg) ./ ...
maxplaneimg - minplaneimg)) * 255)); % perform scaling

% Convert the image to a true colour image with the jet colourmap.
colorimg = ind2rgb(scaledimg,jet(256));

%Instead of showing planeimg, we show colorimg

hold on;

% plot the image plane using surf.
surf([min_x max_x],[min_y max_y],repmat(imgzposition, [2 2]),...
colorimg,'facecolor','texture');

view(-45,30);
%view(-45,20);
set(gca,'XTick',0:75:300,'YTick',0:75:300,'ZTick',-30:30:30,...
'FontSize',f3); %S15
set(gcf,'Color','white')
grid off

xlabel('x [mm]','FontSize',f3);
ylabel('y [mm]','FontSize',f3);
zlabel('Displacement [mm]','FontSize',f3);

colormap(jet(256));
cbfreeze(cb);
colormap(gray);
set(gca,'CLim',[minClim2 maxClim2])
```

# Appendix D

## Numerical Simulation (Ch. 7)

### D.1 Material cards implemented in ABAQUS/Explicit

#### D.1.1 Direct modeling

##### Steel Plates

```
*****  
** Steel 0.8 mm  
*****  
*Material, name=SMM_ST_08  
*Density  
7800,  
*INCLUDE, INPUT=./DEPVAR_SMM.inc  
*USER MATERIAL, CONSTANTS=32  
** EFLAG, YFLAG, RMAPFLAG, HFLAG, VFLAG, TFLAG, DFLAG, SFFLAG  
1, 1, 2, 1, 1, 0, 1, 0  
** STFLAG, E, NU, SIGMA0, KSI, THETAR1, QR1, THETAR2  
0, 210e9, 0.3, 334.5e6, 0.1, 9944.1e6, 117.1e6, 4313.3e6  
** QR2, THETAR3, QR3, dRdpmin, CS, PDOTS, DINIT, DCRIT  
379.7e6, 0, 0, 0, 0.001, 0.0005, 0.0, 1e12  
** WC, PHI, GAMMA  
1.0e6, 1.0, 1.0
```

```

*****
** Steel 2.0 mm
*****
*Material, name=SMM_ST_2
*Density
7800,
*INCLUDE,INPUT=./DEPVAR_SMM.inc
*USER MATERIAL,CONSTANTS=32
**  EFLAG,   YFLAG, RMAPFLAG,  HFLAG,   VFLAG,   TFLAG,   DFLAG,   SFFLAG
      1,     1,     2,     1,     1,     0,     1,     0
**  STFLAG,   E,     NU, SIGMA0,   KSI, THETAR1,   QR1, THETAR2
      0,  210e9,   0.3,355.6e6,   0.1,4067.5e6,   345e6,  11588e6
**  QR2, THETAR3,   QR3,dRdpmin,   CS,   PDOTS,   DINIT,   DCRIT
      135e6,   0,     0,     0,   0.001,  0.0005,   0.0,   1e12
**  WC,     PHI,   GAMMA
      1.0e6,   1.0,   1.0

```

**Aluminium Plates**

```

*****
** Aluminium 0.8 mm
*****
*Material, name=SMM_AL_08
*Density
2710,
*INCLUDE,INPUT=./DEPVAR_SMM.inc
*USER MATERIAL,CONSTANTS=32
**  EFLAG,   YFLAG, RMAPFLAG, HFLAG,   VFLAG,   TFLAG,   DFLAG,   SFFLAG
      1,     1,     2,     1,     1,     0,     1,     0
**  STFLAG,   E,     NU, SIGMA0,   KSI, THETAR1,   QR1, THETAR2
      0, 71000e6,   0.3,97.58e6,   0.1, 19201e6, 13.17e6, 1976.1e6
**  QR2, THETAR3,   QR3,dRdpmin,   CS,   PDOT,   DINIT,   DCRIT
      10.63e6,   0,     0,     0,   0.014, 0.0005,   0.0,   1e12
**  WC,     PHI,   GAMMA,
      1.0e6,   1.0,   1.0
*****
** Aluminium 2.0 mm
*****
*Material, name=SMM_AL_2
*Density
2710,
*INCLUDE,INPUT=./DEPVAR_SMM.inc
*USER MATERIAL,CONSTANTS=32
**  EFLAG,   YFLAG, RMAPFLAG, HFLAG,   VFLAG,   TFLAG,   DFLAG,   SFFLAG
      1,     1,     2,     1,     1,     0,     1,     0
**  STFLAG,   E,     NU, SIGMA0,   KSI, THETAR1,   QR1, THETAR2
      0, 71000e6,   0.3,86.82e6,   0.1, 879.0e6, 8.51e6,16414.2e6
**  QR2, THETAR3,   QR3,dRdpmin,   CS,   PS,   DINIT,   DCRIT
      16.52e6,   0,     0,     0,   0.014, 5e-4,   0.0,   1e12
**  WC,     PHI,   GAMMA
      1.0e6,   1.0,   1.0

```



## D.1.2 Inverse modeling

### Steel Plates

```

*****
** Steel 0.8 mm
*****
*Material, name=SMM_ST_08
*Density
7800,
*INCLUDE,INPUT=../DEPVAR_SMM.inc
*USER MATERIAL,CONSTANTS=40
** EFLAG, YFLAG, RMAPFLAG, HFLAG, VFLAG, TFLAG, DFLAG, SFFLAG
    1, 1, 2, 1, 1, 12, 1, 0
** STFLAG, E, NU, SIGMA0, KSI, THETAR1, QR1, THETAR2
    0, 210e9, 0.3, 330e6, 0.1,2.886e10, 27.45e6, 7083e6
** QR2, THETAR3, QR3,dRdpmin, CS, PDOTS, TI, TO
    164.6e6, 2330e6, 392e6, 0, 0.005, 0.0001, 293, 293
** TM, RHO, CT, BETATQ, MS, DINIT, DCRIT, WC
    1800, 7800, 452, 0, 1.0, 0.0, 1.0, 815e6
** PHI, GAMMA
    1.0, 1.0
*****
** Steel 2.0 mm
*****
*Material, name=SMM_ST_2
*Density
7800,
*INCLUDE,INPUT=../DEPVAR_SMM.inc
*USER MATERIAL,CONSTANTS=40
** EFLAG, YFLAG, RMAPFLAG, HFLAG, VFLAG, TFLAG, DFLAG, SFFLAG
    1, 1, 2, 1, 1, 12, 1, 0
** STFLAG, E, NU, SIGMA0, KSI, THETAR1, QR1, THETAR2
    0, 210e9, 0.3, 330e6, 0.1,6.141e10, 43.89e6, 8616e6
** QR2, THETAR3, QR3,dRdpmin, CS, PDOTS, TI, TO
    179.4e6, 2250e6, 352e6, 0, 0.005, 0.0001, 293, 293
** TM, RHO, CT, BETATQ, MS, DINIT, DCRIT, WC
    1800, 7800, 425, 0, 1.0, 0.0, 1.0, 880e6
** PHI, GAMMA
    1.0, 1.0

```

**Aluminium Plates**

```

*****
** Aluminium 0.8 mm
*****
*Material, name=SMM_AL_08
*Density
2710,
*INCLUDE, INPUT=./DEPVAR_SMM.inc
*USER MATERIAL, CONSTANTS=40
** EFLAG, YFLAG, RMAPFLAG, HFLAG, VFLAG, TFLAG, DFLAG, SFFLAG
    1, 1, 2, 1, 1, 12, 1, 0
** STFLAG, E, NU, SIGMA0, KSI, THETAR1, QR1, THETAR2
    0, 71000e6, 0.3, 100e6, 0.1, 1.535e4, 8.59e6, 3051e6
** QR2, THETAR3, QR3, dRdpmin, CS, PDOTS, TI, TO
    10.71e6, 80e6, 4e6, 0, 0.010, 5e-4, 293, 293
** TM, RHO, CT, BETATQ, MS, DINIT, DCRIT, WC
    918, 2710, 899, 0, 1.0, 0.0, 1.0, 120e6
** PHI, GAMMA
    1.0, 1.0
*****
** Aluminium 2.0 mm
*****
*Material, name=SMM_AL_2
*Density
2710,
*INCLUDE, INPUT=./DEPVAR_SMM.inc
*USER MATERIAL, CONSTANTS=40
** EFLAG, YFLAG, RMAPFLAG, HFLAG, VFLAG, TFLAG, DFLAG, SFFLAG
    1, 1, 2, 1, 1, 12, 1, 0
** STFLAG, E, NU, SIGMA0, KSI, THETAR1, QR1, THETAR2
    0, 71000e6, 0.3, 95e6, 0.1, 7452e6, 5.507e6, 2078e6
** QR2, THETAR3, QR3, dRdpmin, CS, PDOTS, TI, TO
    8.243e6, 80e6, 17.5e6, 0, 0.010, 5e-4, 293, 293
** TM, RHO, CT, BETATQ, MS, DINIT, DCRIT, WC
    918, 2710, 899, 0, 1.0, 0.0, 1.0, 200e6
** PHI, GAMMA
    1.0, 1.0

```